Durham E-Theses

Coupling of beam and shell finite elements for the rapid analysis of tubular structures

LUSH, ANNABEL,MARIE

How to cite:

LUSH, ANNABEL,MARIE (2014) *Coupling of beam and shell finite elements for the rapid analysis of tubular structures*, Durham theses, Durham University. Available at Durham E-Theses Online: http://etheses.dur.ac.uk/10843/

Use policy

The full-text may be used and/or reproduced, and given to third parties in any format or medium, without prior permission or charge, for personal research or study, educational, or not-for-profit purposes provided that:

- a full bibliographic reference is made to the original source
- a link is made to the metadata record in Durham E-Theses
- the full-text is not changed in any way

The full-text must not be sold in any format or medium without the formal permission of the copyright holders.

Please consult the full Durham E-Theses policy for further details.

Academic Support Office, Durham University, University Office, Old Elvet, Durham DH1 3HP
e-mail: e-theses.admin@dur.ac.uk Tel: +44 0191 334 6107
http://etheses.dur.ac.uk

Coupling of beam and shell finite elements for the rapid analysis of tubular structures

Annabel Marie Lush

Thesis submitted as consideration towards the degree of Master of Science.

Mechanics Group
School of Engineering and Computing Sciences
Durham University
United Kingdom

May 2014

Coupling of beam and shell finite elements for the rapid analysis of tubular structures

Annabel Marie Lush

Abstract

The research presented in this thesis focuses on the development of a technique to couple beam and shell elements, with the purpose of creating one finite element (FE) model to capture the global and local structural behaviour of an offshore wind turbine foundation design: the Inward Battered Guide Structure (IBGS). The technique is proven to be computationally efficient in that less storage capacity is required as there are fewer degrees of freedom (DOF) than compared with an equivalent analysis that uses only hexahedral elements, for example. Furthermore, the method is effective in providing reliable results in a shorter amount of time as it mitigates the necessity of the Design Engineer to perform separate local and global analyses. Although the beam-shell coupling is applied to the numerical analysis of the IBGS here, the technique is applicable to any tubular structure.

Initially, the simple theories of bending and torsion are reviewed and the formulation of the three-dimensional (3D) Euler-Bernoulli (EB) beam element is given. In addition, the concepts of plate and shell theory are discussed with an emphasis on finding a reliable general shell element. The formulation of the isoparametric degenerate continuum (IDC) shell and the mixed interpolation of tensorial components shell element with nine nodes (MITC9) for linear static analysis are given. It was found that the IDC shell was inadequate to solve simple benchmark problems due to shear locking. It is shown that the MITC9 formulation does not suffer from this problem. The thesis then proceeds to discuss various methods to impose multi-point constraint (MPC) equations, including the transformation equations, penalty functions and Lagrange multipliers, for the purpose of coupling different types of finite elements. The MPC equations to couple EB beam and MITC9 shell elements are developed through a purely geometric approach. The capability to couple these elements is successfully demonstrated in

the numerical analysis of the IBGS.

Through the application of the beam-shell coupling, it is concluded that the twisted jacket arrangement of the IBGS shows reduced stiffness and higher stresses under static loading. It is found that an untwisted jacket arrangement of the IBGS is two-to-three times stiffer than the twisted jacket arrangement for the case of linear static analysis. The analyses are undertaken with firstly a FE model containing only EB beam elements and secondly a FE model that employs the beam-shell coupling technique. The beam-shell coupling enables both the stress distribution through the structural joints, modelled with shell elements, and the axial/bending behaviour of the main structural members, modelled with beam elements, to be assessed in a single analysis.

Declaration

The work in this thesis is based on research carried out in the Mechanics Group in the School of Engineering and Computing Sciences at Durham University. No part of this report has been submitted elsewhere for any other degree or qualification and all of the work is my own, unless referenced to the contrary in the text.

Copyright © 2014 by Annabel Marie Lush.

"The copyright of this thesis rests with the author. No quotations from this document should be published without the authors prior written consent and any information derived from this document should be acknowledged."

Acknowledgements

This research would not have been possible without the generous financial support through the DONG Energy Durham University Partnership, for which I am truly grateful.

I would like to thank Professor Roger Crouch (formerly Head of School) for his encouragement to undertake this interesting project, following my BEng Final Year Project focused on hexahedral mesh refinement. Over the past couple of years, Professor Crouch has continuously encouraged me to question the reasoned logic behind fundamental concepts, an invaluable skill that aids understanding and problem solving.

Throughout my MSc by Research, my supervisors Dr William Coombs, Professor Jon Trevelyan (Head of School) and Professor Roger Crouch (City University) have generously given their time to regularly discuss my work, provide advice in debugging code and also share their knowledge and expertise. It has been a privilege to work with them and I am very grateful for all of their support and advice. In particular, Dr Coombs has been instrumental in helping me to understand the formulation shell elements, an area that has been crucial to the success of this project.

In addition, I would like to thank Dr Richard Williams for the opportunity to share my preliminary findings at the Supergen Wind Phase 2 - 7th Training Seminar at Loughborough University on the 4^{th} September 2013.

Finally, I would like to thank my family, St Mary's College and the School of Engineering and Computing Sciences for their continued support throughout the four fun-filled years I have spent in this beautiful Cathedral city.

Annabel Lush
Durham, May 2014

Contents

List of Figures

List of Tables

List of Algorithms

Nomenclature & Abbreviations

For ease of reference, the nomenclature, which follows the list of abbreviations, is divided into categories by mathematical object type. The *identifiers* and *operators* can be applied to any of the *scalars*, *vectors* or *matrices* respectively.

Abbreviations

3D	three-dimensional
BC	boundary condition
CAD	computer aided design
CAPEX	capital expenditure
DOF	degree of freedom
EB	Euler-Bernoulli
FE	finite element
FEM	finite element method
FEA	finite element analysis
GP	Gauss-point
IBGS	Inward Battered Guide Structure
IDC	isoparametric degenerate continuum
MITC	mixed interpolation of tensorial components
MITC9	mixed interpolation of tensorial components shell element with nine nodes
MPC	multi-point constraint
NA	neutral axis

Identifiers

^{L}	Linear.
^{NL}	Non-linear.
^{b}, $_{b}$	Quantity associated with a beam element.
^{c}	Constrained system (in Section 4.2.3 Langrange Multipliers).
^{c}	Condensed out quantity associated with the transformation equations method.
^{t}	Quantity associated with translations (in Section 3.3 IDC Shell Element Formulation).
^{e}	Quantity associated with a single finite element.
^{ext}	External.
^{i}	Iteration number.
^{int}	Internal.
^{k}	Node number.
^{r}	Quantity associated with rotations (in Section 3.3 IDC Shell Element Formulation).
^{r}	Retained quantity associated with the transformation equations method.
^{r}	Reduced system associated with the transformation equations method.
^{s}, $_{s}$	Quantity associated with a shell element.
^{t}	Load step.
^{GP}	Quantity associated with a Gauss point.

$\bar{}$	Virtual quantity of $()$.
$'$	Local quantity.

Operators

$\Delta( )$	Small change in $( )$.
$\delta( )$	Increment of $( )$.
d( )	Differential of $( )$.
det( )	Determinant of $( )$.
tr( )	Trace of $( )$.
$( )^T$	Transpose of $( )$.
$\|( )\|_2$	Normalised vector / L2 norm of $( )$.

Scalars

α	Geometric angle.
β_1, β_2	Global MITC9 shell rotations.
γ	Shear strain component (in Section 2.4 Torsion).
θ_{xx},θ_{yy},θ_{zz}	Global rotations.
κ	Shear coefficient.
λ	Lagrange multiplier.
ν	Poisson's ratio.
ρ	Density.
σ_v	Von Mises stress.
τ	Shear stress component (in Section 2.4 Torsion).
ϕ, ψ	Global angles to define the shell mid-surface normal.
$\delta\phi$, $\delta\psi$	Global IDC shell rotations.
ξ, η, ζ	Local coordinates.
A	Area.
D	Diameter.
E	Young's modulus.
G	Shear modulus.
I	Second moment of area.
I_p	Polar second moment of area.
J	Torsion constant.
L	Length.
M	Moment.
P	Point load.
Q	Shear force.
T	Torque, which is also denoted as M_{xx} in the local beam element coordinate system.
R	Radius.
S, S^0	Surface in the current and reference configurations.
V, V^0	Volume in the current and reference configurations.
b	Breadth.
d	Depth.
f	Force.
g	Gravitational acceleration.
s	Arc length.
t	Thickness.
t_w	Wall-thickness ratio.
u, v, w	Global translations.
w_{GP}	Gauss point weight.
x, y, z	Global Cartesian coordinates.

IBGS Specific Scalars

ϕ_{IB}	Angle of inclined bracing.
ϕ_{JT}	Angle of jacket twist.
H_j	Jacket height.
H_{lc}	Height of lower-central column.
H_p	Pile height (from the seabed to the bottom of the jacket legs).
H_t	Tower height.
L_b	Length of bottom-radial member.
L_t	Length of top-radial member.

Vectors

$\{\}$	Column vector.
$\{\}^T$	Row vector.
$\{\gamma\}$	Green-Lagrange strain vector (in Chapters 3-6).
$\{\epsilon\}$	Engineering strain.
$\{\sigma\}$	Cauchy stress vector.
$\{\tau\}$	Second Piola-Kirchoff stress vector (in Chapters 3-6).
$\{d\}$	Displacements.
$\{e\}$	Coordinate base vector.
$\{f_b\}$	Body force.
$\{f_{ext}\}$	External force.
$\{f_{int}\}$	Internal force.
$\{f_{oobf}\}$	Out-of-balance force.
$\{f_p\}$	Point load.
$\{f_t\}$	Surface traction.
$\{Q\}$	Prescribed displacements in MPC equations.
$\{Q_0\}$	Congruent transformation vector.
$\{V_1\}$, $\{V_2\}$	Global unit vectors defined at each node on the MITC9 shell.
$\{V_d\}$	Direction vector defined between nodes to be coupled.
$\{V_n\}$	Shell mid-surface normal.

Matrices

$[\alpha]$	Penalty numbers matrix (in Section 4.2.2 Penalty Functions).
$[\gamma]$	Green-Lagrange strain matrix.
$[\sigma]$	Cauchy stress matrix.
$[\sigma_{dev}]$	Deviatoric stress matrix.
$[B]$	Strain-displacement matrix.
$[C]$	Matrix of constraint equations.
$[\tilde{C}]$	EB beam-MITC9 shell coupling matrix.
$[C_{CI}]$	Matrix containing the node numbers at the coupling interface.
$[D]$	Elastic material stiffness matrix.
$[F]$	Deformation gradient matrix.
$[J]$	Jacobian matrix.
$[K]$	Structural stiffness matrix.
$[N]$	Nodal shape functions.
$[S]$	Second Piola-Kirchoff stress matrix.
$[T]$	Congruent transformation matrix.
$[T_b]$	Beam rotation matrix.
$[T_s]$	MITC9 shell rotation matrix.
$[V]$	Derivatives of $\{V_n\}$ (in Section 3.3 IDC Shell Element Formulation).

Chapter 1

Introduction

High efficiency is paramount in computational structural analysis, a vital tool that aids the work of the Design Engineer. Often, in commercial finite element (FE) software, it is most economical to undertake separate local (part of a structure) and global (whole structure) analyses. However, the aim here is to demonstrate how the coupling of FE of different dimensions, in terms of different numbers of degree of freedom (DOF) per node, can be employed to run one, efficient analysis of a structure and yet maintain the level of detail required where necessary. More specifically, the unique contribution here is the coupling between the three-dimensional (3D) Euler-Bernoulli (EB) element and the mixed interpolation of tensorial components shell element with nine nodes (MITC9). Although the technique could be applied to any tubular structure with slender members, the work presented in this thesis focuses on investigating the structural behaviour of a particular foundation design for offshore wind turbines: the Inward Battered Guide Structure (IBGS).

At present, a priority for the rapidly expanding offshore wind industry is to reduce CAPEX costs from £140/MWh to £100/MWh* by 2020 [*64*], alongside developing larger turbines that are located further offshore. The challenge is to reduce costs across the supply-chain by standardising components, a central message from the Renewable UK Offshore Wind 2013 Conference in Manchester. Cost reduction is essential if the operational capacity of offshore wind capacity is to increase from 3.3GW to 18GW in contribution to the UK Government's target of 15% energy from renewable sources by 2020 [*29*, *57*]. Around 30% of CAPEX costs for offshore wind are attributed to the design, fabrication and installation of foundations [*15*] - a term used loosely here to describe the structure supporting a wind turbine. In this regard, the Carbon Trust organised a foundation design competition through its Offshore Wind Accelerator project with a view to developing an economical foundation suitable for water depths 20-60m at Round III sites around the UK [*16*]. Keystone Engineering's IBGS or 'twisted-jacket' was one of four finalists from this competition, as shown by (ii) in Figure 1.1. According to Keystone

*Levelised cost of energy, i.e. the lifetime cost of the project with respect to the amount of energy generated. [*64*]

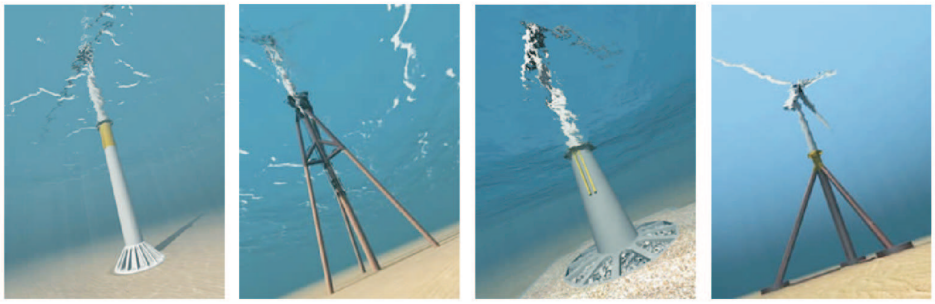

(i) (ii) (iii) (iv)

Figure 1.1: Finalists from the Carbon Trust's foundation design competition: (i) suction bucket monopile (ii) twisted jacket (iii) gravity structure and (iv) suction bucket tripod [*63*].

Engineering [*48*], the IBGS is around 20% cheaper than traditional jacket foundations and its simple design provides greater efficiency in transportation. In addition, Keystone Engineering have used this foundation to support oil and gas platforms in the Gulf of Mexico.

The steel IBGS would be installed by first driving the central pile into the sea bed (Figure 1.2 (i)) and then the jacket would be lowered and secured, probably with grouting, on the central pile (Figure 1.2 (ii)). Each jacket leg acts as a sleeve to guide the three remaining piles as they are driven into the sea bed (Figure 1.2 (iii)). Although the jacket itself is a standard

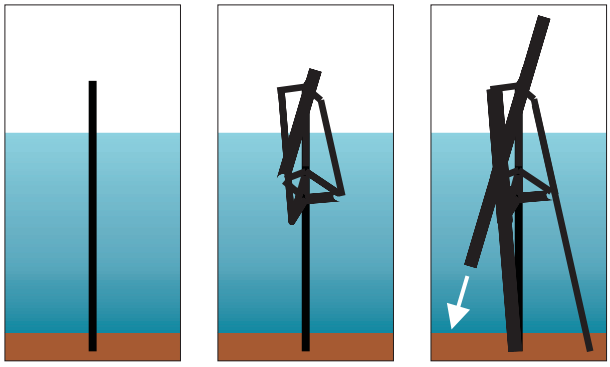

(i) (ii) (iii)

Figure 1.2: Installation sequence of the IBGS.

size, the foundation is readily adapted for different site conditions (water depth, soil properties etc.) by varying the pile length. With this in mind, the IBGS has the potential to reduce costs by becoming a standard part in the supply chain and so the development of an efficient analysis capability to quickly assess the structural behaviour under different parameters at various locations could be a useful, time-saving tool for the Design Engineer.

To date, the IBGS has been successfully installed as a demonstration project at Hornsea, over 190km off the Yorkshire coastline by the SMart Wind consortium, with financial support from DONG Energy, to support a meteorological mast [*17*], as seen in Figure 1.3. Its use as

Figure 1.3: Demonstration of the IBGS at Hornsea [*58*].

a viable foundation solution for offshore wind will be dependent upon the economics of the ease of fabrication, transportation and installation, in addition to the structural behaviour. Nevertheless, the beam-shell coupling devised in this thesis is used to provide some indication as to the structural advantages of the unusual design of the IBGS. This will be achieved by modelling structural members with beam elements and structural joints with shell elements. In this way, it is anticipated that both elements should capture the general bending behaviour well and that, in addition, the shell elements should capture the localised stress variation at each joint. In the following, a brief introduction to the finite element method (FEM) that underpins the research is given, followed by the scope and structure of this thesis.

1.1 Background - The Finite Element Method

The finite element method (FEM) is a numerical analysis technique that has been widely used for over fifty years to accurately model physical phenomena, expressed by partial differential equations, where analytical techniques are not possible. The name *finite element* originates from work by Clough [*20*] to analyse shell-type structures at the beginning of the computer era, following work by Turner et al. [*66*], in which triangular elements were used to model the delta-wing for the aeronautics industry [*21*]. Previously, the method had been derived by Courant [*24*] as a purely mathematical approach to solve problems by creating subregions of triangles [*45*]. Today, the FEM is an integral part of engineering across various disciplines to investigate problems including structural behaviour, geomechanics, fluid flow, heat transfer and electromagnetics. In essence, the FEM involves subdividing a body into individual elements that are interconnected at nodes and collectively form a mesh. On solving the assemblage of

equations associated with each element to find the nodal variables, an approximation of the physical phenomena in question is obtained.

In computational structural mechanics, the FEM is used to find nodal displacements, $\{d\}$, as a result of the external loads, $\{f_{est}\}$, that are imposed, given the material stiffness[†], $[K]$. One approach to obtain an expression for the stiffness matrix is to consider the *Principle of Virtual Work* whereby a real force is applied to a system in static equilibrium and an imaginary or *virtual displacement*, $\{\delta\bar{d}\}$, is induced. More specifically, this concept is termed the *Principle of Virtual Displacements*[‡]. In other words, for any virtual displacement relative to the equilibrium condition, the *external virtual work* is equal to the *internal virtual work*. External virtual work includes external surface tractions, $\{f_t\}$, external point forces, $\{f_p\}$, and external body forces, $\{f_b\}$, such as gravity, whereas internal virtual work can be described as a change in the internal strain energy. Mathematically, this is expressed as

$$\underbrace{\int_V \{\delta\bar{\epsilon}\}^T\{\sigma\}dV}_{\text{Internal strain energy}} = \underbrace{\int_V \{\delta\bar{d}\}^T\{f_b\}dV}_{\text{External body forces}} + \underbrace{\int_S \{\delta\bar{d}\}^T\{f_t\}dS}_{\text{External surface tractions}} + \underbrace{\int_V \{\delta\bar{d}\}^T\{f_p\}dV}_{\text{External nodal forces}} . \tag{1.1}$$

Equation (1.1) is an expression of the work equilibrium in which the virtual displacements, $\{\delta\bar{d}\}$, cause virtual strains, $\{\delta\bar{\epsilon}\}$. If it is assumed that all external forces are applied at nodes, then the integral could be replaced with a summation symbol. In addition, in the case of a non-linear analysis, the total change in internal strain energy would be with reference to the initial stress and strain state of a structure [*23*], as discussed in Chapter 3.

The virtual strain, $\{\bar{\epsilon}\}$, can be written in terms of the virtual displacements, $\{\delta\bar{d}\}$, as

$$\{\bar{\epsilon}\} = [B]\{\delta\bar{d}\} , \tag{1.2}$$

where $[B]$ is the *strain-displacement matrix* comprised of the derivatives of the local geometric interpolation functions with respect to the global coordinates. The engineering stress, $\{\sigma\}$, can be rewritten using a constitutive material law and the real (engineering) strain, $\{\epsilon\} = [B]\{d\}$, such that

$$\begin{aligned} \{\sigma\} &= [D]\{\epsilon\} \\ \{\sigma\} &= [D][B]\{d\} , \end{aligned} \tag{1.3}$$

where $[D]$ contains the material properties. On substituting (1.2) and (1.3) into (1.1) and removing the displacements from the integrals, as these are nodal values and do not vary

[†]Note that in some texts $[K]$ is called the *flexibility matrix* and on solving the system $\{d\} = [K]^{-1}\{f_{ext}\}$, the term $[K]^{-1}$ is named the *stiffness matrix*, though this distinction is not necessary here.

[‡]Alternatively, it can be assumed that real displacements are applied to the system to give *virtual forces*, a concept termed the *Principle of Virtual Forces*.

through the element, it is found that

$$\{\bar{\delta d}\}^T \int_V [B]^T[D][B]dV\{d\} = \{\bar{\delta d}\}^T \int_S \{f_t\}dS \; + \; \{\bar{\delta d}\}^T \int_V \{f_p\}dV \; + \; \{\bar{\delta d}\}^T \int_V \{f_b\}dV \; . \tag{1.4}$$

Notice that the virtual displacement terms, $\{\delta\bar{d}\}^T$, cancel to yield an expression of force equilibrium, such that

$$\underbrace{\int_V [B]^T[D][B]dV}_{\text{Stiffness, } [K]}\{d\} = \underbrace{\int_S \{f_t\}dS \; + \; \int_V \{f_p\}dV \; + \; \int_V \{f_b\}dV}_{\text{External forces, } \{f_{ext}\}} \; , \tag{1.5}$$

or more simply,

$$[K]\{d\} = \{f_{ext}\} \; , \tag{1.6}$$

where $\{d\}$ are the unknown displacements in a structure for which the system is solved, such that

$$\{d\} = [K]^{-1}\{f_{ext}\} \; . \tag{1.7}$$

Equation (1.5) shows the *weak form* of force equilibrium in that it applies in an average or integral sense through the volume and is evaluated only at certain points inside the element. Typically, a Gauss-Legendre quadrature is used to evaluate (1.5) at sampling or *Gauss points*, where each point is associated with a weight.

Instead of using the Principle of Virtual Work, equation (1.5) could have been obtained by deriving the *strong form* (which is continuous at all material points) by direct physical argument from the concepts of three-dimensional stress and strain. By multiplying the resulting expressions by a virtual displacement, integrating over the volume and rearranging through integration by parts, the weak form written as (1.5) can be found [*23*]. It is noted that there are other approaches in deriving the weak form of equilibrium, including the Rayleigh-Ritz method, a variational method that relies on using a functional such as that of the Principle of Minimum Potential Energy, or a weighted residual method such as the Galerkin method, which offers a more general mathematical approach to solving differential equations by trial solution [*23*].

A typical linear finite element analysis (FEA) is conducted in the following sequence.

1. **Define the geometry**, usually with the aid of computer aided design (CAD) software.
2. **Discretise the continuum**, namely the body to be analysed, using the chosen type of FE. The mesh could be developed through the volume or over the surface only. In 3D analysis using commercial software, hexahedral or tetrahedral elements are most commonly used since these are well understood and considered robust. When choosing the appropriate type of FE for the analysis, it is important to consider the following points.

- The element shape and geometric dimension, e.g. a 3D hexahedron.
- The number of DOF at each node, e.g. 3 displacements, u, v, w,
- The order of the element given by the number and arrangement of nodes, which gives the order of the local geometric interpolation functions or *shape functions* through an element. There are as many shape functions as there are nodes. For example, an eight-noded (serendipity) hexahedron with one node at each corner of the cube would be trilinear, whereas a twenty-noded (serendipity) hexahedron with three nodes along each edge would be triquadratic. Lagrangian elements have an extra node at the centre of each face and at the centre of each volume and so would have additional shape functions, but of the same order as the equivalent serendipity element.

There has been a wide range of methods developed for the discretisation process as summarised by Owen [*53*]. To give an example, the method of *paving* or *advancing fronts* starts from the surface of a volume and progressively subdivides the continuum towards the middle, where some additional processing is required to tie elements formed from different directions together. On forming the mesh, it may be necessary to perform a quality check, for instance, by considering the element aspect ratio or by checking that the volume scalar, $\det[J]$, between the local and global coordinate systems is positive. In addition, the mesh could be refined to produce a denser mesh by either h-, p- or r-refinement methods. H-refinement involves element subdivision whilst maintaining mesh conformity, namely node-node connections only, whereas p-refinement is concerned with increasing the order of each element by increasing the number of nodes and/or DOF. R-refinement is concerned with relocating nodes whilst maintaining the same number and order of elements [*23*]. These adaptive methods would allow greater detail around a complex piece of geometry for example. Equally, it would be possible to create a coarser mesh and reduce the system size to be solved.

3. **Select the displacement field** through each FE, in terms of the order and type of interpolation. If the interpolation functions for the geometry and the displacements are of the same order then the FE is termed an *isoparametric* element. In addition, the magnitude of the displacements to be calculated is taken into consideration. For linear elastic analysis, infinitesimal strains (small displacements and small rotations) are assumed, whereby the initial and final configurations are identical and so the Engineering stress and strain quantities can be used.
4. **Formulate the element stiffness matrices** using (1.5), which incorporates the material properties and strain-displacement matrix, and is evaluated at the Gauss points. The number and location of the Gauss points in a Gauss-Legendre integration scheme is given such that polynomials of order $(2n-1)$ are integrated exactly, where n is the

number of Gauss points in any one direction.

5. **Assemble the global stiffness matrix**. Generally element stiffness matrices are defined in a local coordinate system and so these must first be rotated into the global coordinate system.
6. **Solve** the system to find the displacements at all nodes.
7. **Postprocessing** activities, which might include calculating the quantities of stress and strain as well as perhaps refining the mesh around a region of high stress and repeating the FEA from step 4.

The sequence described above assumes a static linear analysis. In a non-linear static analysis, loads are applied in more than one load step and the system is solved iteratively at each load step until convergence of the solution is reached within a prescribed tolerance. For instance, the Newton-Raphson method can be used whereby the equilibrium to be achieved between the internal and external forces at each load step, t, is defined as

$$\{f_{oobf^t}\} = \{f^t_{ext}\} - \{f^t_{int}\} \leq \frac{\|\{f_{oobf}\}\|_2}{\|\|\{f_{ext}\}\|_2} \,. \tag{1.8}$$

$\{f_{oobf}\}$ is the *residual out-of-balance force* vector that should be within the ratio of the normalised (L2 norm) of the external and out-of-balance force vectors at equilibrium. At each load step, the system is solved iteratively, such that

$$[K]\{\delta_{i+1}\} = \{f_{oobf,\,i}\} \,, \tag{1.9}$$

where $[K]$ is the *global tangent stiffness matrix* and i is the iteration number [*28*]. The application of load over several steps yields the load-displacement path for a structure and shows how a structure is expected to deform over time. In a non-linear analysis, the system would diverge if all the load is applied in one step.

1.2 Thesis Scope & Structure

The purpose of this research is to develop a 3D rapid linear static analysis capability through the coupling of shell and beam FE in order to model the structural behaviour of the IBGS under a normal operational load case. The work that details the relevant FE formulations and coupling technique required for this analysis is set out as follows.

Chapter 2: Finite Beam Elements reviews the simple theories of bending and torsion and derives the EB beam bending equation. These concepts are used in the formulation of a linear EB beam element that follows.

Chapter 3: Finite Shell Elements begins with a discussion on the similarities between beam, plate and shell elements and then proceeds to discuss the formulation of general shell elements. Two shell element formulations are given and their effectiveness in reproducing

analytical solutions is demonstrated.

Chapter 4: Coupling of Finite Elements explores various techniques to impose multi-point constraint (MPC) equations and reviews existing methods to couple different types of FE. The MPC equations that allow the coupling between EB beam and MITC9 shell elements are developed and verified.

Chapter 5: Numerical Analysis combines the algorithms from the preceding chapters to provide a full static linear analysis of the IBGS. In this analysis, the angle of twist in the jacket is varied in order to investigate the influence of the twisted arrangement on the stresses at each structural joint as well as give an assessment of the overall structural behaviour of the IBGS.

Chapter 6: Conclusion summarises the research presented in this thesis and recommends how the work could be extended to (i) undertake additional numerical analysis of the IBGS and (ii) further develop the concept of coupling between other types of FE, with suggestions for alternative applications.

Throughout, simple benchmark problems are used to demonstrate the work presented. All numerical algorithms were developed and run in MATLAB m-script [*50*] and are outlined in this thesis where appropriate.

Chapter 2

Beam Finite Elements

Beam elements* are used to model prismatic beams with a single, one-dimensional line. In the following, a short discussion on different types of beam elements is given in Section 2.1. The simple theory of bending is reviewed in Section 2.2 and the Euler-Bernoulli (EB) beam bending equation is derived in Sections 2.3. In addition, the simple theory of torsion is reviewed in Section 2.4. These theories are central to the formulation of the EB beam element given in Section 2.5. A comparison between beam and solid elements to accurately model bending behaviour is demonstrated in Section 2.6. Throughout the chapter, the local and global three-dimensional (3D) Cartesian coordinate systems in Figure 2.1 are used, where the local x-axis is in the longitudinal direction of a beam element, measured from node 1. Note that the unit vectors or bases that define the coordinate systems are denoted $\{\hat{e}\}$ with the appropriate axis shown as a subscript, thus the global bases would be $\{\hat{e}_x\}$, $\{\hat{e}_y\}$ and $\{\hat{e}_z\}$ for instance. Where necessary, local variables such as nodal coordinates, strains and stresses are distinguished from their global counterparts by a prime.

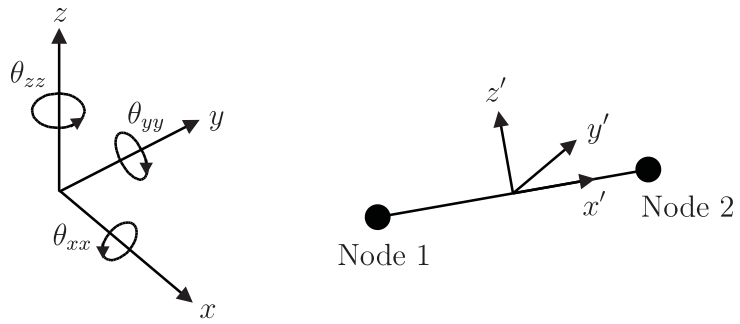

Figure 2.1: Global and local coordinate systems for beam elements.

*The author notes that in some texts, such as in [4], a beam element describes only bending behaviour and a bar/truss element describes longitudinal 'stretching,' whereas a frame element is a structural element that describes both bending and axial (longitudinal 'stretching' and torsion' effects. It is not necessary to make this distinction in this work and so the term beam element is used to encompass both bending and axial effects, unless stated otherwise.

2.1 Types of Beam Elements

In three-dimensions, a typical beam element has six degrees of freedom (DOF): three translations, u, v, w, and three rotations, $\theta_{xx}, \theta_{yy}, \theta_{zz}$, as shown in Figure 2.2. However,

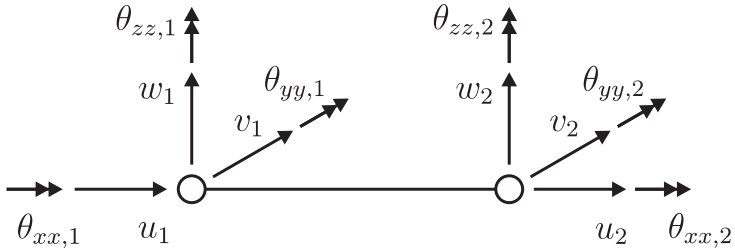

Figure 2.2: DOF for a two-node 3D beam element.

depending on the problem in question, the formulation of a beam element can follow different assumptions, based on theories from classical mechanics. For instance, Euler-Bernoulli (EB)'s beam bending equation is valid for slender beams where the length is much greater than the depth (typically $\frac{L}{d} > 10$) and where it can be assumed that there are no transverse shear deformations [*11*, *44*]. This means that cross-sections remain planar and perpendicular to the neutral axis (NA)[†] during deformation. Nonetheless, in non-slender beams, this assumption is no longer valid as transverse shear strains become significant since plane sections do not remain perpendicular to the NA during deformation, thus inducing shear strains, γ_{xz} and γ_{xy}. In this case, the theory by Timoshenko is followed in which a shear correction factor is included in the element stiffness matrix [*23*] with the assumption that the shear strains remain constant over the cross-section. The shear correction factor is dependent upon Poisson's ratio, though there are various ways in which the shear correction factor can be calculated [*31*, *47*]. For example, one such method is to compare the actual shear strain with the average shear strain [*47*]. In higher order Timoshenko elements, the shear strain might be defined as a parabolic function over the beam depth, allowing the case of warping to be considered [*36*, *55*]. Warping is a characteristic that is more common in thin-walled, open sections and occurs because plane sections become non-planar during deformation. Cook et al. [*23*] suggested that another DOF can be added to each node to describe the rate of twist, $\frac{d\theta_{xx}}{dx}$, in order to impose a restraint to warping. The force associated with this DOF is called a *bimoment*, although it is generally not used in commercial finite element software.

In this work, a linear beam element based on EB beam theory is considered to model straight prismatic members. The theory that underpins this element is derived in the following sections, using the sign convention in Figure 2.3.

[†]The NA is the axis along which the bending stress is equal to zero. For a symmetric and isotropic cross-section, the NA is collinear with the centroid.

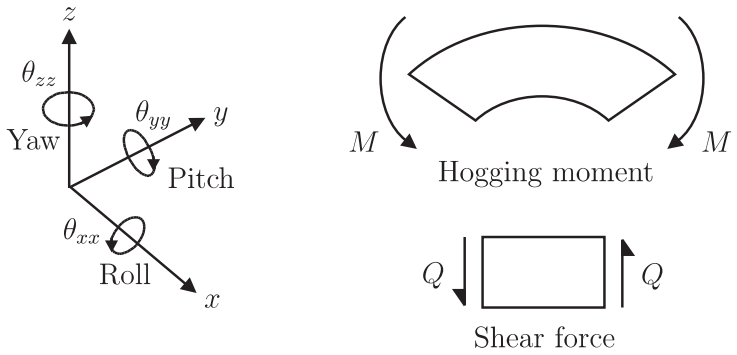

Figure 2.3: Axis orientation and positive sign convention for moments and shear forces.

2.2 Simple Theory of Bending

The simple or elementary theory of bending for a slender prismatic beam was developed by Jacob Bernoulli and Leonhard Euler in the eighteenth century [*38*] and is described in most introductory textbooks on solid mechanics, such as Benham et al. [*11*] and Gere and Goodno [*36*]. The following derivation assumes that plane sections remain plane and perpendicular to the NA during deformation when a pure bending moment is applied. No transverse shear deformation occurs. The beam is assumed to be homogenous, isotropic and elastic, with a symmetric cross-section about the local z'-z' axis. After deformation (in the linear-elastic region), the beam forms a circular arc as pure bending is assumed to occur about a single point, as shown in Figure 2.4. The curvature is constant along the beam as the physical properties and applied bending moment do not vary longitudinally. Figure 2.4 shows a positive hogging moment for a deformed beam that is in tension at the top and in compression at the bottom.

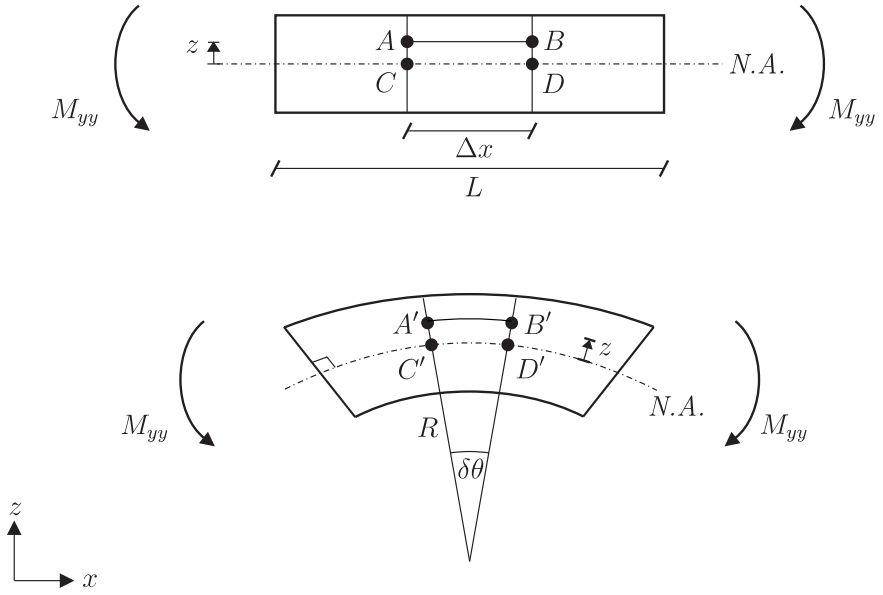

Figure 2.4: Pure bending applied to a slender beam.

The pure bending moment, as applied in Figure 2.4, gives a longitudinal strain defined as.

$$\epsilon_{xx} = \frac{\Delta L}{L}$$
$$\epsilon_{xx} = \frac{A'B' - AB}{AB} .$$

Noting that $AB = CD = C'D' = R\delta\theta$, then

$$\epsilon_{xx} = \frac{(R+z)\delta\theta - R\,\delta\theta}{R\,\delta\theta}$$
$$\epsilon_{xx} = \frac{z}{R} . \tag{2.1}$$

During bending, the beam is assumed to deform according Hooke's Law, where the elastic modulus is

$$E = \frac{\sigma_{xx}}{\epsilon_{xx}} = \frac{\sigma_{xx}}{\frac{z}{R}} . \tag{2.2}$$

This can be rewritten as

$$\frac{E}{R} = \frac{\sigma_{xx}}{z} . \tag{2.3}$$

To link the longitudinal strain to the applied bending moment, the stress over a portion of area ΔA in the cross-section of the beam is considered, as shown in Figure 2.5. The stress

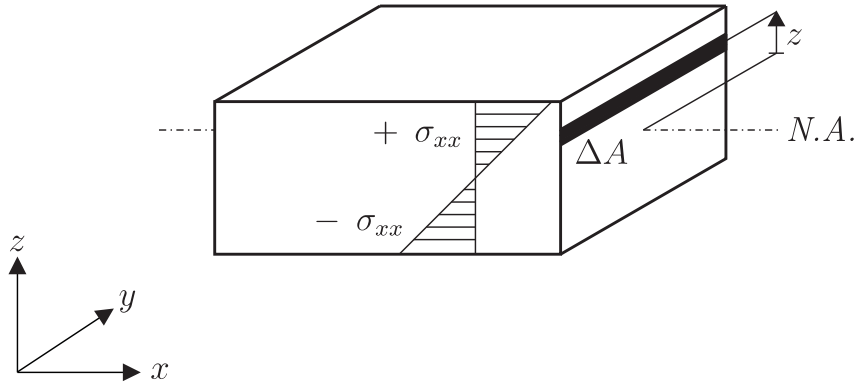

Figure 2.5: Beam cross-section with an element of area ΔA.

over the area ΔA gives an internal force, such that

$$f_{xx}^{int} = \sigma_{xx}\,\Delta A . \tag{2.4}$$

Assuming static equilibrium, the sum of the tensile forces above the NA equal the sum of the compressive forces below the NA. The internal moment acting on the element in Figure 2.5 is equal to product of the internal force and the lever arm, which is the distance z from the

NA, such that

$$M_{yy}^{int} = \sigma_{xx}\,\Delta A\,z\,. \tag{2.5}$$

Since static equilibrium is assumed, the external moment applied to the beam is equal to the sum of all the internal moments over the cross-section, thus

$$M_{yy} = \int \sigma_{xx}\,z\,dA\,. \tag{2.6}$$

By rearranging (2.3) and substituting for σ_{xx} in (2.6), it is seen that

$$M_{yy} = \frac{E}{R}\int z^2\,dA\,. \tag{2.7}$$

Here it is noted that $\int z^2\,dA$ is the second moment of area, I_{yy}, which describes the distribution of cross-sectional area about the NA and is parallel to the local y'-axis. For hollow circular and rectangular members respectively, the second moment of area is

$$I_{yy,\,circular} = \frac{\pi}{4}(R_{ext}^2 - R_{int}^2) \quad \text{and} \quad I_{yy,\,rectangular} = \frac{bd^3}{12}\,. \tag{2.8}$$

On combining (2.3) and (2.7), the equation for the simple theory of bending[‡] is obtained:

$$\frac{M_{yy}}{I_{yy}} = \frac{\sigma_{xx}}{z} = \frac{E}{R}\,. \tag{2.9}$$

This relationship links the geometry, applied moment and stress of a slender beam.

2.3 Euler-Bernoulli Beam Theory

In order to relate the external moment applied to the curvature of the deformed beam, and so derive the EB beam bending equation, first consider a small element of a beam of length Δx, as shown in Figure 2.4$_i$. After bending, as shown in Figure 2.6 the arc length of

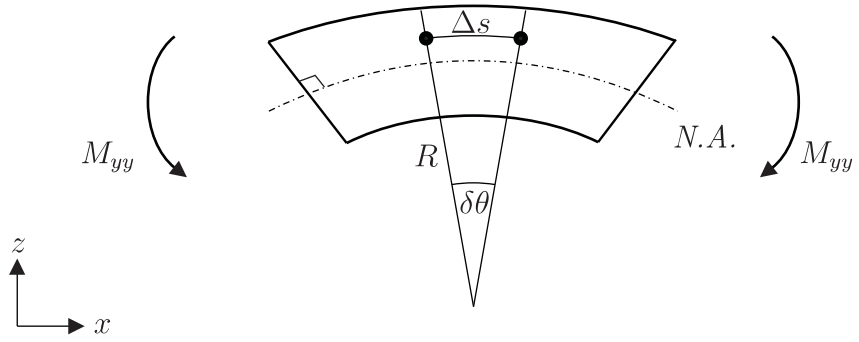

Figure 2.6: Deformed beam with radius of curvature R.

[‡]For bending about the local z' axis, the simple theory of bending is $\frac{M_{zz}}{I_{zz}} = \frac{\sigma_{xx}}{y} = \frac{E}{R}$.

this element is given by

$$ds = R\,d\theta \tag{2.10}$$

where $d\theta$ is the infinitesimal angle between the normals of the tangents at two points along the deflected beam. The expression for the arc length of the element can be rearranged to give the curvature, as

$$\frac{1}{R} = \frac{d\theta}{ds}\,. \tag{2.11}$$

With the assumption of small angles, the arc length of the element, ds, is approximately equal to the original element length, dx. In addition, $\tan\theta$ is approximately equal to θ, where

$$\theta \approx \tan\theta = \frac{dw}{dx}\,. \tag{2.12}$$

By substituting for ds and θ in equation (2.11), the curvature can be rewritten as

$$\frac{1}{R} = \frac{d}{dx}\left(\frac{dw}{dx}\right) = \frac{d^2w}{dx^2}\,. \tag{2.13}$$

EB's beam bending equation is obtained by substituting (2.13) into (2.9) and rearranging, such that

$$M_{yy} = EI_{yy}\,\frac{d^2w}{dx^2}\,, \tag{2.14}$$

where EI_{yy} is termed the *flexural stiffness*. The slope of the deflection (or rotation) is found by integrating the expression in (2.14) once. To find the vertical displacement of the beam, equation (2.14) should be integrated twice, as demonstrated in the beam element formulation in Section 2.5.

2.4 Simple Theory of Torsion

The beam element formulation given in Section 2.5 allows for axial effects and so it is valuable to give a brief review of the simple theory of torsion here. Torsion is the twisting moment or applied torque, T, to a member about its longitudinal axis, as shown in Figure 2.7. Here, a thin-walled cylinder is considered where cross-sections remain plane and the radius remains straight during twisting. On applying equal and opposite torques to each end and assuming that the angle of twist, θ_{xx} remains uniform along the length of the member, the arc length through which a point on the circumference of the tube moves is

$$ds = R\theta_{xx}\,. \tag{2.15}$$

Along the length of the member, the arc length is equal to

$$ds = \gamma L\,, \tag{2.16}$$

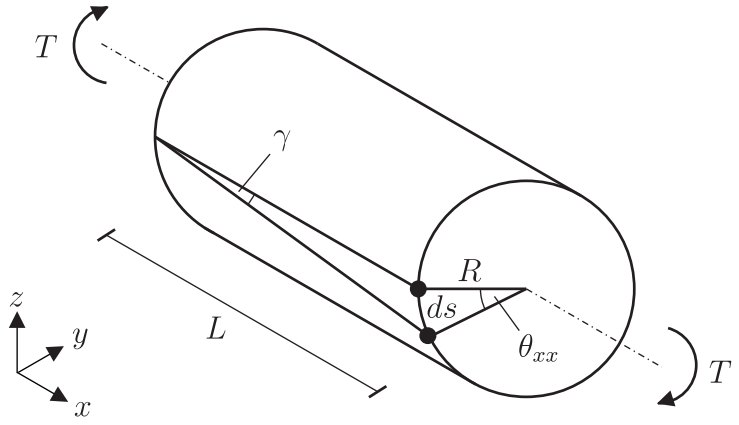

Figure 2.7: Torsion of a thin-walled cylinder.

where γ is the shear strain induced from the applied torque. Equating (2.15) and (2.16), the shear strain is equal to

$$\gamma = \frac{R\theta_{xx}}{L}\,. \tag{2.17}$$

The shear stress, τ, is given by

$$\tau = G\gamma = G\frac{R\theta_{xx}}{L}\,, \tag{2.18}$$

where G is the shear modulus. For any element of area equal to

$$dA = 2\pi R dR\,, \tag{2.19}$$

the internal tangential shear force is

$$f_{int} = \tau dA = \tau 2\pi R dR\,. \tag{2.20}$$

The applied torque is equal to the sum of the internal shear forces over the cross-section, such that

$$T = \int_0^R R f_{int} = \int_0^R 2\pi R^2 \tau dR\,. \tag{2.21}$$

Substituting for shear stress using (2.18), then

$$T = \frac{G\theta_{xx}}{L} 2\pi \int_0^R R^3 dR\,, \tag{2.22}$$

where $2\pi \int_0^R R^3 dR$ is the torsion constant, J. For circular sections, the torsion constant is equal to the polar second moment of area[§], I_p. For hollow cylinders and thin-rectangular

[§]The polar second moment of area is a moment of area about an axis perpendicular (instead of parallel) to the cross-section and can be defined in terms of polar coordinates for a circular section. Alternatively, the polar second moment of area for a circular section is the sum of the second moment of areas in the y'- and z'- directions

plates, the respective torsion constants are

$$J_{circular} = I_p = \frac{\pi}{2}(R_{ext}^4 - R_{int}^4) \quad \text{and} \quad J_{rectangular} \approx \frac{bt^3}{3} \,. \tag{2.23}$$

On combining (2.22) and (2.18), the simple theory of torsion is obtained:

$$\frac{T}{J} = \frac{G\theta}{L} = \frac{\tau}{R} \,. \tag{2.24}$$

This expression relates the applied torque and section properties as well as the resulting angle of twist and shear stress for a thin-walled circular member.

2.5 3D Euler-Bernoulli Beam Element Formulation

The 3D EB beam element is a linear finite element with a node at each end of the neutral (x-x) axis. As shown in Figure 2.2, the two nodes each have six DOF, giving a twelve-by-twelve element stiffness matrix, $[K_b^{e'}]$ [*23*]. By enforcing the boundary conditions shown in Figure 2.8, the stiffness coefficient, $[K_b^{e'}]$, can be determined for each case in the form

$$\{f_{ext}\} = [K_b^{e'}]\,\{d\} \,, \tag{2.25}$$

where $[K_b^{e'}]$ is a matrix comprised of material and geometric properties, defined in the local coordinate system.

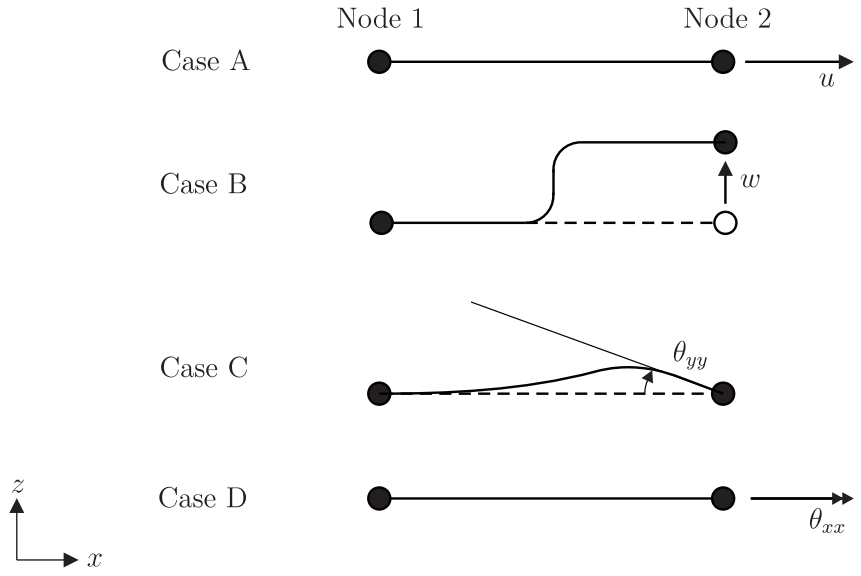

Figure 2.8: Boundary conditions applied to a slender beam at node 2.

Figure 2.8 shows a beam of length L and cross-sectional area A. In case A, a displacement is enforced at node 2 to simulate applying an axial force, $f_{xx,2}$. Expressions can be written for

the stress and strain at each node and related through Young's modulus.

$$E = \frac{\sigma_{xx}}{\epsilon_{xx}} = \frac{\frac{f_{xx}}{A}}{\frac{u_2 - u_1}{L}} \tag{2.26}$$

Rearranging and using $u_1 = 0$, it is found that

$$f_{xx,2} = \frac{EA}{L}\, u_2 \,, \tag{2.27}$$

where the stiffness term $\frac{EA}{L}$ describes the resistance of the beam when subjected to an axial force. For equilibrium,

$$f_{xx,1} = -\,\frac{EA}{L}\, u_2 \,. \tag{2.28}$$

In case B in Figure 2.8, a fully fixed beam is subjected to a transverse unit displacement at node 2 and is evaluated using the EB bending equation. Firstly, an expression is written for the moments about node 2 and then substituted into equation (2.14). Secondly, this expression is integrated twice, with respect to x, to obtain the relationships for the rotation and deflection of the beam, as shown in (2.29).

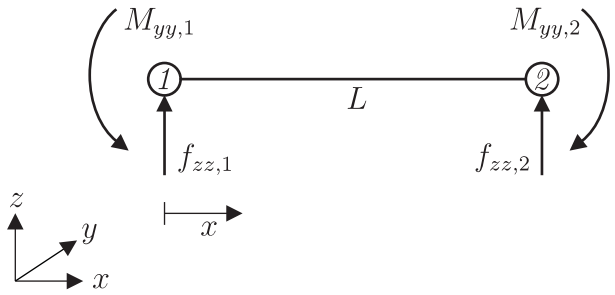

Figure 2.9: Two-node beam element with an applied moment.

$$\begin{aligned}
EI_{yy}\,\frac{d^2w}{dx^2} &= \;\; M \\
EI_{yy}\,\frac{d^2w}{dx^2} &= -\;\; f_{zz.1}\,x \;\; + M_{yy,1} \\
EI_{yy}\,\frac{dw}{dx} \;\; &= -\;\; \frac{f_{zz,1}\,x^2}{2} + M_{yy,1}\,x \quad\; + A \\
EI_{yy}\,w \quad &= -\;\; \frac{f_{zz,1}\,x^3}{6} + \frac{M_{yy,1}\,x^2}{2} + A\,x + B
\end{aligned} \tag{2.29}$$

It is seen that the integration constants A and B are equal to zero when the following boundary conditions are prescribed:

$$\text{At } x = 0\,, \quad \frac{dw}{dx} = 0 \quad \text{and} \quad w = 0\,. \tag{2.30}$$

By changing (2.30) to enforce the boundary condition that w equals some positive vertical displacement, δw_2, at $x = L$, it is possible to simulate the application of a point load at node 2. Here, the reaction force at node 1 is obtained by rearranging $(2.29)_3$.

$$f_{zz,1} = \frac{2M_{yy,1}}{L} \tag{2.31}$$

Substituting for w and $f_{zz,1}$ in equation $(2.29)_4$ and simplifying, the moment at node 1 is given as

$$M_{yy,1} = \frac{6EI_{yy}}{L^2}\,\delta w_2\,. \tag{2.32}$$

Rearranging equation (2.31) and substituting for $M_{yy,1}$ into , the reaction at node 1 is

$$f_{zz,1} = -\frac{12EI_{yy}}{L^3}\,\delta w_2\,. \tag{2.33}$$

By taking moments about node 1 and applying the same boundary conditions, it is found that

$$f_{zz,2} = \frac{12EI_{yy}}{L^3}\,\delta w_2 \quad \text{and} \quad M_{yy,2} = \frac{6EI_{yy}}{L^2}\,\delta w_2\,. \tag{2.34}$$

Similarly, case B can be repeated to find f_{yy} and M_{zz} at each node for the boundary condition that $w = \delta v_2$.

In Case C in Figure 2.8, a unit rotation is applied to the fully fixed beam at node 2 and is enforced by changing the boundary condition in (2.30) such that $\frac{dw}{dx} = \delta\theta_{yy,2}$, at $x = L$. This simulates an applied moment, $M_{yy,2}$, for which the reaction force from $(2.29)_4$ at node 1 is

$$f_{zz,1} = \frac{3M_{yy,2}}{L}\,. \tag{2.35}$$

Substituting for $\frac{dw}{dx}$ and $f_{zz,1}$ in equation $(2.29)_3$, the moment at node 1 is given as

$$M_{yy,1} = \frac{2EI_{yy}}{L}\,\delta\theta_{yy,2}\,. \tag{2.36}$$

Rearranging equation (2.35) and substituting for $M_{yy,1}$ into (2.36), the reaction at node 1 is

$$f_{zz,1} = -\frac{6EI_{yy}}{L^2}\,\delta\theta_{yy,2}\,. \tag{2.37}$$

By taking moments about node 1, the moment and reaction at node 2 for case C are

$$f_{zz,2} = \frac{6EI_{yy}}{L^2}\,\delta\theta_{yy,2} \quad \text{and} \quad M_{yy,2} = \frac{4EI_{yy}}{L}\,\delta\theta_{yy,2}\,. \tag{2.38}$$

Similarly, case C can be repeated to find f_{yy} and M_{zz} at each node for the boundary condition $\frac{dw}{dx} = \delta\theta_{zz,2}$.

Finally, case D in Figure 2.8 illustrates a torque applied to the beam with shear modulus, G, and a torsion constant, J. By using the equation for the simple theory of torsion in (2.24), then

$$M_{xx,1} = -\frac{GJ}{L}\,\theta_{xx,\,2} \tag{2.39}$$

where $\frac{GJ}{L}$ is the torsional stiffness of the beam. For equilibrium,

$$M_{xx,2} = \frac{GJ}{L}\,\theta_{xx,\,2}\,. \tag{2.40}$$

On using the stiffness coefficients in the results found in cases A-D, and by noting that the element stiffness matrix is symmetric (or by working through cases A-D for these boundary conditions applied at node 1), the complete 3D beam element stiffness matrix can be written in the form

$$\{f_{ext}\} = [K_b^e]^{-1}\,\{d\}\,. \tag{2.41}$$

The twelve-by-twelve stiffness matrix is shown in Appendix A where the rows relate to forces/moments and the columns relate to displacements.

In a finite element program, in order that the element stiffness matrix can be populated with the terms in accordance with Figure 2.1 and the derivation above, the local orientation of each beam element can be defined by finding the direction of one of the local axes, e.g. calculate $\{\hat{e}_{x'}\}$. This is achieved either by finding the unit direction vector between the two nodes or by using trigonometry. The other local axes can be then be found so that a local orthogonal basis is formed. Once fully populated, the local element stiffness matrix must be rotated to align with the global coordinate system using the dot product between the unit vectors that define the local and global axes, such that

$$[K_b^e] = [T_b]^T[K_b^{e'}][T_b] \quad \text{where} \quad [T_b] = \begin{bmatrix} [T] & [0] & [0] & [0] \\ [0] & [T] & [0] & [0] \\ [0] & [0] & [T] & [0] \\ [0] & [0] & [0] & [T] \end{bmatrix} \tag{2.42}$$

$$\text{in which} \quad [T] = \begin{bmatrix} \{\hat{e}_x\}.\{\hat{e}_{x'}\} & \{\hat{e}_x\}.\{\hat{e}_{y'}\} & \{\hat{e}_x\}.\{\hat{e}_{z'}\} \\ \{\hat{e}_y\}.\{\hat{e}_{x'}\} & \{\hat{e}_y\}.\{\hat{e}_{y'}\} & \{\hat{e}_y\}.\{\hat{e}_{z'}\} \\ \{\hat{e}_z\}.\{\hat{e}_{x'}\} & \{\hat{e}_z\}.\{\hat{e}_{y'}\} & \{\hat{e}_z\}.\{\hat{e}_{z'}\} \end{bmatrix}\,.$$

With this in mind, the implementation of the EB beam element formulation is shown in Algorithm 2.1, which is used in the example that follows. Once the global stiffness matrix is obtained, the system can be solved to find the nodal displacements. Stress quantities can then be calculated as required.

Algorithm 2.1 Euler-Bernoulli 3D beam element stiffness matrix formulation

INPUTS:

x, y, z	Global nodal coordinates
$\{\hat{e}_x\}$, $\{\hat{e}_y\}$, $\{\hat{e}_z\}$	Global coordinate base vectors
E	Young's modulus
G	Shear modulus
A	Cross-sectional area
I_{yy}, I_{zz}	Second moment of areas
J	Torsion constant

1:	Define the local orientation of beam element.	$\{\hat{e}_{x'}\}$	
2:	Form the local beam element stiffness matrix.	$[K_b^{e'}]$	Appendix A
3:	Calculate the transformation matrix.	$[T_b]$	(2.42)
4:	Transform the local element stiffness matrix into the global coordinate system.	$[K_b^e]$	(2.42)

OUTPUTS:

$[K_b^e]$	Global beam element stiffness matrix

2.6 Example: Beam vs. Solid Elements for Bending

Consider the simple problem of a cantilever beam of rectangular cross-section with an end point load applied at the free end. The solution according to EB beam theory, using values in Table 2.2, is shown in Figure 2.10. In comparison with using one linear beam element, 100 eight-node (trilinear) solid elements, distributed uniformly in the longitudinal direction, are required to obtain the same deflection within a tolerance of 0.1%, as illustrated in Table 2.3. Although there is negligible difference in the run times here, a larger system would show a clear benefit in using beam elements over solid elements for bending since there are many fewer unknown DOF in the system to be solved, which reduces the amount of computational storage required.

Beam	Solid
$P = 1$ kN	$P = 1$ kN
$L = 1$ m	$L = 1$ m
$b = 0.1$ m	$b = 0.1$ m
$d = 0.1$ m	$d = 0.1$ m
$E = 210$ GPa	$E = 210$ GPa
$G = 80$ GPa	$G = 80$ GPa
	$\nu = 0$
	$\rho = 7800$ kg/m^3
	$g = 9.81$ m/s^2
	8 Gauss points

Table 2.2: Input parameters for the cantilever example to compare beam and solid elements.

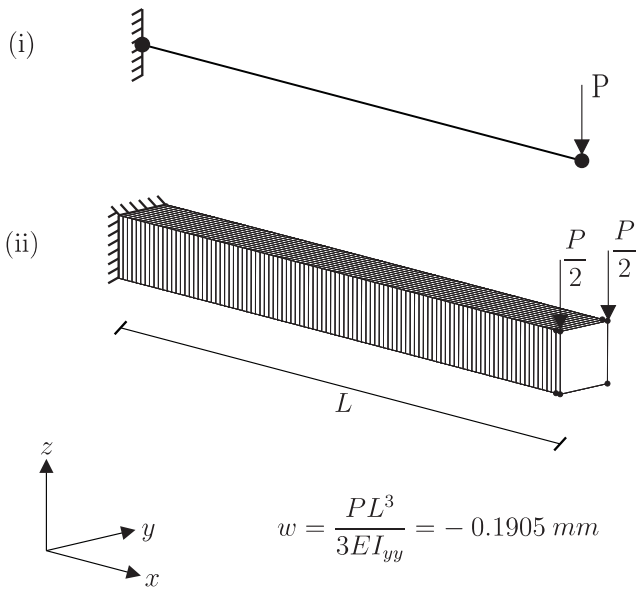

Figure 2.10: Numerical example of a cantilever beam with an end point load modelled with (i) a two-node beam element and (ii) with 100 solid elements. The EB solution for the inputs in Table 2.2 is given.

Element type	Beam	Solid
Number of elements	1	100
Number of DOF	12	1212
Deflection (mm)	-0.1905	-0.1903

Table 2.3: End deflection in mm of a cantilever modelled with beam and solid elements respectively, subjected to an end point load.

2.7 Chapter 2 Summary

In the above, the simple theories of bending and torsion are discussed and the formulation of a linear beam element that satisfies EB beam theory is given. It has been shown that a single beam element is much more effective in capturing bending than hexahedral elements. The linear beam element formulated is employed in Chapter 5 in the numerical analysis of the Inward Battered Guide Structure (IBGS).

Chapter 3

Shell Finite Elements

In effect, shells are simply a more complex type of plate element in that they are designed to model curved surfaces such as containers, nuclear reactor vessels or domed roof structures. In this chapter, the types of shell elements currently available are summarised, followed by a detailed discussion on the formulation and implementation of two general quadrilateral shell elements: the isoparametric degenerate continuum (IDC) shell element [*27*] and the mixed interpolation of tensorial components shell element with nine nodes (MITC9) [*14*]. Small strains as well as material and geometric linearity are assumed throughout and, although the focus is on static linear analysis, some key points are given to show how the work could be extended for geometrically non-linear static analysis. The global and local Cartesian coordinate systems* referred to in this chapter are shown in Figure 3.1. There are three local coordinate axes defined at the element mid-surface, including one for the element, (ξ, η, ζ), in the range -1 to $+1$, one for the Gauss points, $(\xi_{GP}, \eta_{GP}, \zeta_{GP})$, and one for each node, (x'_k, y'_k, z'_k). The mid-surface is always defined by the ξ-η plane. Note that the unit vectors or bases that define the coordinate systems are denoted $\{\hat{e}\}$ with the appropriate axis shown as a subscript. Where necessary, local variables such as nodal coordinates, strains and stresses are distinguished from their global counterparts by a prime.

Throughout this chapter, the simple problem of a cantilever, with an end point load or moment applied, is referred to as a benchmark problem in order to demonstrate the accuracy to which the selected shell elements can reproduce known analytical solutions. Before progressing with the discussion on shell elements, it is useful to highlight the link between beam and plate, and plate and shell elements.

*Often curvilinear coordinates are used for shell element formulations since shells are designed to model curved surfaces. This approach is not adopted here in order that the coordinate systems remain consistent for convenience in developing the beam-shell coupling in Chapter 4.

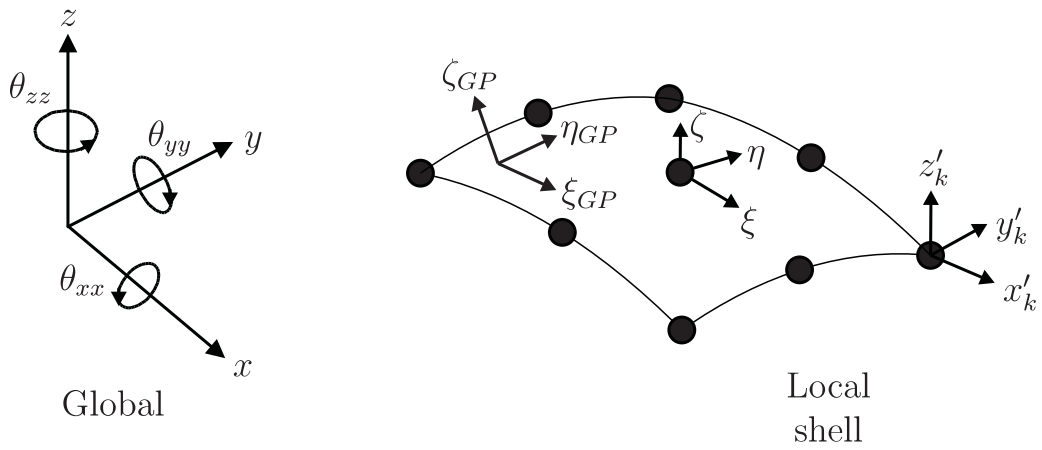

Figure 3.1: Global and local coordinate systems for shell elements.

3.1 Comparison of Beam, Plate and Shell Elements

A plate element is simply a beam element, but with bending occurring in two-directions (and without axial forces or torsion). It is used to describe the deformation of a flat body when subjected to bending whereas a shell element describes the deformation of a curved surface subjected to both bending and membrane actions. In other words, to use the terminology by Astley [*4*], a plate is analogous to a beam element in that only bending behaviour is considered. Similarly, a shell element is analogous to a frame element in that a combination of these actions is considered, as summarised in Figure 3.2. Geometrically, plate and shell

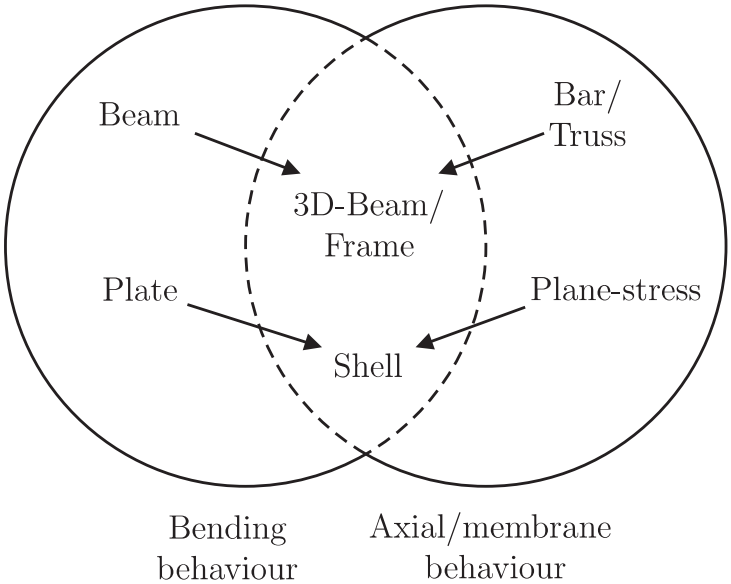

Figure 3.2: Comparison of finite element types.

elements have a thickness that is much smaller than the overall dimensions, where element nodes are located on a neutral plane (in plates) or mid-surface (in shells), located at half of the thickness. In essence, a beam is a 1D element as the nodes lie on a single axis whereas a

plate is a 2D element as all the nodes lie on the same plane, as shown in Figure 3.3. However, depending on the type of formulation, a shell element is often described as either a $2\frac{1}{2}$D element, as not all of the nodes lie in the same plane, or a 3D element, as thick shells are similar in shape to a solid element. All three elements can be used to solve three-dimensional

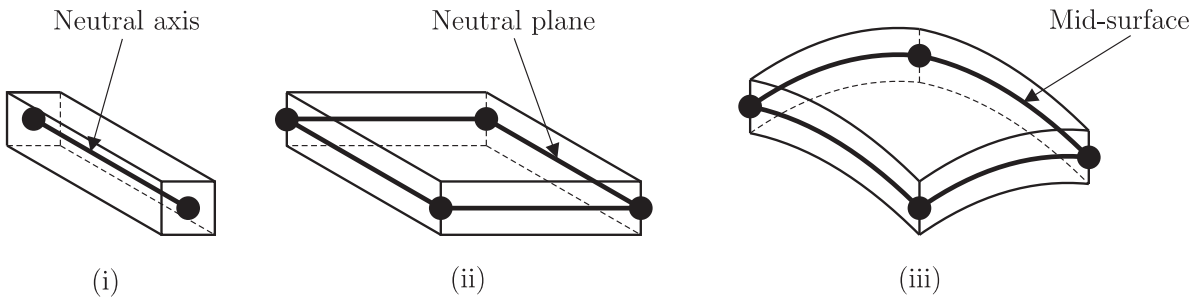

Figure 3.3: Schematic of (i) beam, (ii) plate and (iii) shell elements.

problems more efficiently, especially where bending is dominant, than compared with 3D solid elements, as shown in Sections 2.6 and 3.6. This is because a model with beams, plates and/or shells, will typically have a smaller total number of degrees of freedom (DOF) compared with a model that uses solid elements, thus less data storage is required and the computational efficiency is improved.

Aside from the issue of computational efficiency, there is an additional reason why thin solid elements are not appropriate for use in plate or shell problems. Unless the solid elements used are sufficiently small, issues such as *shear locking* and *ill-conditioning* can arise due to the very small thickness compared with the other dimensions. The problem of shear locking occurs when an element is over-stiff in the thickness direction and so cannot reproduce accurate solutions. By using thin solid elements, there would be two or more nodes along each edge in the thickness direction, which would be very close together. Consequently, abnormally large stiffness coefficients associated with strains in the thickness direction would be induced, dominating the solution and generating spurious strain energy. Since these transverse shear strain components cause a large variation in the magnitude of the stiffness coefficients, the stiffness matrix suffers from ill-conditioning and can become near singular. As noted by Dvorkin et al. [*33*], an example of shear locking is in an early degenerative shell element by Ahmad et al. [*2*], a formulation that is in a sense based on a thin solid element, and is discussed in Section 3.2 with regard to the development of general shell elements. Nevertheless, it is worth noting that the problem of ill-conditioning can be a result of other factors, other than shear locking, such as elements with a poor aspect ratio where one dimension is significantly smaller than the others [*23*, *69*]. The problem of shear locking will be revisited in Section 3.4 with regard to shell elements.

A typical plate element, in addition to the two bending moments, M_{xx} and M_{yy}, has two twisting moments, M_{xy} and M_{yx}, which allow in-plane shear deformation. These moments give

a linear bending stress variation through the thickness of the element and are associated with the curvature of the neutral plane during deformation, as described by the lateral displacement (deflection) and rotation (slope) of the neutral plane at each node. In the case of pure bending, no membrane components (parallel to the neutral plane) of the external force are applied [*4*]. Generally, the normal stress in the thickness direction, σ_{zz}, is considered to be zero when compared with the in-plane normal stresses, σ_{xx} and σ_{yy} [*23*].

There are numerous formulations for plate (and shell) elements and so the reader is directed to work by Hrabok and Hrudey [*41*], Kansara [*46*] and Yang et al. [*68*] for a more extensive review of existing elements. A key reason for the significant number of plate elements available arises from issues with compatibility between elements, as discussed below. Nevertheless, many plate elements rely on the assumptions associated with two classical theories [*4*, *23*, *69*].

Firstly, the Kirchhoff, or thin-plate theory, was developed in 1850. It is comparable to Euler-Bernoulli (EB) beam theory as it is assumed that a straight line perpendicular to the neutral plane remains straight and normal during deformation, provided that deflections are small. This allows transverse shear deformation to be neglected and also assumes that there is no change in the plate thickness during deformation. With this is mind, the deformation of a Kirchhoff plate element is described by the displacement of the neutral plane and the rotation of the normal to the neutral plane, where the bending and twisting moments vary linearly with depth. However, in order to completely satisfy inter-element continuity, the lateral displacement and its derivatives must not only be unique to allow a smooth transition between nodes on adjacent elements, but also be continuous along, above and below the neutral plane. If not, physical discontinuities occur such as distortion in the deformed element where the slope is not continuous along the element edge. Despite this, it is possible to derive elements with partial compatibility that perform well, namely non-conforming Kirchhoff elements [*4*]. Alternatively, the discrepancy in continuity can be avoided by either using separate interpolations for the displacements and rotations, or including Lagrangian multipliers to enforce continuity [*69*].

Secondly, the Mindlin-Reissner plate theory, developed in the mid-twentieth century, is similar to the Timoshenko beam theory in that a straight line perpendicular to the neutral plane remains straight but not normal during deformation. This introduces transverse shear deformation in the x-z and y-z planes, which allows plates of greater thickness to be modelled. As for the Timoshenko beam theory, as discussed in Chapter 2, a shear coefficient, κ, is included in the element stiffness matrix, which is equal to $\frac{5}{6}$ for rectangular cross-sections [*23*, *31*]. However, elements based on the Reissner-Mindlin theory typically exhibit shear-locking when the thickness approaches zero [*4*, *13*]. In other words, as the thickness decreases, transverse shear components become less important and the element should be analogous to a Kirchhoff formulation. Instead, the element behaviour is over-stiff, as discussed in [*23*]. In this case, the

Discrete-Kirchhoff plate element formulation is used, where Kirchhoff constraints are imposed on the Mindlin-Reissner formulation at Gauss-points (GP), in order that shear deformation can be neglected as the thickness approaches zero. In both Reissner-Mindlin and Discrete-Kirchhoff elements, inter-element continuity is achieved.

In contrast to plate elements, shell elements incorporate both bending and membrane actions as illustrated in Figure 3.2. Bending behaviour is caused by forces perpendicular to the mid-surface or applied moments whereas membrane behaviour is caused by forces tangential to the mid-surface. Typically, shell element formulations do not include a rotational DOF about the local ζ-axis, which is often termed the *drilling DOF*. It is worth noting that if the shell mid-surface is flat, not curved, then the shell element is essentially a plate element and a plane-stress element superimposed together where the effects of bending and membrane actions are assessed independently, as demonstrated in work by Kansara [*46*]. Such elements would use a linear geometric interpolation scheme through the element and so would be termed *flat shells* or *facets*. These elements can be used to model curved surfaces and an early example is the triangular shell by Clough and Johnson [*22*]. However, in order to capture the curvature with the same degree of accuracy, a greater number of facets would be required compared with curved shell elements [*69*]. A curved shell element is described by a geometric interpolation scheme of second order or higher, where the bending and membrane actions do interact, that is they cannot be treated independently.

In similarity with the beam and plate elements, the formulation of shell elements can be derived from multiple theories. For instance, the Kirchhoff-Love theory developed in the late nineteenth century is analogous to the thin plate theory assumptions. This theory has been refined by various researchers and has been extended to include shear deformation in thick shells, which is often referred to as a Reissner-Mindlin shell [*12*]. However, often shell elements are not necessarily based on shell theories directly in order to maintain generality. In the next section, the two main approaches in developing general shell elements are discussed.

3.2 Types of General Shell Elements

A general shell element formulation should be suitable for the analysis of both thin and thick plates/shells of arbitrary shape and be applicable to linear and non-linear systems. In addition, the element behaviour must be reliable and its implementation computationally effective [*14*].

To formulate a general shell element, two approaches have been established. Firstly, shell elements can be formulated through the superposition of plane stress and plate bending elements. This approach is suited to the formulation of flat shells or facets, as mentioned in Section 3.1. Secondly, shell elements can be formed through the use of degenerated isoparametric continuum elements, as illustrated in Figure 3.4. The latter approach provides the most general shell element formulation as it is not dependent upon any shell theory. In addition,

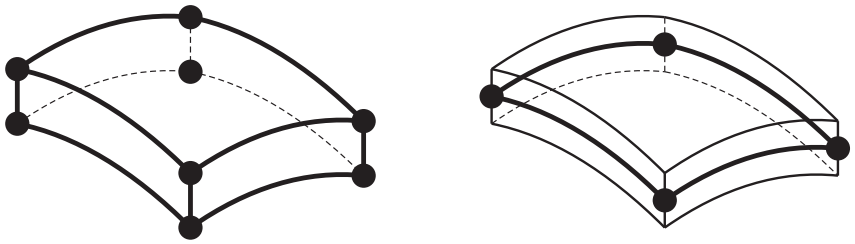

Figure 3.4: Schematic of degenerative shell elements: (i) solid element and (ii) shell.

inter-element continuity is satisfied since the displacements and rotations at the mid-surface are independent, i.e. in contrast to elements derived from shell theories, the rotations are not derived from the displacements [*5*]. The first degenerative shell element was formulated by Ahmad et al. [*2*], whose work was extended by Ramm [*56*] and Bathe and Bolourchi [*7*] for non-linear problems with the assumption of small deformation (small displacements and rotations). These formulations have been further developed to allow for large deformations (large displacements and rotations), as discussed in [*5*, *25*, *27*, *34*, *49*].

In the following section, the isoparametric degenerate continuum (IDC) shell element formulation by de Borst et al. [*27*] is derived. In this work, shell elements of constant thickness are assumed, although it is possible to vary the thickness through the element by defining different thicknesses at each node.

3.3 IDC Shell Element Formulation

The isoparametric degenerate continuum (IDC) shell element detailed here was first developed by Ramm and Matzenmiller in 1986 and is described in work by Stander et al. [*62*] and Crisfield [*25*]. The derivation of this element given in this section follows the formulation arranged by de Borst et al. [*27*], a text which is an updated version of Crisfield's book [*25*].

The IDC shell element is a displacement-based element with five DOF per node; k, three global translations, u_k, v_k and w_k, and two global rotations, $\delta\phi_k$ and $\delta\psi_k$. The two rotations describe the orientation of a normalised global vector, $\{\hat{V}_{n,k}\}$, that is (approximately) perpendicular to the shell mid-surface at each node, as illustrated in Figure 3.5. The angle ϕ_k is measured from the nodal x'-axis to $\{\hat{V}_{n,k}\}$ whereas ψ_k is the angle between the nodal y'-axis and the plane onto which $\{\hat{V}_{n,k}\}$ is projected. The mid-surface normal at each node, k, is defined by

$$\{\hat{V}_{n,k^t}\} = \begin{Bmatrix} \cos\phi_k^t \\ \sin\phi_k^t \cos\psi_k^t \\ \sin\phi_k^t \sin\psi_k^t \end{Bmatrix} , \tag{3.1}$$

where $t = 0$ for the initial configuration. In non-linear analysis, the incremental changes in the local rotations, $\delta\phi_k$ and $\delta\psi_k$, would be used to update angles ϕ_k^t and ψ_k^t and redefine

$\{V_{n,k}^{t+\Delta t}\}$, using

$$\begin{aligned} \phi_k^{t+\Delta t} &= \phi_k^t + \delta\phi_k \\ \psi_k^{t+\Delta t} &= \psi_k^t + \delta\psi_k \,. \end{aligned} \tag{3.2}$$

This step is not necessary for linear analysis since there are only the initial and final configurations to consider.

To define the geometry of the IDC shell element, the following quantities are required for each node, k, as shown in Figure 3.5:

- the global nodal coordinates, x_k, y_k, z_k,
- the angles ϕ_k and ψ_k to define the mid-surface normal vector, $\{\hat{V}_{n,k}^t\}$, and
- the shell thickness, t_k, measured along the mid-surface normal.

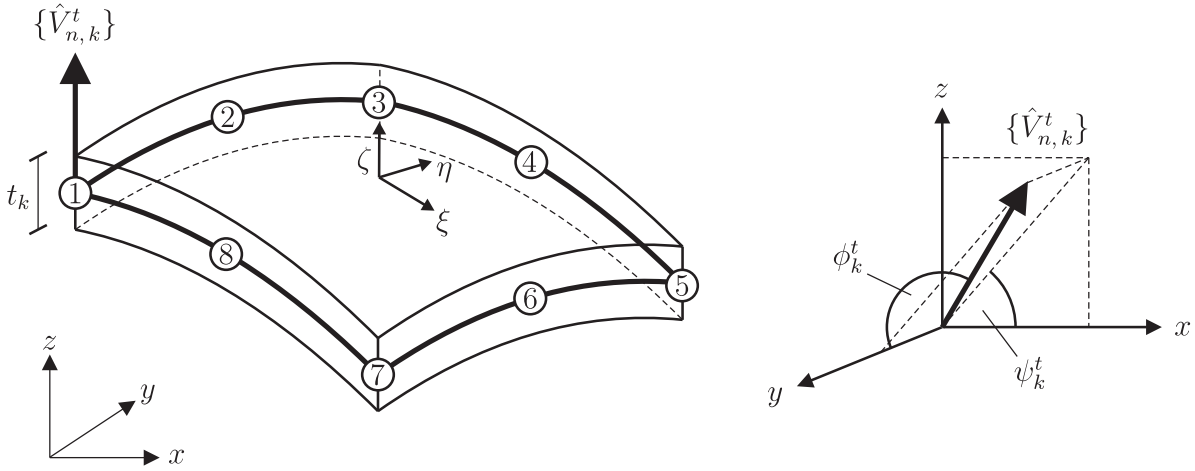

Figure 3.5: Initial geometry for an eight-noded IDC shell element.

The global coordinates of any point within the element are given by

$$\begin{Bmatrix} x^t \\ y^t \\ z^t \end{Bmatrix} = \sum_{k=1}^{8} N_k \begin{Bmatrix} x_k \\ y_k \\ z_k \end{Bmatrix} + t_k \frac{\zeta}{2} \sum_{k=1}^{8} N_k \{\hat{V}_{n,k}^t\} \,, \tag{3.3}$$

where N_k are the shape functions in terms of the in-plane local element coordinates ξ and η. Similarly, since this is an isoparametric element, the incremental nodal displacements are described as

$$\begin{Bmatrix} \delta u_k \\ \delta v_k \\ \delta w_k \end{Bmatrix} = \sum_{k=1}^{8} N_k \begin{Bmatrix} u_k \\ v_k \\ w_k \end{Bmatrix} + t_k \frac{\zeta}{2} \sum_{k=1}^{8} N_k \{\hat{V}_{n,k}^t\} \,. \tag{3.4}$$

In the two equations above, the first term interpolates the coordinates/displacements on the mid-surface and the second term accounts for the thickness and rotation of the element.

The Lagrangian shape functions, N_k, that provide interpolation of these quantities over the mid-surface of an eight-noded element are

$$\begin{aligned}
N_1 &= \frac{1}{4}(1-\xi)(1-\eta)(-\xi-\eta-1) \\
N_2 &= \frac{1}{2}(1-\xi)(1-\eta^2) \\
N_3 &= \frac{1}{4}(1-\xi)(1+\eta)(-\xi+\eta-1) \\
N_4 &= \frac{1}{2}(1-\xi^2)(1+\eta) \\
N_5 &= \frac{1}{4}(1+\xi)(1+\eta)(\xi+\eta-1 \\
N_6 &= \frac{1}{2}(1+\xi)(1-\eta^2) \\
N_7 &= \frac{1}{4}(1+\xi)(1-\eta)(\xi-\eta-1) \\
N_8 &= \frac{1}{2}(1-\xi^2)(1-\eta)\,.
\end{aligned} \tag{3.5}$$

For non-linear analysis, the global nodal coordinates would be updated using the incremental displacements, such that

$$\begin{Bmatrix} x^{t+\Delta t} \\ y^{t+\Delta t} \\ z^{t+\Delta t} \end{Bmatrix} = \begin{Bmatrix} x^{t} \\ y^{t} \\ z^{t} \end{Bmatrix} + \begin{Bmatrix} \delta u \\ \delta v \\ \delta w \end{Bmatrix}\,. \tag{3.6}$$

To find the element stiffness matrix, $[K^e]$, and the internal element force vector, $\{f^e_{int}\}$, as required for finite element analysis (FEA), the expression for equilibrium is obtained from the Principle of Virtual Work, as discussed in Section 1.1. As stated before, this equation equates the stored strain energy (element stiffness) to the external work done due to a virtual (or imaginary) incremental displacement, that is

$$\underbrace{\int_{V^0} \{\bar{\delta\gamma}\}^T\{\delta\tau\}dV^0}_{\text{Incremental strain energy}} + \underbrace{\int_{V^0} \{\bar{\delta\gamma}\}^T\{\tau^t\}dV^0}_{\text{Current strain energy}} = \underbrace{\int_{S^0} \{\bar{\delta d}\}^T\{f^0_t\}dS^0 + \int_{V^0} \{\bar{\delta d}\}^T\{f^0_p\}dV^0}_{\text{External forces}}\,. \tag{3.7}$$

Here, τ is the Second Piola-Kirchhoff stress tensor and γ is the Green-Lagrange strain tensor. These are measures of true stress and strain, which are used to allow for a non-linear analysis capability as they are defined with reference to the initial, undeformed configuration. The Green-Lagrange strain is given by

$$[\gamma] = \frac{1}{2}\left[[F]^T[F] - [I]\right]\,, \tag{3.8}$$

in which $[F]$ is the deformation gradient and is calculated from the derivatives of the displace-

ments with respect to the global coordinates (where X denotes x^0 for the initial configuration), such that

$$[F] = [I] + \begin{bmatrix} \frac{\delta u}{\delta X} & \frac{\delta u}{\delta Y} & \frac{\delta u}{\delta Z} \\ \frac{\delta v}{\delta X} & \frac{\delta v}{\delta Y} & \frac{\delta v}{\delta Z} \\ \frac{\delta w}{\delta X} & \frac{\delta w}{\delta Y} & \frac{\delta w}{\delta Z} \end{bmatrix} = \begin{bmatrix} \frac{\delta u}{\delta \xi} & \frac{\delta u}{\delta \eta} & \frac{\delta u}{\delta \zeta} \\ \frac{\delta v}{\delta \xi} & \frac{\delta v}{\delta \eta} & \frac{\delta v}{\delta \zeta} \\ \frac{\delta w}{\delta \xi} & \frac{\delta w}{\delta \eta} & \frac{\delta w}{\delta \zeta} \end{bmatrix} [J]^{-T}, \quad \text{where} \quad [J]^{-T} = \begin{bmatrix} \frac{dX}{d\xi} & \frac{dX}{d\eta} & \frac{dX}{d\zeta} \\ \frac{dY}{d\xi} & \frac{dY}{d\eta} & \frac{dY}{d\zeta} \\ \frac{dZ}{d\xi} & \frac{dZ}{d\eta} & \frac{dZ}{d\zeta} \end{bmatrix}. \tag{3.9}$$

The matrix $[J]$ gives the derivatives of the global coordinates with respect to the local element coordinates and is termed the *Jacobian*. It is worth noting that with the assumption of small strains, where the displacement gradient $[F] \approx [1]$, the Second Piola-Kirchhoff stress and Green-Lagrange strain converge to the Engineering stress and strain quantities, though for completeness, the former measures are used here.

Nevertheless, since small strains are assumed, a linear relation exists between the Green-Lagrange strain and the Piola-Kirchhoff stress for each increment of stored strain energy, such that

$$\{\delta\tau\} = [D']\{\delta\gamma\}, \tag{3.10}$$

with the Green-Lagrange strain vector comprising of

$$\{\gamma\} = \begin{Bmatrix} \gamma_{xx} & \gamma_{yy} & \gamma_{xy} & \gamma_{yz} & \gamma_{xz} \end{Bmatrix}^T. \tag{3.11}$$

Note that there is no γ_{zz} term as the drilling DOF is considered negligible. The local material stiffness matrix, $[D']$ is equal to

$$[D'] = \begin{bmatrix} 1 & \nu & 0 & 0 & 0 \\ \nu & 1 & 0 & 0 & 0 \\ 0 & 0 & \frac{1}{2}(1-\nu) & 0 & 0 \\ 0 & 0 & 0 & \frac{1}{2}\kappa(1-\nu) & 0 \\ 0 & 0 & 0 & 0 & \frac{1}{2}\kappa(1-\nu) \end{bmatrix}, \tag{3.12}$$

and contains Young's modulus, E; Poison's ratio, ν; and a shear correction factor, κ. In this work, the material relations remains linear and so non-linear components refer to geometric non-linearity. With this in mind, the Green-Lagrange strain tensor can be decomposed into linear and non-linear components, such that

$$\{\delta\gamma\} = \{\delta\gamma_L\} + \{\delta\gamma_{NL}\}. \tag{3.13}$$

After substituting for $\{\delta\tau\}$ in (3.7), (3.13) allows the linearisation of (3.7), which is

rearranged to yield

$$\begin{aligned}\int_{V^0}\{\bar{\delta\gamma}_L\}^T[D]\{\delta\gamma_L\}dV^0 + \int_{V^0}\{\delta\bar{\gamma}_{NL}\}^T\{\tau^t\}dV^0 \\ = \int_{S^0}\{\bar{\delta d}\}^T\{f_t^0\}dS_0 + \int_{V^0}\{\bar{\delta d}\}^T\{f_p^0\}dV^0 - \int_{V^0}\{\bar{\delta\gamma}_L\}^T\{\tau^t\}dV^0\,.\end{aligned} \tag{3.14}$$

This equation describes how the sum of the linear and non-linear stiffness components through the element volume are equal to the difference between the external surface traction and point loads, and the internal body forces. Here, $\bar{}$ denotes the virtual quantities.

The linear strain component in the first integral on the left-hand side of (3.14) can be rewritten as

$$\{\delta\gamma_L\} = [B_L]\{\delta d\}\,, \tag{3.15}$$

where $\{\delta d\}$ is a vector containing the displacemtns/rotations at each node and $[B_L]$ is the linear strain-displacement matrix. In the {IDC} shell element, the vector $\{\delta d\}$ is arranged such that all the translations in the model are followed by all the rotations. It follows that the strain-displacement matrix is also partitioned in this manner, thus $[B_L] = \Big[[B_{L,t}],\,[B_{L,r}]\Big]$. $[B_{L,t}]$ is calculated from the product of the deformation gradient, $[F]$, and the derivatives of the shape functions with respect to the local element coordinates are as follows

$$[B_{L,t}] = \begin{bmatrix} F_{11}\frac{\delta N_k}{\delta\xi} & F_{21}\frac{\delta N_k}{\delta\xi} & F_{31}\frac{\delta N_k}{\delta\xi} \\ F_{12}\frac{\delta N_k}{\delta\eta} & F_{22}\frac{\delta N_k}{\delta\eta} & F_{32}\frac{\delta N_k}{\delta\eta} \\ F_{11}\frac{\delta N_k}{\delta\eta} + F_{12}\frac{\delta N_k}{\delta\xi} & F_{21}\frac{\delta N_k}{\delta\eta} + F_{22}\frac{\delta N_k}{\delta\xi} & F_{31}\frac{\delta N_k}{\delta\eta} + F_{32}\frac{\delta N_k}{\delta\xi} \\ F_{12}\frac{\delta N_k}{\delta\zeta} + F_{13}\frac{\delta N_k}{\delta\eta} & F_{22}\frac{\delta N_k}{\delta\zeta} + F_{23}\frac{\delta N_k}{\delta\eta} & F_{32}\frac{\delta N_k}{\delta\zeta} + F_{33}\frac{\delta N_k}{\delta\eta} \\ F_{13}\frac{\delta N_k}{\delta\xi} + F_{11}\frac{\delta N_k}{\delta\zeta} & F_{23}\frac{\delta N_k}{\delta\xi} + F_{21}\frac{\delta N_k}{\delta\zeta} & F_{33}\frac{\delta N_k}{\delta\xi} + F_{31}\frac{\delta N_k}{\delta\zeta} \end{bmatrix}\,. \tag{3.16}$$

In the above, the rows correspond to the strain components in (3.11) and the columns correspond to the translations at each node, namely u_k, v_k and w_k. The second part of the strain-displacement matrix, $[B_{L,r}]$, is calculated by the product of $[B_{L,t}]$ and the derivatives of the mid-surface normal, with respect to the angles ϕ_k and ψ_k, multiplied by the local coordinate ζ. The derivatives for the mid-surface normal at each node, multiplied by the thickness

at each node and are arranged in the matrix $\tilde{V}$, where

$$[V] = \begin{bmatrix} -t_1 \sin\ \phi_1 & 0 & \cdots & 0 & 0 \\ t_1 \cos\ \phi_1 \cos\ \psi_1 & -t_1 \sin\ \phi_1 \sin\ psi_1 & \cdots & 0 & 0 \\ t_1 \cos\ \phi_1 \sin\ \psi_1 & t_1 \sin\ \phi_1 \cos\ \psi_1 & \cdots & 0 & 0 \\ \vdots & \vdots & \ddots & \vdots & \vdots \\ 0 & 0 & \cdots & -t_k \sin\ \phi_k & 0 \\ 0 & 0 & \cdots & t_k \cos\ \phi_k \cos\ \psi_k & -t_k \sin\ \phi_k \sin\ psi_k \\ 0 & 0 & \cdots & t_k \cos\ \phi_k \sin\ \psi_k & t_k \sin\ \phi_k \cos\ \psi_k \end{bmatrix} . \tag{3.17}$$

On combining the separate parts together, the complete linear strain-displacement matrix is

$$[B_L] = \left[[B_{L,t}]\ ,\ \tfrac{\zeta}{2}[B_{L,r}][V] \right] . \tag{3.18}$$

By substituting equations (3.18) into (3.15) and substituting for $\{\gamma_L\}$ in the first integral in (3.14), the linear element stiffness matrix is given by

$$[K_L^e] = \int_{V^0} [B_L]^T [D'][B_L] dV^0 . \tag{3.19}$$

As $[B_L]$ contains terms with respect to the global coordinates, the pre- and post- multiplication of the local material stiffness matrix, $[D']$, ensures it is rotated into the global coordinate system.

Likewise, the non-linear strain component in the second integral on the left-hand side of equation (3.14) can be written as

$$\{\delta\gamma_{NL}\} = [B_{NL}]\{\delta d\} , \tag{3.20}$$

where $[B_{NL}]$ is the geometrically non-linear strain-displacement matrix. As above, $[B_{NL}]$ is partitioned into $[B_{NL,t}]$ and $[B_{NL,r}]$ according to the displacements and rotations respectively, where $[B_{NL}]$ is given by

$$[B_{NL]} = \left[[B_{NL,t}]\ ,\ \tfrac{\zeta}{2}[B_{NL,r}][V] \right] . \tag{3.21}$$

The matrix $[V]$ is defined above and $[B_{NL,t}]$ is

$$[B_{NL,t}] = \begin{bmatrix} \frac{\delta N_k}{\delta \xi} & 0 & 0 \\ \frac{\delta N_k}{\delta \eta} & 0 & 0 \\ \frac{\delta N_k}{\delta \zeta} & 0 & 0 \\ 0 & \frac{\delta N_k}{\delta \xi} & 0 \\ 0 & \frac{\delta N_k}{\delta \eta} & 0 \\ 0 & \frac{\delta N_k}{\delta \zeta} & 0 \\ 0 & 0 & \frac{\delta N_k}{\delta \xi} \\ 0 & 0 & \frac{\delta N_k}{\delta \eta} \\ 0 & 0 & \frac{\delta N_k}{\delta \zeta} \end{bmatrix} . \tag{3.22}$$

It is seen that $[B_{NL}]$ has nine rows to be consistent with using the matrix form of the Second Piola-Kirchhoff stress tensor, $[S]$, as opposed to the vector form with six rows, $\{\tau\}$, thus

$$[S] = \begin{bmatrix} \tau_{xx} & \tau_{xy} & \tau_{xz} & 0 & 0 & 0 & 0 & 0 & 0 \\ \tau_{yx} & \tau_{yy} & \tau_{yz} & 0 & 0 & 0 & 0 & 0 & 0 \\ \tau_{zx} & \tau_{zy} & 0 & 0 & 0 & 0 & 0 & 0 & 0 \\ 0 & 0 & 0 & \tau_{xx} & \tau_{xy} & \tau_{xz} & 0 & 0 & 0 \\ 0 & 0 & 0 & \tau_{yx} & \tau_{yy} & \tau_{yz} & 0 & 0 & 0 \\ 0 & 0 & 0 & \tau_{zx} & \tau_{zy} & 0 & 0 & 0 & 0 \\ 0 & 0 & 0 & 0 & 0 & 0 & \tau_{xx} & \tau_{xy} & \tau_{xz} \\ 0 & 0 & 0 & 0 & 0 & 0 & \tau_{yx} & \tau_{yy} & \tau_{yz} \\ 0 & 0 & 0 & 0 & 0 & 0 & \tau_{zx} & \tau_{zy} & 0 \end{bmatrix} . \tag{3.23}$$

The term τ_{zz} is equal to zero since shells are generally assumed to have no significant stress in the thickness direction. $[S]$ is found by using (3.10) to find $\{\tau\}$ and rewriting in tensor form. By substituting for $\{\gamma_{NL}\}$ into (3.14) and replacing $\{\tau\}$ with $[S]$ to ensure compatibility in matrix multiplication, the non-linear element stiffness matrix is given by

$$[K^e_{NL}] = \int_{V^0} [B_{NL}]^T [S][B_{NL}] dV^0 . \tag{3.24}$$

The complete element stiffness matrix is found by summing the linear and non-linear contributions at each GP, as will be shown in (3.27) and (3.29).

The local internal element force vector is given by the last integral on the right-hand side of equation (3.14). In this case, the vector form of the Second Piola-Kirchhoff stress is used, where

$$\{\tau\} = \begin{Bmatrix} \tau_{xx} & \tau_{yy} & \tau_{xy} & \tau_{yz} & \tau_{xz} \end{Bmatrix}^T . \tag{3.25}$$

By substituting for $\{\gamma_L\}$ in (3.14) and noting that $\{\bar{\delta d}\}^T$ cancels out, the internal element force vector is obtained as

$$\{f^e_{int}\} = \int_{V^0} [B_L]^T \{\tau\} dV^0 \,. \tag{3.26}$$

The integrals for the element stiffness matrix and the internal element force vector are evaluated at the Gauss-points (GP) within each element, where each integral is multiplied by a weight associated with the contribution of the particular GP within the element. In addition, since the integrals are bounded between -1 and $+1$, owing to the definition of the local element coordinate system, then a scalar is required to adjust the integral to the global volume. This is achieved by multiplying by the determinant of the Jacobian matrix, det$[J]$. The expressions for the global stiffness matrix and the global internal force vector evaluated at each GP can be rewritten as follows.

$$[K^{GP}] = [B_L]^T [D'][B_L]\, w_{GP}\, \text{det}[J] + [B_{NL}]^T [S][B_{NL}]\, w_{GP}\, \text{det}[J] \tag{3.27}$$

$$\{f^{GP}_{int}\} = [B_L]^T \{\tau\}\, w_{GP}\, \text{det}[J] \tag{3.28}$$

The summation of these expressions over all the GP gives the full global element stiffness matrix and global internal element force vector, such that

$$[K^e] = \sum_{GP=1}^{n_{GP}} [K^{GP}] \quad \text{and} \tag{3.29}$$

$$\{f^e_{int}\} = \sum_{GP=1}^{n_{GP}} \{f^{GP}_{int}\} \,. \tag{3.30}$$

The implementation of the IDC shell element is shown in the next section.

3.4 Example: Implementation of the IDC Shell

Algorithm 3.1 shows the formulation of an IDC shell element, which can be incorporated as a function into a finite element (FE) code. With the calculation of the linear and non-linear components of the strain-displacement matrix, Algorithm 3.1 can be used in either a linear or a geometrically non-linear FEA program, as required. For linear analysis, superscript $t = 0$ and matrix $[B_{NL}] = [0]$.

Algorithm 3.1 IDC shell element stiffness matrix formulation.

INPUTS:

x_k^t, y_k^t, z_k^t	Global nodal coordinates
ϕ_k^t, ψ_k^t	Global angles to define the mid-surface normal
u_k, v_k, w_k, $\delta\phi_k$, $\delta\psi_k$	Nodal displacements (initially zero)
E	Young's modulus
ν	Poisson's ratio
κ	Shear correction factor
n_{GP}	Number of Gauss-point (GP)
ξ_{GP}, η_{GP}, ζ_{GP}	Local Gauss-points (GP) coordinates
w_{GP}	GP weights

1:	Form the material stiffness matrix.	$[D]$	(3.12)
2:	**for** GP = 1, 2, 2, ..., n_{GP}		
3:	Calculate the shape functions.	N_k	(3.5)
4:	**for** shell node = 1, 2, 3, ..., k		
5:	*For non-linear analysis, update the nodal coordinates and global angles that define the mid-surface normal.*		(3.6), (3.2)
6:	Calculate the mid-surface normal.	$\{\hat{V}_{n,k}^t\}$	(3.1)
7:	Find the derivatives of the mid-surface normals.	$[V_k]$	(3.17)
8:	**end**		
9:	**for** shell node = 1, 2, 3, ..., k		
10:	Calculate the Jacobian matrix.	$[J]$	(3.9)
11:	Calculate the derivatives of the displacements.	$\frac{d\{u,v,w\}^T}{d\{\xi,\eta,\zeta\}^T}$	(3.9)
12:	**end**		
13:	Calculate the deformation gradient.	$[F]$	(3.9)
14:	Calculate the Green-Lagrange strain tensor.	$\{\gamma\}$	(3.10)
15:	Calculate the Second Piola-Kirchhoff stress.	$[S]$, $\{\tau\}$	(3.23), (3.25)
16:	Form the matrix of the derivatives of the mid-surface normals.	$[V]$	(3.17)
17:	Form the linear strain-displacement matrix.	$[B_L]$	(3.18)
18:	Form the non-linear strain-displacement matrix.	$[B_{NL}]$	(3.21)
19:	Find the determinant of the Jacobian matrix.	det$[J]$	
20:	Calculate the global stiffness matrix at this GP.	$[K^{GP}]$	(3.27)
21:	Calculate the global internal force vector at this GP.	$\{f_{int}^{GP}\}$	(3.28)
22:	**end**		
23:	Sum the stiffness and internal force contributions at each Gauss point to obtain the global element stiffness matrix and global element internal force vector.	$[K^e]$, $\{f_{int}^e\}$	(3.29), (3.30)

OUTPUTS:

$[K_s^e]$	Global shell element stiffness matrix.
$\{f_{int,\,s}^e\}$	Global shell internal element force vector.

The implementation of the IDC element with four and eight nodes is demonstrated through modelling a cantilever beam, which is fixed at one end and with a distributed end moment of 1kNm applied to the free end, as shown in Figure 3.6. The inputs in Table 3.2 are used and the boundary conditions (BC) comprise of fixing all the DOF at the root. Second

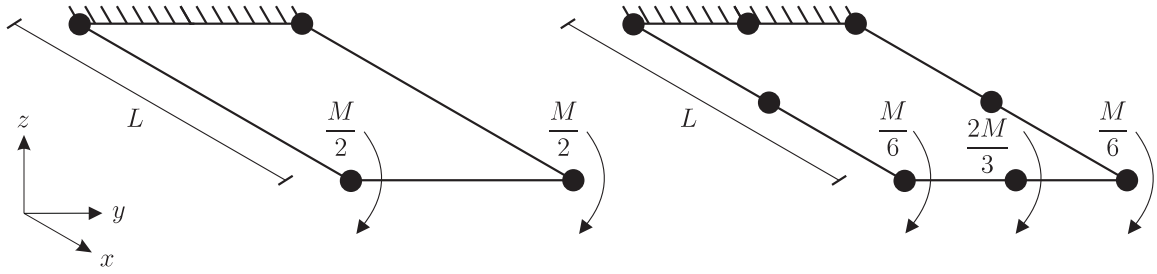

Figure 3.6: Cantilever example of the IDC shell, with a distributed end moment applied to the free end of (i) a four-noded and (ii) an eight-noded element.

Length	L	1 m
Breadth	b	0.1 m
Thickness	t	0.1 m
Young's modulus	E	1 GPa
Poisson's ratio	ν	0
Shear correction factor	κ	1

Table 3.2: Input parameters for the IDC shell element cantilever example.

and third order integration schemes are used for the four and eight noded elements respectively, where the element stiffness matrix and internal force vector are evaluated at each of eight or twenty-seven GP. For the quadratic eight-noded element, the third order integration scheme should provide an exact solution for a second order displacement field. This is reflected in the results in Table 3.3 for when an end moment of 1kNm is applied, which agrees with EB beam theory. However, by applying a distributed end point load of 1kN to this cantilever

	End Moment	**End Point Load**
Analytical Solution	$w = -\frac{ML^2}{2EI_{yy}} = -60$	$w = -\frac{PL^3}{3EI_{yy}} = -40$
4 nodes, 8 Gauss points	$w = -60$	$w = -200\times10^{-3}$
8 nodes, 27 Gauss points	$w = -62$	$w = -200\times10^{-3}$

Table 3.3: Deflection in mm of the IDC shell cantilever example modelled with a four- and eight-noded element respectively, compared with analytical solutions.

with the same input parameters, it is seen in Table 3.3 that the element is over-stiff since the displacement is significantly smaller than expected. There is no improvement in the result if

either more than one element is used in the longitudinal direction, or if the order of integration is reduced from three to two for the eight-noded element. The latter implies that there is a significant problem with shear locking in this element.

In the section that follows, a formulation from the family of mixed interpolation of tensorial components (MITC) shell elements, developed through research led by Bathe at MIT, is derived. Although the formulation is more involved, these elements are considered to be more robust as they provide an effective approach to mitigate shear locking.

3.5 MITC9 Shell Element Formulation

The acronym MITC first appears in 1986 [*8*] to describe a general shell element formulation, which builds upon the work of a four node degenerate solid shell element in [*32*]. The distinctive characteristic in this family of elements is the *mixed formulation* approach whereby separate interpolation functions are used for the in-plane and transverse shear strain components in order to avoid the problem of shear locking [*9*]. In addition, the problem of membrane locking, which becomes apparent in curved geometries, is also avoided. These interpolations are then linked to the usual displacement variables at tying points. Subsequently, the MITC elements could be described as partially isoparametric since the transverse shear strains do not share the same interpolation function as for the in-plane displacements and/or the geometry. Over the last few decades, these elements have been refined, for example by improving the tying of strains and displacement interpolation functions in doubly curved shell problems to provide greater accuracy of the transverse shear components [*10*]. Although these shells have been derived with four, eight, nine and sixteen nodes, the focus here is on the nine-noded MITC element. In this section, the formulation of the MITC9 shell element is given for linear analysis, with the reference to papers by Huang and Hinton [*42*] and Bucalem and Bathe [*14*].

The geometry is defined in a similar fashion to the IDC shell element. For convenience, the initial normalised direction vector at each node on the shell mid-surface is again defined by

$$\{\hat{V}^0_{n,k}\} = \begin{Bmatrix} \cos\phi^0 \\ \sin\phi^0 \cos\psi^0 \\ \sin\phi^0 \sin\psi^0 \end{Bmatrix} . \tag{3.31}$$

This definition is for the initial configuration only, though the mid-surface normal can be updated in non-linear analysis using (3.34) below. Nonetheless, it is worth noting that an alternative way in which to define the mid-surface normal is to input the nodal coordinates of a solid element (instead of the nodal coordinates on the shell mid-surface) and calculate the vector between the corresponding nodes on the lower and upper surfaces. In this way, by not normalising the vector, the thickness, t_k is accounted for and can be removed from (3.35).

In linear analysis, it is assumed that the mid-surface normals remain straight and (approximately) perpendicular during deformation and that transverse shear terms are zero. Since

only in-plane shear terms are considered, no tying points are required and so the formulation that follows is purely isoparametric. There are two additional normalised vectors, $\{\hat{V}^t_{1,k}\}$ and $\{\hat{V}^t_{2,k}\}$, defined at each node, as shown in Figure 3.7, such that

$$\{\hat{V}^t_{1,k}\} = \frac{\{\hat{V}^t_{n,k}\} \times \{\hat{e}_y\}}{\|\{\hat{V}^t_{n,k}\} \times \{\hat{e}_y\}\|_2} \tag{3.32}$$

$$\{\hat{V}^t_{2,k}\} = \frac{\{\hat{V}^t_{n,k}\} \times \{\hat{V}^t_{1,k}\}}{\|\{\hat{V}^t_{n,k}\} \times \{\hat{V}^t_{1,k}\}\|_2} \,. \tag{3.33}$$

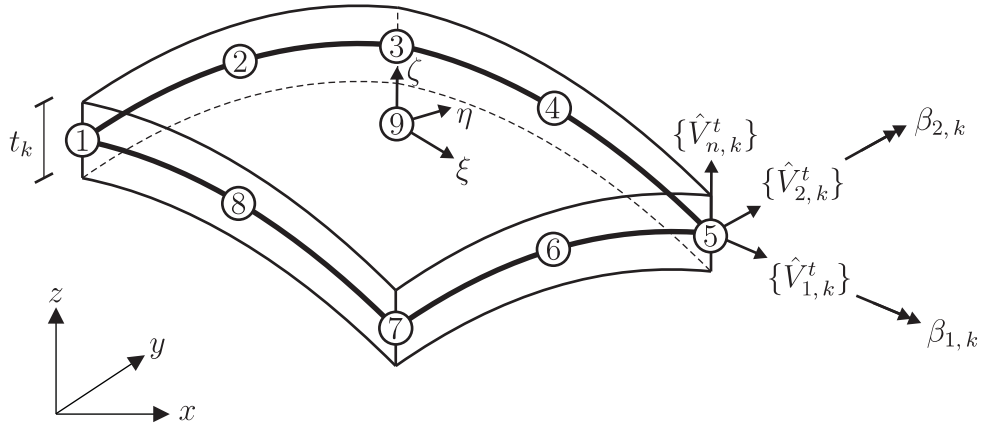

Figure 3.7: MITC9 geometry.

For the case where $\{\hat{V}^t_{n,k}\}$ is collinear with $\{\hat{e}_y\}$, then $\{\hat{V}^t_{1,k}\}$ is defined as $\{\hat{e}_x\}$. All three vectors at each node are initially orthogonal. It is the use of these additional vectors at each node that in part distinguish this formulation from that of the IDC shell. In the MITC9 element, the local rotational DOF, $\beta_{1,k}$ and $\beta_{2,2}$, are defined in a clockwise sense around the vectors $\{\hat{V}^t_{1,k}\}$ and $\{\hat{V}^t_{2,k}\}$ respectively and can be used to express the mid-surface normal in non-linear analysis as

$$\{\hat{V}^{t+\Delta t}_{n,k}\} = \{\hat{V}^t_{n,k}\} + \{\delta\hat{V}_{n,k}\} \quad \text{where} \quad \{\delta\hat{V}_{n,k}\} = \left\{ - \{\hat{V}^t_{2,k}\}\beta_{1,k} + \{\hat{V}^t_{1,k}\}\beta_{2,k} \right\} \,. \tag{3.34}$$

The geometry and incremental displacements are given by

$$\begin{Bmatrix} x^t \\ y^t \\ z^t \end{Bmatrix} = \sum_{k=1}^{9} N_k \begin{Bmatrix} x_k \\ y_k \\ z_k \end{Bmatrix} + t_k \frac{\zeta}{2} \sum_{k=1}^{9} N_k \{\hat{V}^t_{n,k}\} \tag{3.35}$$

$$\begin{Bmatrix} \delta u_k \\ \delta v_k \\ \delta w_k \end{Bmatrix} = \sum_{k=1}^{9} N_k \begin{Bmatrix} u_k \\ v_k \\ w_k \end{Bmatrix} + t_k \frac{\zeta}{2} \sum_{k=1}^{9} N_k \{\hat{V}^t_{n,k}\} \,, \tag{3.36}$$

where the geometry could be updated in non-linear analysis as shown in (3.6). In the above, N_k are the Lagrangian shape functions that are used to interpolate the geometry and displacements over the shell mid-surface. For a nine-noded element, these shape functions are given by

$$\begin{aligned}
N_1 &= \frac{1}{4}\xi(\xi-1)\eta(\eta-1) \\
N_2 &= -\frac{1}{2}\xi(\xi-1)(\eta+1)(\eta-1) \\
N_3 &= \frac{1}{4}\xi(\xi-1)\eta(\eta+1) \\
N_4 &= -\frac{1}{2}(\xi+1)(\xi-1)\eta(\eta+1) \\
N_5 &= \frac{1}{4}\xi(\xi+1)\eta(\eta+1) \\
N_6 &= -\frac{1}{2}\xi(\xi+1)(\eta+1)(\eta-1) \\
N_7 &= \frac{1}{4}\xi(\xi+1)\eta(\eta-1) \\
N_8 &= -\frac{1}{2}(\xi+1)(\xi-1)\eta(\eta-1) \\
N_9 &= (\xi+1)(\xi-1)(\eta+1)(\eta-1)\,.
\end{aligned} \tag{3.37}$$

The advantage of using a nine-noded element is that the middle node provides a more uniform spacing of nodes over the mid-surface, yielding an improved distribution of displacements and stress through the element. On the other hand, the extra node requires an additional five DOF to be solved in each element.

As before, assuming material linearity, the Lagrange strain, $\{\gamma\}$, and the Second Piola-Kirchhoff stress, $\{\tau\}$, are related by the local constitutive matrix, $[D']$,

$$[D'] = \begin{bmatrix}
1 & \nu & 0 & 0 & 0 \\
\nu & 1 & 0 & 0 & 0 \\
0 & 0 & 0 & 0 & 0 \\
0 & 0 & \frac{1}{2}(1-\nu) & 0 & 0 \\
0 & 0 & 0 & \frac{1}{2}\kappa(1-\nu) & 0 \\
0 & 0 & 0 & 0 & \frac{1}{2}\kappa(1-\nu)
\end{bmatrix}. \tag{3.38}$$

Here, a row of zeros for the component in the ζ-ζ direction is included for consistency in matrix operations. To allow for the curved geometry, $[D']$ must be calculated at each GP and transformed to the global coordinate system, using the dot products between the local GP

coordinate basis and the global coordinate basis, thus

$$[D] = [T_s]^T [D'][T_s]\,, \tag{3.39}$$

where $[T_s] =$

$$\begin{bmatrix} l_1\,l_1 & m_1\,m_1 & n_1\,n_1 & l_1\,m_1 & m_1\,n_1 & n_1\,l_1 \\ l_2\,l_2 & m_2\,m_2 & n_2\,n_2 & l_2\,m_2 & m_2\,n_2 & n_2\,l_2 \\ l_3\,l_3 & m_3\,m_3 & n_3\,n_3 & l_3\,m_3 & m_3\,n_3 & n_3\,l_3 \\ 2\,l_1\,l_2 & 2\,m_1\,m_2 & 2\,n_1\,n_2 & l_1\,m_2 + l_2\,m_1 & m_1\,n_2 + m_2\,n_1 & n_1\,l_2 + n_2\,l_1 \\ 2\,l_2\,l_3 & 2\,m_2\,m_3 & 2\,n_2\,n_3 & l_2\,m_3 + l_3\,m_2 & m_2\,n_3 + m_3\,n_2 & n_2\,l_3 + n_3\,l_2 \\ 2\,l_3\,l_1 & 2\,m_3\,m_1 & 2\,n_3\,n_1 & l_3\,m_1 + l_1\,m_3 & m_3\,n_1 + m_1\,n_3 & n_3\,l_1 + n_1\,l_3 \end{bmatrix}$$

$$\begin{aligned} l_1 &= \{\hat{e}_x\}.\{\hat{e}_{\xi_{GP}}\} \quad & m_1 &= \{\hat{e}_y\}.\{\hat{e}_{\xi_{GP}}\} \quad & n_1 &= \{\hat{e}_z\}.\{\hat{e}_{\xi_{GP}}\} \\ l_2 &= \{\hat{e}_x\}.\{\hat{e}_{\eta_{GP}}\} \quad & m_2 &= \{\hat{e}_y\}.\{\hat{e}_{\eta_{GP}}\} \quad & n_2 &= \{\hat{e}_z\}.\{\hat{e}_{\eta_{GP}}\} \\ l_3 &= \{\hat{e}_x\}.\{\hat{e}_{\zeta_{GP}}\} \quad & m_3 &= \{e_y\}.\{\hat{e}_{\zeta_{GP}}\} \quad & n_3 &= \{e\hat{e}_z\}.\{\hat{e}_{\zeta_{GP}}\} \end{aligned}$$

The local orthogonal GP basis vectors can be found using the Jacobian matrix,

$$[J] = \begin{bmatrix} \frac{d\xi_{GP}}{dx} & \frac{d\eta_{GP}}{dx} & \frac{d\zeta_{GP}}{dx} \\ \frac{d\xi_{GP}}{dy} & \frac{d\eta_{GP}}{dy} & \frac{d\zeta_{GP}}{dy} \\ \frac{d\xi_{GP}}{dz} & \frac{d\eta_{GP}}{dz} & \frac{d\zeta_{GP}}{dz} \end{bmatrix} = \begin{bmatrix} \{J_1\} \\ \{J_2\} \\ \{J_3\} \end{bmatrix} \quad \text{to give} \quad \begin{aligned} \{e_{\zeta_{GP}}\} &= \{J_3\} \\ \{e_{\xi_{GP}}\} &= \{J_1\} \times \{e_{\zeta_{GP}}\} \\ \{e_{\eta_{GP}}\} &= \{e_{\xi_{GP}}\} \times \{e_{\zeta_{GP}}\} \end{aligned} \quad . \tag{3.40}$$

By following the principle of virtual work used in the IDC shell formulation in (3.7), and through separating the linear and non-linear strain components as in (3.14), it is possible to arrive at the linear strain-displacement matrix, $[B_L]$. Note that only the first integral in (3.14) and equation (3.15) are used as the non-linear components are approached slightly differently and are beyond the scope of this work. In MITC elements, the displacement vector, $\{d\}$, is formatted such that all the DOF associated with each node are defined together, and so there is no partitioning of $[B]$ with reference to the translations and rotations. The linear strain-displacement matrix is

$$[B_L] = \begin{bmatrix} \frac{dN}{dx} & 0 & 0 & g_{1,x}\,g_{3,x} & g_{2,x}\,g_{3,x} \\ 0 & \frac{dN}{dy} & 0 & g_{1,y}\,g_{3,y} & g_{2,y}\,g_{3,y} \\ 0 & 0 & \frac{dN}{dz} & g_{1,z}\,g_{3,z} & g_{2,z}\,g_{3,z} \\ \frac{dN}{dx} & \frac{dN}{dy} & 0 & g_{1,x}\,g_{3,y} + g_{1,y}g_{3,x} & g_{2,x}\,g_{3,y} + g_{2,y}g_{3,x} \\ 0 & \frac{dN}{dy} & \frac{dN}{dz} & g_{1,y}\,g_{3,z} + g_{1,z}g_{3,y} & g_{2,y}\,g_{3,z} + g_{2,z}g_{3,y} \\ \frac{dN}{dx} & 0 & \frac{dN}{dz} & g_{1,x}\,g_{3,z} + g_{1,z}g_{3,x} & g_{2,x}\,g_{3,z} + g_{2,z}g_{3,x} \end{bmatrix}, \tag{3.41}$$

where

$$\begin{aligned} \{g_1\} &= -\frac{1}{2}t_k\{V_2,\, k\}\,, \\ \{g_2\} &= \frac{1}{2}t_k\{V_1,\, k\}\,, \quad \text{and} \\ \{g_3\} &= \zeta\left(\tfrac{dN}{d(x,y,z)}\right) + \left(J_\zeta^{-1}N\right)\,. \end{aligned} \tag{3.42}$$

The term $\{J_\zeta^{-1}\}$ is the last column of the inverse of the Jacobian matrix in (3.40). The global element stiffness matrix can be calculated as

$$[K^e] = [T_s]^T \left[\sum_{GP=1}^{n_{GP}} [B_L]^T[D][B_L]\, w_{GP}\, \det[J]\right][T_s]\,. \tag{3.43}$$

The global internal element force vector is calculated by

$$\{f_{int}^e\} = [T_s] \sum_{GP=1}^{n_{GP}} [B_L]^T\{\sigma\}\, w_{GP}\, \det[J]\,, \tag{3.44}$$

where $\{\sigma\}$ is the Cauchy or true stress for a linear analysis, given by

$$\{\sigma\} = [D][B_L]\{d\} \tag{3.45}$$

To extend the above formulation to a geometrically non-linear analysis and allow for large deformations, the reader is directed to [*9*] where either a Total or Updated Lagrangian approach can be followed. In the Total Lagrangian formulation, all variables (at $t + \Delta t$) are referred to the original configuration (at $t = 0$) whereas in the Updated Lagrangian formulation, all variables (at $t + \Delta t$) are referred to the previous load step (at t). As an example, the expressions (3.7) and (3.14) above that describes the Principal of Virtual Work are written in a Total Lagrangian form. Both approaches can account for large displacements, large rotations and large strains. For a more in depth and mathematical review of shell geometry and the MITC elements, the reader is directed to [*19*].

3.6 Example: Implementation of the MITC9 Shell

Algorithm 3.2 shows the formulation of a linear MITC family shell element, which can be incorporated as a function into a FE code.

Algorithm 3.2 MITC linear shell element stiffness matrix formulation.

INPUTS:

x_k, y_k, z_k	Global nodal coordinates
$\{\hat{e}_x\}$, $\{\hat{e}_y\}$, $\{\hat{e}_z\}$	Global coordinate base vectors
ϕ_k, ψ_k	Global angles to define the mid-surface normal
u_k, v_k, w_k, $\beta_{1,k}$, $\beta_{2,k}$	Nodal displacements (initially zero)
E	Young's modulus
ν	Poisson's ratio
κ	Shear correction factor
n_{GP}	Number of Gauss-points (GP)
ξ_{GP}, η_{GP}, ζ_{GP}	Local Gauss-point (GP) coordinates
$\{\hat{e}_{\xi_{GP}}\}$, $\{\hat{e}_{\eta_{GP}}\}$, $\{\hat{e}_{\zeta_{GP}}\}$	Local GP coordinate base vectors
w_{GP}	Gauss-point (GP) weights

1:	Calculate the mid-surface normal at each node.	$\{\hat{V}_{n,k}\}$	(3.31)
2:	**for** shell node = 1, 2, 3, ..., k		
3:	Calculate node vector 1.	$\{\hat{V}_{1,k}\}$	(3.32)
4:	Calculate node vector 2.	$\{\hat{V}_{2,k}\}$	(3.33)
5:	Pre-calculate terms for $[B_L]$.	$\{g_1\}$, $\{g_2\}$	(3.42)
6:	**end**		
7:	Form the local material stiffness matrix.	$[D']$	(3.38)
8:	**for** GP = 1, 2, 2, ..., n_{GP}		
9:	Define GP.	ξ_{GP}, η_{GP}, ζ_{GP}	
10:	Calculate the shape functions at this GP.	N_k	(3.5)
11:	Calculate the shape function derivatives.	$\frac{dN}{d\xi}$, $\frac{dN}{d\eta}$	
12:	Form the Jacobian matrix.	$[J]$	(3.40)
13:	Calculate the determinant of the Jacobian.	det$J$	
14:	Calculate the base vectors at this GP.	$\{\hat{e}_{\xi_{GP}}\}$, $\{\hat{e}_{\eta_{GP}}\}$, $\{\hat{e}_{\zeta_{GP}}\}$	(3.40)
15:	Form the transformation matrix by taking the dot product between local element and global base vectors.	$[T_s]$	(3.39)
16:	Transform the material stiffness matrix to the global coordinate system.	$[D]$	(3.39)
17:	Form the strain-displacement matrix.	$[B_L]$	(3.41)
18:	Evaluate the global element stiffness matrix.	$[K^e]$	(3.43)
19:	Calculate the Cauchy stress.	$\{\sigma\}$	(3.45)
20:	Evaluate the global internal element force vector.	$\{f^e_{int}\}$	(3.44)
21:	**end**		

OUTPUTS:

$[K^e_s]$	Global shell element stiffness matrix
$\{f^e_{int,\,s}\}$	Global shell element internal force vector

By using Algorithm 3.2, the implementation of the MITC9 shell element is demonstrated through modelling a cantilever beam, which is fixed at one end with a distributed end moment, end point load, and end torque applied independently to the free end, as illustrated in Figure 3.8. The inputs in Table 3.5 and a third-order Gaussian integration (namely 27 Gauss points) are used, along with the BC stated in Table 3.6.

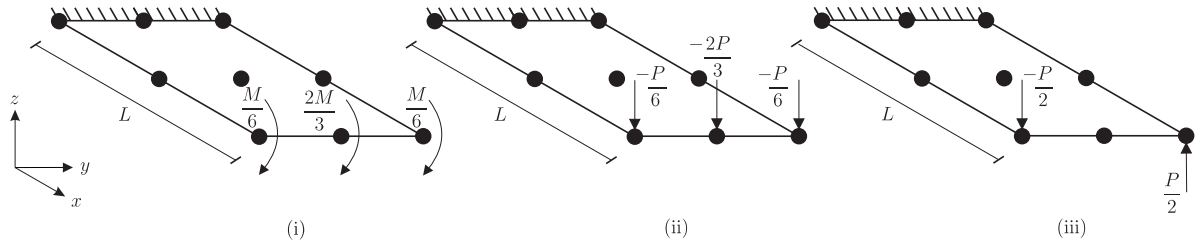

Figure 3.8: Cantilever example for the MITC9 shell with a distributed (i) end moment, (ii) end point load and (iii) end torque applied at the free end.

Length	L	1 m
Breadth	b	1 m
Thickness	t	0.1 m
Young's modulus	E	1 GPa
Shear modulus	G	0.5GPa
Poisson's ratio	ν	0
Shear correction factor	κ	$\frac{5}{6}$

Table 3.5: Input parameters for the MITC9 shell element cantilever example.

The results shown in Table 3.6 demonstrate that this shell element can successfully replicate simple analytical problems to a good degree of accuracy.

	End Point Load, f_{zz} =**1kN**	**End Moment,** M_{yy} =**1kNm**	**End Torque** M_{xx} =**1kNm**
BC	Fix all DOF at the root.	Fix all DOF at the root.	Fix u, v, w and θ_{xx} at the root and θ_{yy} at the middle node at the root.
Analytical Solution	$w = -\frac{ML^2}{2EI_{yy}}$ $w = -6.0 \times 10^{-3}$ mm	$w = -\frac{PL^3}{3EI_{yy}}$ $w = -4.0 \times 10^{-3}$ mm	N/A. N/A.
	$\theta_{yy} = -\frac{ML}{EI_{yy}}$ $\theta_{yy} = -12.0 \times 10^{-6}$ rad	$\theta_{yy} = -\frac{PL^2}{2EI_{yy}}$ $\theta_{yy} = -6.0 \times 10^{-3}$ rad	$\theta_{xx} = \frac{TL}{JG}$ $\theta_{xx} = 6.0 \times 10^{-3}$ rad
MITC9	$w = -6.0 \times 10^{-3}$ mm	$w = -4.0 \times 10^{-3}$ mm	N/A.
	$\beta_2 = -12.0 \times 10^{-6}$ rad	$\beta_2 = -6.0 \times 10^{-3}$ rad	$\beta_1 = 6.0 \times 10^{-3}$ rad

Table 3.6: Solutions for the cantilever example for the MITC9 shell element, compared with analytical solutions.

3.7 Chapter 3 Summary

The derivation and implementation of two shell elements have been shown in this chapter. It was discovered that the IDC shell element was prone to shear locking and could not produce accurate solutions for a cantilever with an end point load, though the result was satisfactory for an end moment. Nevertheless, the MITC9 shell element was found to provide a close approximation when an end moment, end point load and end torque are applied independently and so will be employed in the work that follows.

Chapter 4

Coupling of Finite Elements

In this chapter, the way in which beam and shell elements can be joined together (or *coupled*) is detailed. In order to connect beam and shell elements together, the constraint that the degrees of freedom (DOF) at the coupling interface must be equivalent is imposed. The chapter begins with a discussion on the various methods of imposing constraints with reference to simple examples where appropriate. In Section 4.3, constraint relations are developed that allow the coupling of the Euler-Bernoulli (EB) beam element and the mixed interpolation of tensorial components shell element with nine nodes (MITC9), as formulated in Chapters 2 and 3 respectively. Throughout, the local and global coordinate systems shown in Figure 4.1 are used, where a prime denotes local variables. Please refer to Figures 2.1 and 3.7 for details of element node numbering.

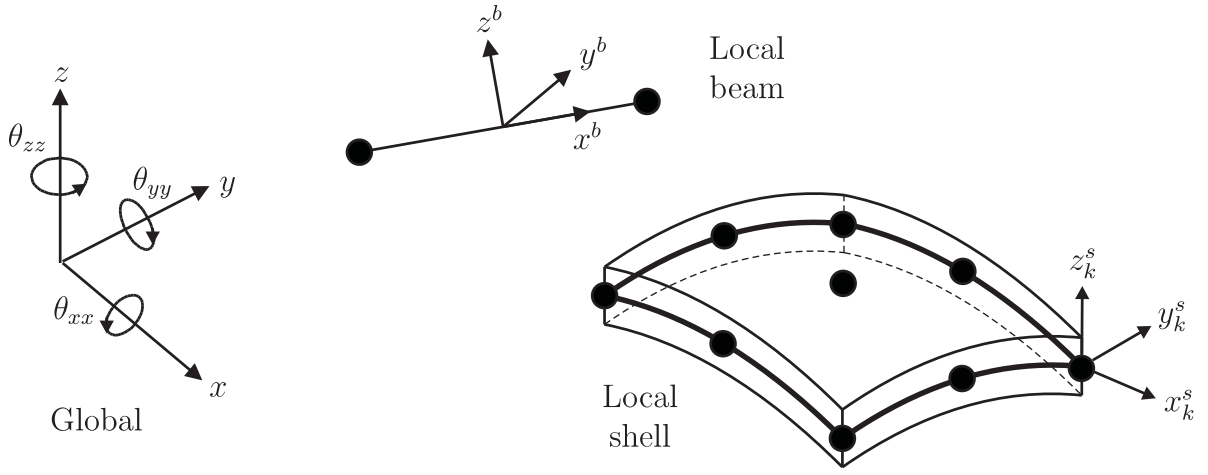

Figure 4.1: Global and local coordinate systems for coupling.

4.1 Coupling Techniques

There are two ways to couple finite elements (FE) of different dimensions (i.e. different DOF per node) in order to ensure compatibility between element types. The first is to employ

transition elements and the second is to develop *constraint equations* that are applied to DOF at the coupling interface between a beam and a shell element. Transition elements require node-to-node coupling and so a specific formulation must be developed for each element combination. According to Ho et al. [*39*], much of the work in this area has been focused on shell-solid transitions, with limited work concerning beam-shell or beam-solid transitions. Often transition elements are prone to locking and although reduced integration has been used to try to avoid this problem, it has been found that hourglass modes (element inversion) can be induced [*39*]. Since the motivation here is to achieve high computational efficiency, then increasing the number of elements in the model is undesirable, hence the remainder of the discussion on coupling methods focuses on how to develop and impose constraint equations.

Typically, constraints are applied in addition to the expressions inherent in the FE model. In general, a single-point constraint prescribes a value to one DOF whereas a multi-point constraint (MPC) enforces a relationship between two or more DOF. These MPC relationships are often described as explicit constraints and are used either to join separate parts of a mesh or elements together, or to introduce an additional relationship into the FE model to describe a specific physical phenomena [*23*]. In displacement based FE formulations, linear MPC equations, $[C]$, prescribe the known differences in displacements, $\{Q\}$, between nodes either side of the constraint (or coupling) interface and can be written in the form

$$[C]\{d\} - \{Q\} = \{0\}\,, \tag{4.1}$$

where $\{d\}$ contains all the translational/rotational DOF in the system [*23*]. In order to achieve FE coupling, there is no change in the displacements at the coupling interface since they are directly equivalent and so the vector $\{Q\}$ in (4.1) is zero. The following discussion compares three ways in which MPC equations can be imposed in FE codes.

4.2 Techniques for Imposing Constraint Equations

Transformation equations, penalty functions and Lagrange multipliers are the three main methods that are used to impose MPC equations. The advantages and disadvantages of these methods are explored here using a simple cantilever beam as an example.

4.2.1 Transformation Equations

Transformation equations eliminate the constrained DOF from the system, thus providing a reduced system in which there are fewer equations to be solved. Ho et al. [*39*] describes this method as a *congruent transformation* since the output is an equivalent system that has not been rotated or transformed in the usual sense. In essence, the stiffness attributed to the nodes condensed out (or removed) is added to the node retained at the coupling interface. This will become clear later in equation (4.5).

An algorithm by Curiskis and Valliappan [*26*] reduces the global stiffness matrix using row and column operations and is a more generalised algorithm compared to work in [*35*] as it is not necessary to prescribe values in the vector $\{Q\}$ in (4.1). To limit the size of these row/column operations, Abel and Shephard [*1*] partitioned the system into unconstrained (*retained*) and constrained (*condensed out*) components; an approach that is developed by Shephard [*60*] to apply a transformation operation to each element as part of the direct assembly of the global stiffness matrix. This work was implemented by Chang and Lin [*18*] with provision for improved data management of the constrained DOF. The work in [*1*] and [*60*] is adapted below, with reference to Cook et al. [*23*].

First, (4.1) is partitioned to correspond to all the DOF retained in the model (subscript r) followed by the DOF to be condensed out (subscript c) at the coupling interface, such that

$$\begin{bmatrix} C_r & C_c \end{bmatrix} \begin{Bmatrix} d_r \\ d_c \end{Bmatrix} - \begin{Bmatrix} Q_r \\ Q_c \end{Bmatrix} = \{0\} \,. \tag{4.2}$$

The dimensions of $[C_c]$ and the number of rows in $[C_r]$ are determined by the number of MPC equations, where there is one expression for each DOF to be condensed out. Typically, $[C_r]$ has more columns than rows as there are more DOF retained compared with the number of MPC equations. Equation (4.2) can then be solved for the DOF to be condensed out, $\{d_c\}$, to give

$$\begin{Bmatrix} d_r \\ d_c \end{Bmatrix} = \begin{bmatrix} [I] \\ -\left[C_c\right]^{-1}\left[C_r\right] \end{bmatrix} \{d_r\} + \begin{Bmatrix} \{0\} \\ \left[C_c\right]^{-1}\{Q\} \end{Bmatrix} \,, \tag{4.3}$$

where the first row correctly implies that the DOF to be retained remain unchanged. This equation can be written more simply as

$$\{d\} = [T]\{d_r\} + \{Q_0\} \,, \tag{4.4}$$

in which $\{Q_0\}$ is the *congruent force vector* that contains prescribed values, $\{Q\}$. $[T]$ is the *congruent transformation matrix* that is used to reduce both the stiffness matrix, $[K]$, and the external force vector, $\{f_{ext}\}$, such that

$$[K^r] = [T]^T[K][T] \tag{4.5}$$

$$\{f^r_{ext}\} = [T]^T(\{f_{ext}\} - [K]\{Q_0\}) \,, \tag{4.6}$$

where the superscript r denotes the reduced system. The system is then solved in the usual manner.

To demonstrate this method, it is helpful to look at a simple problem. Consider the cantilever beam in Figure 4.2, which is fully fixed at the left-hand end and modelled with two 2D Euler-Bernoulli beam elements. A unit point load is applied at the right-hand end. In this

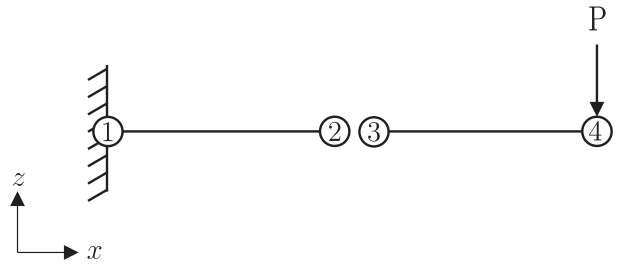

Figure 4.2: Coupling beams between nodes 2 and 3.

example, the aim is to couple node 3 to node 2, thereby eliminating node 3. After applying the boundary conditions, the partitioned vector $\{d\}$ containing the corresponding DOF can be written as

$$\{d\}^T = \{d_r \quad d_c\}^T = \{4\ 5\ 6\ 10\ 11\ 12\ \vdots\ 7\ 8\ 9\}^T .$$

The partitioned $[C]$ matrix containing the MPC equations corresponding to these DOF is

$$[C] = [C_r \quad C_c] = \left[\begin{array}{cccccc:ccc} 1 & 0 & 0 & 0 & 0 & 0 & -1 & 0 & 0 \\ 0 & 1 & 0 & 0 & 0 & 0 & 0 & -1 & 0 \\ 0 & 0 & 1 & 0 & 0 & 0 & 0 & 0 & -1 \end{array}\right]$$

In this case, it can be seen that $[C_c]$ is a negative identity matrix. By substituting $\{d\}$ and $[C]$ into equation (4.4) using (4.3), the congruent transformation matrix, $[T]$, and the congruent force vector, $\{Q_0\}$, are calculated. Through carrying out the operations in equations (4.5) and (4.6), the system to be solved in this example reduces from $[9 \times 9]$ to $[6 \times 6]$, excluding boundary conditions. Although the system size is reduced, there is no change to the equilibrium of the problem and so pre- and post- multiplying by $[T]$ gives additional stiffness at node 2 to account for the elimination of node 3.

Through implementing a similar example using 3D EB beam elements in MATLAB m-script [*50*], it was found that it is easier to apply all the constraints to the global stiffness matrix in one operation, as opposed to one DOF at a time, which avoids problems with relating the final solutions to the correct DOF. Algorithm 4.1 summarises this approach in applying a constraint after the global stiffness matrix assembly and before the system is solved.

While the transformation equation method is known to be numerically stable [*60*], it has the disadvantage of costly matrix operations that would compromise efficiency in a system where a large number of constraints is necessary. These matrix operations also remove the symmetry and increase the bandwidth in the global stiffness matrix [*39*], which increases the storage capacity required. Additional processing is also required at the end of the program to recover the values corresponding to the condensed DOF. An alternative way to impose MPC equations is by using penalty functions, as described below.

Algorithm 4.1 Imposing constraints using transformation equations.

INPUTS:

$[K]$	Global stiffness matrix.
$\{f_{ext}\}$	Global external force vector.

1:	Define DOF at nodes to be condensed out.	$\{d_c\}$	(4.2)
2:	Define all DOF to remain.	$\{d_r\}$	(4.2)
3:	**for** condensed out node = 1, 2, 3, ... , n_{k_c}		
4:	Create partitioned constraint matrix.	$[C_c \quad C_r]$	(4.2)
5:	**end**		
6:	Calculate the congruent transformation matrix.	$[T]$	(4.3)
7:	Calculate the congruent force vector.	$[Q_0]$	(4.3)
8:	Calculate the global reduced stiffness matrix.	$[K^r]$	(4.5)
9:	Calculate the global reduced external force vector.	$\{f^r_{ext}\}$	(4.6)

OUTPUTS:

$[K^r]$	Reduced global stiffness matrix.
$\{f^r_{ext}\}$	Reduced global external force vector.

4.2.2 Penalty Functions

Penalty functions impose constraints by adding the term $\frac{1}{2}\{t\}^T[a]\{t\}$ to the potential energy function [*23*]

$$\Pi_p = \frac{1}{2}\{d\}^T[K]\{d\} - \{d\}^T\{f_{ext}\} - \frac{1}{2}\{t\}^T[a]\{t\}\,. \tag{4.7}$$

The diagonal matrix $[a]$ contains penalty numbers, selected by the Analyst, which approximate how severely the constraint is imposed and the vector $\{t\}$ describes the degree to which the linear MPC equations are satisfied, that is

$$\{t\} = [C]\{d\} - \{Q\}\,. \tag{4.8}$$

As before, the matrix $[C]$, containing the constraint relations, is partitioned as $[C_r \quad C_c]$ and the vector $\{d\}$ is partitioned as $\{d_r \quad d_c\}^T$. By taking the minimum $\{\frac{\partial \Pi_p}{\partial d}\} = \{0\}$, equation (4.7) becomes

$$\Big([K] + [C]^T[a][C]\Big)\{d\} = \{f_{ext}\} + [C]^T[a]\{Q\}\,, \tag{4.9}$$

where $[C]^T[a][C]$ is a penalty matrix.

The left-hand side of equation (4.9) shows that additional stiffness is added to the global stiffness matrix, which can cause two problems [*23*]. Firstly, the topology of the global stiffness matrix is modified, which presents an additional challenge in the efficient management of

storing data relating to the correct DOF. Secondly, and perhaps more importantly, a large addition in stiffness can result in ill-conditioning of the global stiffness matrix, an effect that can lead to a near singular stiffness matrix and also an incorrect solution if the system can be solved. According to Cook et al. [*23*], ill-conditioning can occur when $[a]$ increases, yielding a significant increase in the stiffness at the constraint, where the surrounding region is flexible in comparison. Consequently, the constrained region deforms as a rigid body and this deformation then incorrectly dominates the corresponding strain components. These issues render the penalty functions method unsuitable for the work in this thesis.

In addition to these two problems, since the values of the penalty numbers, $[a]$, must be selected by the Analyst to represent the severity to which the constraints are imposed, this method only provides an approximate way of imposing constraints [*39*]. A further way in which MPC can be imposed is through using Lagrange multipliers, as described below.

4.2.3 Lagrange Multipliers

Lagrange multipliers enable the maximum or minimum of a function whose variables have certain prescribed constraints to be determined. The MPC equations in the form of (4.1) are added to the potential energy function and are pre-multiplied by a row vector, $\{\lambda\}^T$ [*23*]. This constraint term in (4.10) is effectively zero and so the potential energy of the system remains unchanged [*23*].

$$\Pi_p = \frac{1}{2}\{d\}^T[K]\{d\} - \{d\}^T\{f_{ext}\} + \{\lambda\}^T\Big([C]\{d\} - \{Q\}\Big) \tag{4.10}$$

This approach is similar to the penalty method in that there is an additional term in the potential energy expression. However, the use of Lagrange multipliers allows the constraints to be imposed in an exact, rather than an approximate manner. Furthermore, the method can alter the bandwidth in the global stiffness matrix [*39*].

From equation (4.10), by setting $\frac{\partial \Pi_p}{\partial d}$ and $\frac{\partial \Pi_p}{\partial \lambda}$ to zero, the following system of equations is obtained:

$$\begin{bmatrix}[K] & [C]^T \\ [C] & [0]\end{bmatrix}\begin{Bmatrix}\{d\} \\ \{\lambda\}\end{Bmatrix} = \begin{Bmatrix}\{f_{ext}\} \\ \{Q\}\end{Bmatrix} . \tag{4.11}$$

There are different ways of partitioning $[C]$ and $\{d\}$ [*54*], though here, as before, $[C]$ and $\{d\}$ are partitioned by separating the DOF to be retained and constrained. Note that the stiffness matrix, $[K]$, should be also arranged in this order for consistency. The additional unknown terms, $\{\lambda\}$, are the Lagrange multipliers, which can be described as the force applied across the constraint interface. For convenience, (4.11) can be written as

$$[K^c]\{d^c\} = \{f^c_{ext}\} , \tag{4.12}$$

where superscript c denotes constrained. Equation (4.12) can then be solved in the usual

manner to obtain the nodal displacements/rotations and the Lagrange multipliers. Algorithm 4.2 shows how to implement this method, after the assembly of the global stiffness matrix.

Algorithm 4.2 Imposing constraints using Lagrange multipliers.

INPUTS:

$[K]$	Global stiffness matrix.
$\{f_{ext}\}$	Global external force vector.

1:	Define DOF at nodes to be constrained.	$[D_c]$	(4.2)
2:	Define all DOF to remain.	$[D_r]$	(4.2)
3:	**for** condensed out node = 1, 2, 3, ... , n_{k_c}		
4:	Create partitioned constraint matrix.	$[C_r \quad C_c]$	(4.2)
5:	**end**		
6:	Calculate the constrained global stiffness matrix.	$[K^c]$	(4.11)
7:	Calculate the constrained global external force vector.	$\{f^c_{ext}\}$	(4.11)

OUTPUTS:

$[K^c]$	Constrained global stiffness matrix.
$\{f^c_{ext}\}$	Constrained global external force vector.

Since the number of equations to be solved always increases with this method, it is preferable to avoid using this technique, especially for imposing large numbers of constraints. In this regard, the transformation equations method has the clear benefit of always reducing the system of equations to be solved. If there are few constraints to be imposed, then $[C_c]$ used in the transformations equations method is small and so quick to invert, thus concern about the effects of large matrix operations is negligible since the overall system size is reduced. For this reason, the transformation equations is the chosen technique in this thesis.

4.3 Development of Constraint Equations for Beam-Shell Coupling

Linear MPC equations, generally in the form of equation (4.1), relate the translational/ rotational DOF on the MITC9 shell element to the translational/rotational DOF on a EB beam element, as shown in Figure 4.3. In constructing MPC expressions, it is essential to ensure not only that the DOF are compatible between elements of different dimensions but also that there is consistency in the kinematic assumptions associated with the element types at the coupling interface. Whilst there is some literature devoted to the coupling of solid and beam elements including work by Monaghan [*52*], and also to couple solid and shell elements such as in work by Jialin et al. [*43*], there is very little literature that explores the coupling of shell and beam elements.

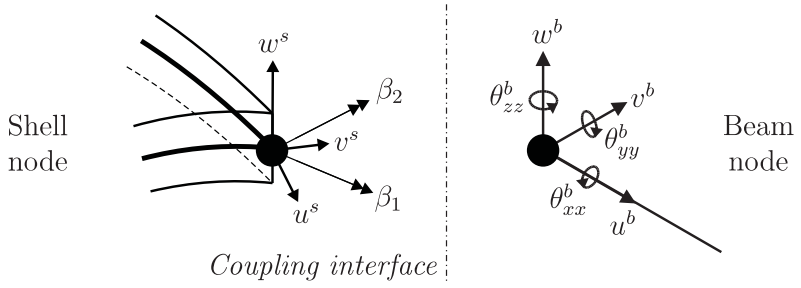

Figure 4.3: DOF on a beam and shell element at the coupling interface.

In order to couple 3D-beam and isoparametric shell elements, Shim et al. [*61*] obtained MPC equations for elastostatic problems through considering the stress equilibrium across the constraint by equating the work done on each side of the constraint interface. The technique was adopted from work by McCune et al. [*51*] to couple beam and solid elements to plate elements. As detailed in [*52*], by evaluating the response from the individual load cases (axial, moments, shear, torque) in terms of the stress present at the constraint, compatible MPC expressions were derived to link the corresponding DOF on either side of the constraint interface. The axial and bending stress contributions were found directly via analytical solutions whereas the shear and torsion stress contributions were determined numerically through analysing a graded 2D mesh at the constraint interface, created from the shell mid-surface normals. Monaghan [*52*] demonstrated that the analysis of a 2D mesh representing the coupling interface provided a more general approach, with greater accuracy, than by considering the problem using thin wall theories since the latter does not capture boundary layer effects or regions of discontinuity near the edges of thin shells. These MPC equations could be applied also to the coupling of beam elements to plane stress/stain and plate elements, instead of shell elements.

More recently, Ho et al. [*40*] developed more general MPC equations that could be applied to either beam-shell, beam-solid or shell-solid element interfaces in explicit finite element analysis (FEA). The technique takes advantage of the capability to manipulate terms at the time integration step and so does not employ any of the more classical approaches described in Section 4.2 to impose the constraints. The position of each node on each element type at the constraint interface is defined with a direction vector, which remains coplanar to this interface during deformation to enforce the assumption that the constraint interface behaves as a rigid body. At each time step, the new direction vector is calculated and compared with the previous direction vector through a central difference formula to determine the new position of the direction vector. The technique was extended subsequently for non-linear dynamic problems [*39*], in which it is also shown that coupling techniques in commercial software insufficiently capture structural behavior across the coupling interface.

In this thesis, MPC equations that provide coupling between 3D EB beam and MITC9 shell elements are developed through a purely geometric derivation. This approach was chosen

for its simplicity and suitability for the assumption of small strains, which is valid for small translations/rotations only and thus allows the trigonometric small angle approximation to be used where appropriate. The coupling interface is assumed to behave as a rigid plate, as shown in Figure 4.4. This is consistent with the kinematic assumptions for both EB beam and MITC9 shell elements, in which plane sections in beams remain plane and normal and shell mid-surface normals remain straight and perpendicular during deformation. In other words, there is no warping or cross-sectional shear in the member (which may not be cylindrical in shape as in Figure 4.4).

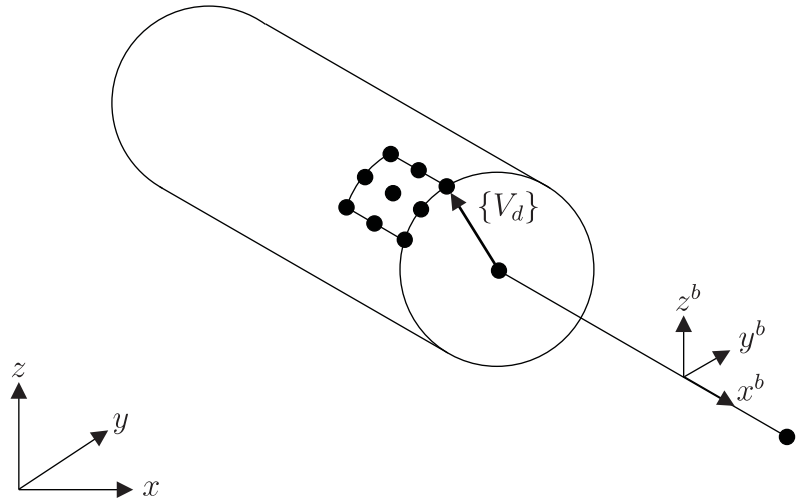

Figure 4.4: Coupling interface between beam and shell elements.

To develop the MPC expressions, the individual translations and rotations on the beam are expressed in terms of the shell DOF and are collated in the form of a $[5 \times 6]$ constraint matrix, $[\tilde{C}]$, such that

$$\underbrace{\begin{Bmatrix} u & v & w & \beta_1 & \beta_2 \end{Bmatrix}^T}_{\text{Shell DOF}} = \begin{bmatrix} \tilde{C} \end{bmatrix} \underbrace{\begin{Bmatrix} u & v & w & \theta_x & \theta_y & \theta_z \end{Bmatrix}^T}_{\text{Beam DOF}}. \tag{4.13}$$

To help determine the influence of the beam DOF on the shell DOF, a direction vector, $\{V_d\}$, is defined from the beam node to each shell node in the original configuration (or previous time step in non-linear analysis) and is coplanar with the coupling interface, as shown in Figure 4.4. This concept stems from work by Ho et al. [*40*]. The change in the components of this vector, when the beam node translates or rotates, are used to form some of the constraint relationships in $[\tilde{C}]$.

To determine the relationships that constitute $[\tilde{C}]$, firstly it is noted that the translations on the beam are directly equivalent to those on the shell. Secondly, to complete the expressions associated with the translational DOF on the shell, the effect of the beam rotations on these DOF are considered, as shown in Figure 4.5, where each beam rotation gives a possible shell

displacement in two directions. These incremental displacements at the shell node due to the

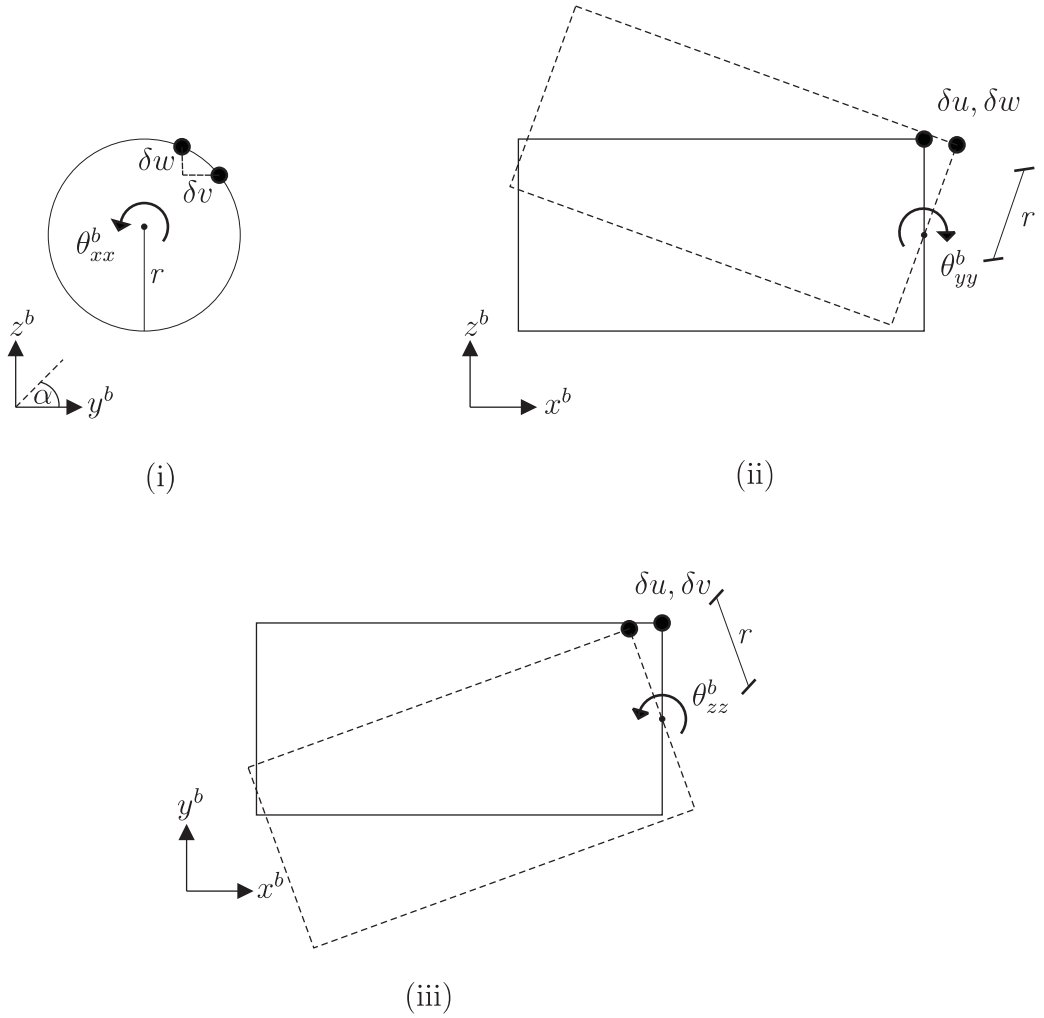

Figure 4.5: Shell translations caused by beam rotations about the (i) x-, (ii) y- and (iii) z-axes.

beam rotations can be described using trigonometric functions. Thus the translational DOF on the shell can be fully expressed as

$$\begin{aligned}
\delta u^s &= u^b + r \sin\theta^b_{yy} \sin\alpha + r \sin\theta^b_{zz} \cos\alpha \\
\delta v^s &= v^b + r\,\theta^b_{xx} \sin\alpha + (r\cos\alpha - r cos\theta^b_{zz} \cos\alpha) \\
\delta w^s &= w^b + r\,\theta^b_{xx} \cos\alpha + (r\sin\alpha - r\cos\theta^b_{yy} \sin\alpha)\,,
\end{aligned} \tag{4.14}$$

where α is the geometric initial position of a shell node on the perimeter of the cross-section, measured anti-clockwise from local beam y-axis. Using small angle approximations, (4.14) is

reduced to

$$\begin{aligned} \delta u^s &= u^b + r\,\theta^b_{yy}\sin\alpha + r\,\theta^b_{zz}\cos\alpha \\ \delta v^s &= v^b + r\,\theta^b_{xx}\sin\alpha \\ \delta w^s &= w^b + r\,\theta^b_{xx}\cos\alpha\,. \end{aligned} \tag{4.15}$$

However, the use of trigonometric functions in (4.15) can lead to programming problems since trigonometric functions are sinusoidal and so developing an appropriate conditional statement to obtain the correct plus / minus sign for these terms is difficult. A more robust and general approach is to write the trigonometric functions in terms of a component of the direction vector, $\{V_d\}$, and so (4.15) is rewritten to give

$$\begin{aligned} \delta u^s &= u^b + V_{d,\,z}\,\theta^b_y - V_{d,\,y}\,\theta^b_z \\ \delta v^s &= v^b - V_{d,\,z}\,\theta^b_x + V_{d,\,x}\,\theta^b_z \\ \delta w^s &= w^b + V_{d,\,y}\,\theta^b_x - V_{d,\,x}\,\theta^b_y\,, \end{aligned} \tag{4.16}$$

where $\{V_d\}$ is given by

$$\{V_d\} = \begin{Bmatrix} x^s \\ y^s \\ z^s \end{Bmatrix}^T - \begin{Bmatrix} x^b \\ y^b \\ z^b \end{Bmatrix}^T \quad . \tag{4.17}$$

In essence, the above allows the original position of each shell node, given by $\{V_d\}$, to be rotated through an angle θ to the new position.

Thirdly, to describe the rotational shell DOF in terms of the beam DOF, it is noted that the translational DOF on the beam have no effect on the rotational DOF on the shell. Finally, to relate the rotational DOF on the beam to those on the shell, a transformation from three to two rotational DOF is required. In the MITC9 shell formulation, two global unit vectors, $\{\hat{V_{1,\,k}}\}$ and $\{\hat{V_{2,\,k}}\}$, are calculated at each node, around which the shell rotations, $\beta_{1,\,k}$ and $\beta_{2,\,k}$, are defined. These two vectors provide the necessary transformation between the rotational DOF on the beam and shell elements.

Through collating the relationships described, the complete constraint matrix is

$$\begin{Bmatrix} u \\ v \\ w \\ \beta_1 \\ \beta_2 \end{Bmatrix}^T = \begin{bmatrix} 1 & 0 & 0 & 0 & V_{d,\,z} & -V_{d,\,y} \\ 0 & 1 & 0 & -V_{d,\,z} & 0 & V_{d,\,x} \\ 0 & 0 & 1 & V_{d,\,y} & -V_{d,\,x} & 0 \\ 0 & 0 & 0 & \hat{V}_{1,\,x} & \hat{V}_{1,\,y} & \hat{V}_{1,\,z} \\ 0 & 0 & 0 & \hat{V}_{2,\,x} & \hat{V}_{2,\,y} & \hat{V}_{2,\,z} \end{bmatrix} \begin{Bmatrix} u \\ v \\ w \\ \theta_x \\ \theta_y \\ \theta_z \end{Bmatrix}^T \quad . \tag{4.18}$$

Here $\hat{}$ denotes a unit vector. $\{V_d\}$ is not a unit vector as it takes the distance between the

nodes (or lever arm) into account.

The following section demonstrates how $[\tilde{C}]$ is incorporated into $[C_r]$ for a simple cantilever problem to achieve the correct coupling between the beam and shell elements.

4.4 Example: Beam-Shell Coupling

To validate $[\tilde{C}]$, a simple cantilever problem was used, in which a flat plate fixed at the one end and subjected to an end point load at node 11, as shown in Figure 4.6. The boundary conditions are given in Table 4.5.

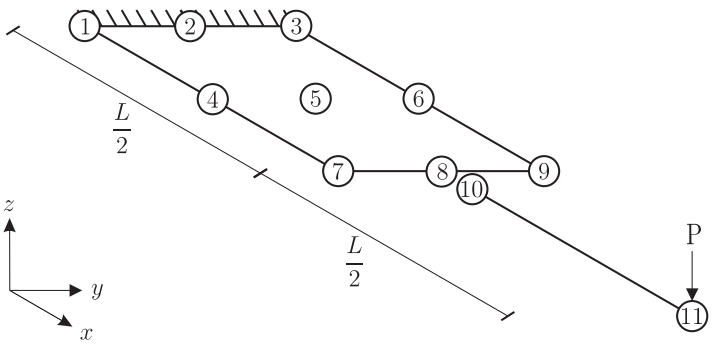

Figure 4.6: Rectangular cantilever example for beam-shell coupling.

L	1 m
b	1 m
d	0.1 m
E	1 GPa
G	0.5 GPa
ν	0
k	$\frac{5}{6}$

Table 4.3: Input parameters for the rectangular cantilever problem.

In order to impose the coupling between nodes 8 and 10, the transformation equations method was implemented, as described in Section 4.2. Recall that this approach reduces the number of equations to be solved through eliminating the DOF on one side of the coupling interface and so creating a smaller but equivalent system using the appropriate constraint relations. The main feature in this approach is the formation of the congruent transformation matrix, $[T]$,

$$[T] = \begin{bmatrix} [I] \\ -[C_c]^{-1}[C_r] \end{bmatrix},$$

which is employed to produce the reduced stiffness matrix $[K^r]$ and external force vector $\{f^r_{ext}\}$. $[\tilde{C}]$ provides the constraint relations to achieve the beam-shell coupling. At node 7, this is

$$[\tilde{C}]_7 = \begin{bmatrix} 1 & 0 & 0 & 0 & 0 & 0.5 \\ 0 & 1 & 0 & 0 & 0 & 0 \\ 0 & 0 & 1 & -0.5 & 0 & 0 \\ 0 & 0 & 0 & 1 & 0 & 0 \\ 0 & 0 & 0 & 0 & 1 & 0 \end{bmatrix}.$$

$[\tilde{C}]$ is inserted into $[C_r]$ in the columns corresponding to the beam DOF retained and in the rows corresponding to the shell DOF to be condensed out. For this problem, $[C_c]$ is a negative

identity matrix equal to the size of the number of shell nodes to be condensed out and so the format of $[T]$ is as shown in Figure 4.7.

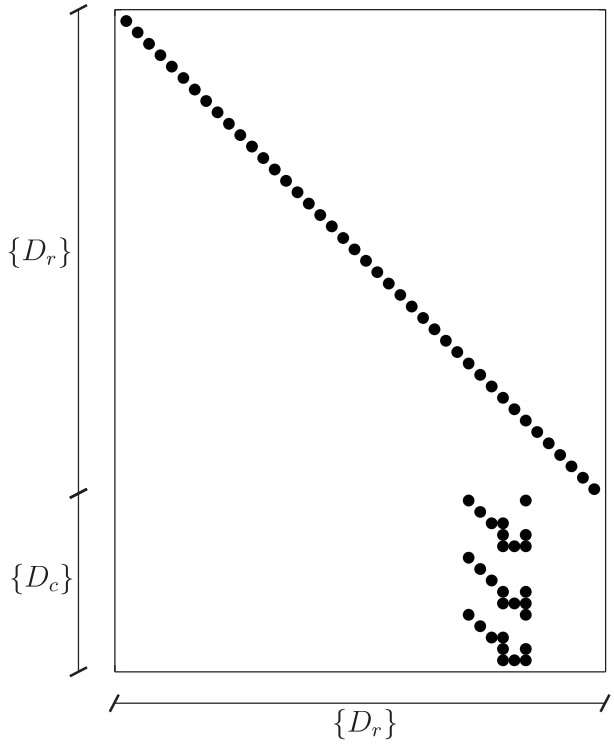

Figure 4.7: Non zero terms in the congruent transformation matrix for the rectangular cantilever in Figure 4.6.

The algorithm used to achieve the beam-shell coupling is shown in Algorithm 4.3. The inputs include the global stiffness matrix and the global external force vector, as well as a matrix, $[C_{CI}]$, which contains the node numbers at the coupling interface to be retained and condensed out respectively, such that

$$[C_{CI}] = \left[\underbrace{k_b}_{\text{retained}} \quad \underbrace{k_{s_1} \quad \ldots, \quad k_{s_n}}_{\text{condensed out}} \right] , \tag{4.19}$$

where each row corresponds to a separate coupling interface. On obtaining the reduced global stiffness matrix and reduced external force vector, the system can be solved for the free DOF in the usual manner. Afterwards, the displacements at the nodes condensed out during the coupling process can be obtained by using the inverse of $[\tilde{C}]$ in (4.18). In addition, the reactions at the fixed DOF can also be calculated.

Algorithm 4.3 Coupling EB beam and MITC9 shell elements.

INPUTS:

$[K]$	Global stiffness matrix.
$\{f_{ext}\}$	Global external force vector.
$[C_{CI}]$	Coupling interface(s) matrix.

1:	Define DOF at nodes to be condensed out.	$[d_c]$	(4.2)
2:	Define all DOF to remain.	$[d_r]$	(4.2)
3:	Redefine the boundary conditions and free DOF to account for the shell DOF that are condensed out.		
4:	**for** coupling interface $=$ 1, 2, 3, ... , n_{CI}		
5:	**for** shell node $=$ 1, 2, 3, ... , n_k		
6:	Calculate the direction vector.	$\{V_d\}$	(4.17)
7:	Calculate the constraint matrix.	$[\tilde{C}]$	(4.18)
8:	Insert $[\tilde{C}]$ into $[C_r]$.		
9:	**end**		
10:	**end**		
11:	Form $[C_c]$.		
12:	Calculate the congruent transformation matrix	$[T]$	(4.3)
13:	Calculate the congruent force vector	$[Q_0]$	(4.3)
14:	Calculate the reduced global stiffness matrix	$[K^r]$	(4.5)
15:	Calculate the reduced global internal force vector	$\{f^r_{int}\}$	(4.6)

OUTPUTS:

$[K^r]$	Reduced global stiffness matrix.
$\{f^r_{ext}\}$	Reduced global external force vector.

Through employing Algorithm 4.3, the solution obtained for the cantilever problem in Figure 4.6 agrees with EB beam theory, as shown in Table 4.5, with an appropriate, symmetric distribution of displacements through the cantilever, as shown in Figure 4.8.

In addition, an end moment and torque were also applied independently to node 11, giving a fairly close approximation to the analytical solution as shown in Table 4.5. It is interesting to note for the torsion problem that by not constraining θ_{yy} at nodes 7 and 9, and thus solving for these DOF, the exact analytical solution for θ_{xx} is obtained (though this is not shown in Table 4.5.

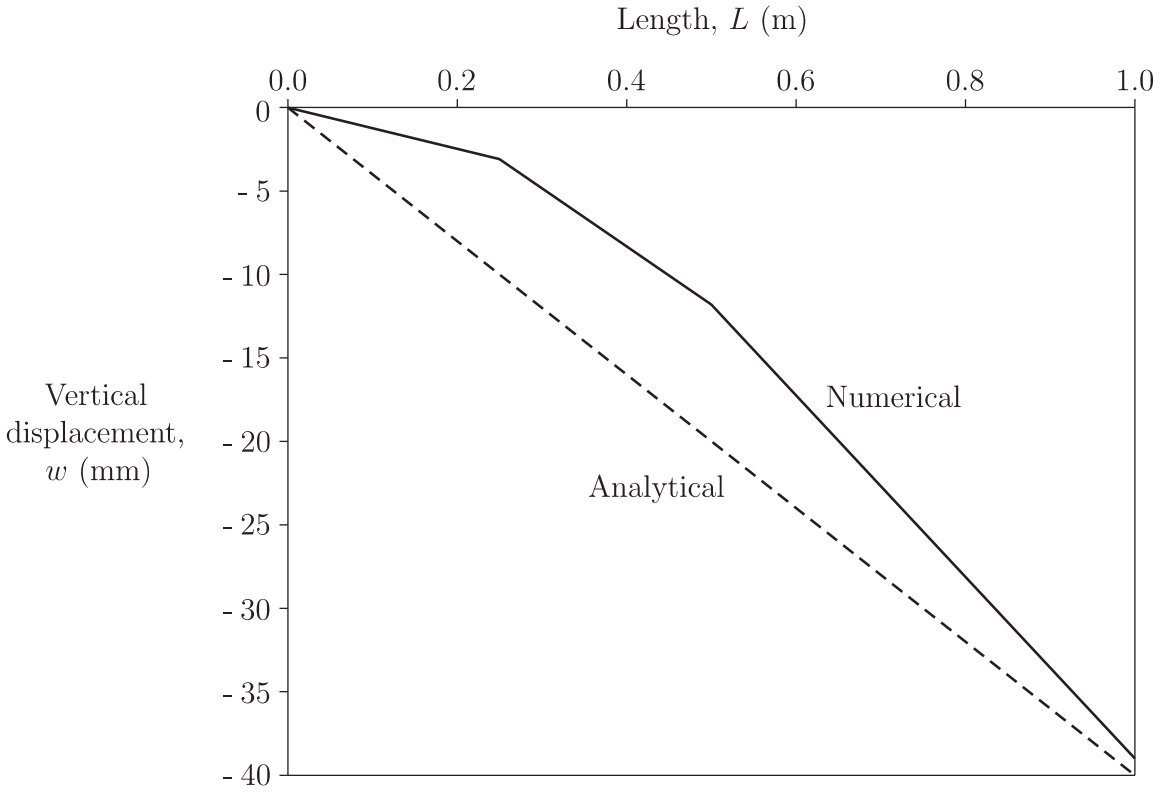

Figure 4.8: Graph of vertical displacement for the rectangular cantilever in Figure 4.6.

	End Point Load, f_{zz} **=1kN**	**End Moment,** M_{yy} **=1kNm**	**End Torque** M_{xx} **=1kNm**
BC	Fix u, v, w, θ_{xx}, θ_{yy} at nodes 1, 2, 3.	Fix u, v, w, θ_{xx}, θ_{yy} at nodes 1, 2, 3.	Fix u, w, w, θ_{xx} at nodes 1, 2, 3 and θ_{yy} at node 2.
Analytical	$w = -\frac{PL^3}{3EI_{yy}}$	$w = -\frac{ML^2}{2EI_{yy}}$	N/A.
	$w = -4.0 \times 10^{-3}$ mm	$w = -6.0 \times 10^{-3}$ mm	N/A.
	$\theta_{yy} = -\frac{PL^2}{2EI_{yy}}$	$\theta_{yy} = -\frac{ML}{EI_{yy}}$	$\theta_{xx} = \frac{TL}{JG}$
	$\theta_{yy} = -6.0 \times 10^{-3}$ rad	$\theta_{yy} = 12.0 \times 10^{-6}$ rad	$\theta_{xx} = 6.0 \times 10^{-3}$ rad
Numerical	$w = -39.3\times$ mm	$w = -60.0\times$ mm	N/A.
	$\beta_2 = 0.06$ rad	$\beta_2 = 0.12$ rad	$\beta_1 = 0.03$ rad

Table 4.5: Solutions for the rectangular cantilever with beam-shell coupling, as shown in Figure 4.6.

Furthermore, a similar problem was tested in which the cantilever is a thin-walled cylindrical member, as shown in Figure 4.9.

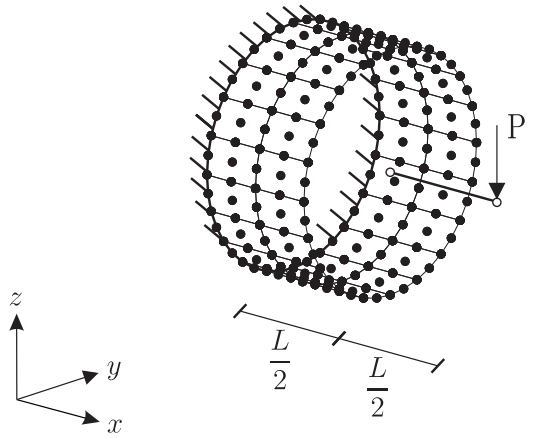

Figure 4.9: Cylindrical cantilever example meshed with 12 shell and 1 beam elements.

L	1 m
R	0.5 m
t	0.01 m
E	1 GPa
G	0.5 GPa
ν	0
k	$\frac{5}{6}$

Table 4.6: Input parameters for the cylindrical cantilever problem.

By applying an end point load, end moment and a torque to the end beam node, using the parameters in Table 4.6, there is close agreement with EB beam theory, as shown in Table 4.7. The 40% displacement error produced when applying an end point load arises from the fact that the quadratic shell and linear beam elements are used here to model a cubic displacement field.

	End Point Load, f_{zz} **=1kN**	**End Moment,** M_{yy} **=1kNm**	**End Torque** M_{xx} **=1kNm**
BC	Fix all DOF at the root.	Fix all DOF at the root.	Fix u, v, w, θ_{xx} at the root and θ_{yy} at the root where y =0 and $z = 0$.
Analytical	$w = -\frac{PL^3}{3EI_{yy}}$	$w = -\frac{ML^2}{2EI_{yy}}$	N/A.
	$w = -0.15 \times 10^{-3}$ mm	$w = -0.13 \times 10^{-3}$ mm	N/A.
	$\theta_{yy} = -\frac{PL^2}{2EI_{yy}}$	$\theta_{yy} = -\frac{ML}{EI_{yy}}$	$\theta_{xx} = \frac{TL}{JG}$
	$\theta_{yy} = 0.13 \times 10^{-3}$ rad	$\theta_{yy} = 0.26 \times 10^{-3}$ rad	$\theta_{xx} = 0.26 \times 10^{-3}$ rad
Numerical	$w = -0.09 \times 10^{-3}$ mm	$w = -0.13 \times 10^{-3}$ mm	N/A.
	$\beta_2 = 0.13 \times 10^{-3}$ rad	$\beta_2 = 0.26 \times 10^{-3}$ rad	$\beta_1 = 0.26 \times 10^{-3}$ rad

Table 4.7: Solutions for the cylindrical cantilever with beam-shell coupling, as shown in Figure 4.9.

4.5 Chapter 4 Summary

Through this chapter, methods to enforce MPC equations have been discussed, followed by the development of MPC relationships, $[\tilde{C}]$, to couple EB beam and MITC9 shell elements. This coupling matrix is simple to construct through considering the movement of vectors

between the nodes to be coupled. The coupling matrix was implemented successfully using the transformation equations method to obtain or closely approximate analytical solutions for a cantilever beam. This method involved condensing out the DOF on one side of the coupling interface, through employing the congruent transformation matrix and congruent force vector in matrix operations, thereby reducing the size of the system to solve. In the next chapter, the $[\tilde{C}]$ matrix will be employed to couple beam and shell elements to provide an efficient analysis program for the Inward Battered Guide Structure (IBGS).

Chapter 5

Numerical Analysis of the IBGS

To demonstrate the finite element techniques discussed in the preceding chapters, the linear static analysis of the Inward Battered Guide Structure (IBGS) was undertaken in MATLAB m-script [*50*]. Through varying the angle of twist in the tripod arrangement of the jacket and applying loads at the base of the turbine tower, the structural behaviour of the IBGS is assessed under normal operating conditions for a wind turbine. Firstly, an assessment of the structural behaviour is undertaken in Section 5.1 where only beam elements are used. Secondly, the coupling of beam and shell elements is employed in Section 5.2 to provide greater detail about the structural behaviour of the IBGS by examining the stress distribution through each structural joint. Throughout the chapter, the coordinate system in Figure 4.1 and the notation in Figure 5.1 are used, along with the parameters in Table 5.1. The structure was assumed to be fully fixed (in terms of both translation and rotation) at the seabed and so the sediment-pile interaction was not considered.

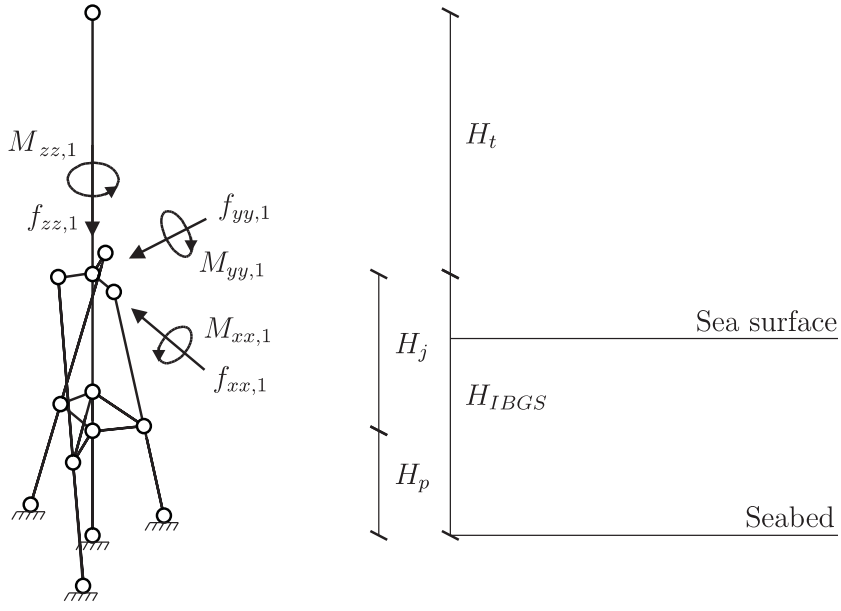

Figure 5.1: Notation and orientation of loads applied to the IBGS.

Elastic modulus	E	210 GPa
Shear modulus	G	80 GPa
Jacket height	H_j	30 m
Pile height	H_p	20 m
Foundation height	H_{IBGS}	50 m
Tower height	H_t	100 m
Radius-wall thickness ratio	t_w	$\frac{1}{20}$
Central column & pile radius		0.75 m
Jacket-leg & outer pile radius		0.65 m
Top-radial member radius		0.60 m
Top-radial member length	L_t	5 m
Inclined bracing radius		0.50 m
Angle of inclined bracing	θ_{IB}	45°
Bottom-radial member radius		0.50 m

Table 5.1: Input parameters for the numerical analysis of the IBGS.

5.1 Beam Analysis

5.1.1 Analysis Aims & Set-up

To provide an initial assessment of the general structural behaviour of the IBGS, each structural member is represented by one linear beam element with element nodes located at the structural joints, as shown in Figure 5.2. In addition, the piles and turbine tower were also

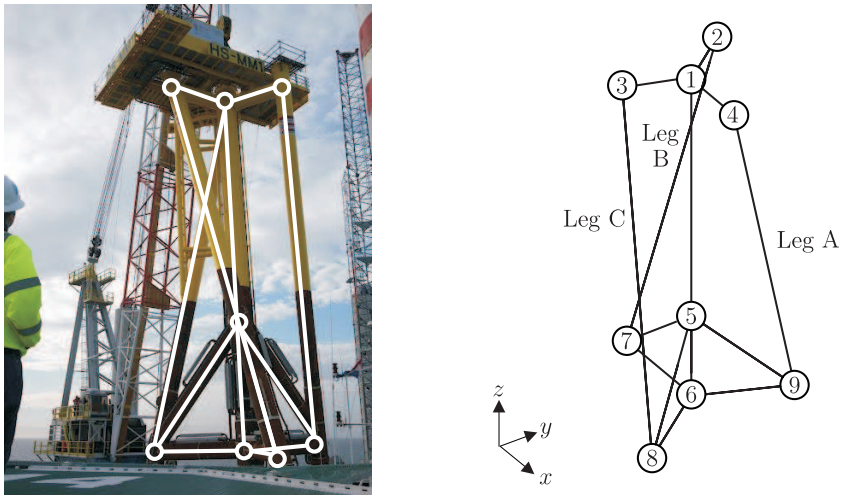

(i) (ii)

Figure 5.2: (i) Discretisation of the IBGS using linear beam elements [*16*] and (ii) the node numbering system used.

modelled, as illustrated in Figure 5.3. The aim is to use this finite element (FE) model to (i) evaluate any structural benefit of the twisted-tripod arrangement and (ii) investigate the

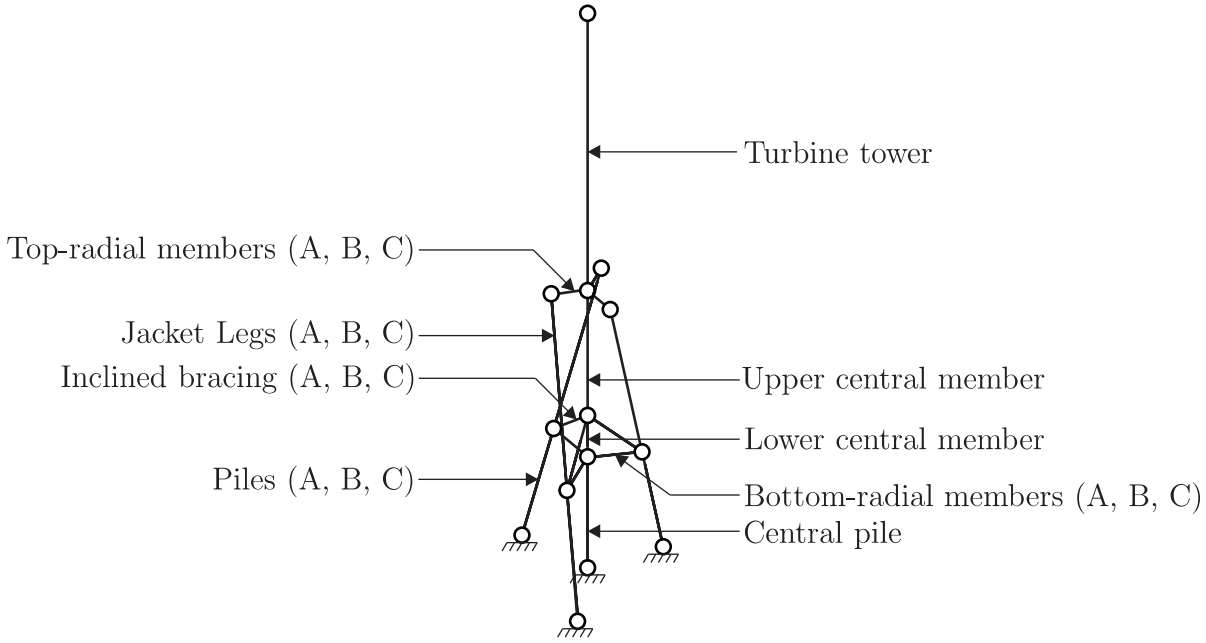

Figure 5.3: Node and member names used for the IBGS.

stiffness contribution from the inclined bracing. This was achieved by applying forces/moments to the top central node (node 1 in Figure 5.2) and comparing the stresses in each member, as well as the translations at the nacelle height, where the angle of twist in the jacket is either 0° or 60°. Algorithm B.1 in Appendix B provides an overview of how the analysis was set-up with a view to using as few input parameters as possible to define the geometry of the IBGS, in order to provide flexibility in modifying the jacket for different geometries or water depths.

5.1.2 Results & Discussion

Unit loads were applied independently at node 1 to the IBGS in each of the directions shown in Figure 5.1, where the angle of twist in the jacket is $0°$ and $60°$ respectively. By comparing the combined axial and bending stresses in the jacket-legs for each load in Table 5.2, it was found that the highest stresses were caused by forces applied in the x-y plane. It was also apparent that the twisted jacket is twice as stiff as the untwisted jacket when a yaw moment, M_{zz}, and vertical load, f_{zz}, are applied independently. These observations are not restricted to the jacket-legs, as shown in Tables C.1 and C.2 in Appendix B.

However, in order to gain a more realistic understanding of the structural behaviour of the IBGS in normal operating conditions, ultimate loads selected from an UpWind project report [*59*] were applied, as shown in Figure 5.4. This load case corresponds to the normal power production of a 5MW wind turbine in extreme wind turbulence. Figure 5.4 indicates that the pitching moment, M_{yy}, is the most important load to consider when designing a support structure for a wind turbine. On applying this pitching moment, M_{yy}, independently at node 1, it is evident in Figure 5.5 that the axial forces in the jacket-legs and piles are generally

Jacket Twist	Jacket-leg	f_{xx}	f_{yy}	f_{zz}	M_{xx}	M_{yy}	M_{zz}
$0°$	A	66	15	- 2	- 1	- 1	- 8
	B	- 32	- 55	- 2	1	1	- 8
	C	- 32	58	- 2	- 1	1	8
$60°$	A	38	- 49	- 1	2	- 1	- 4
	B	- 61	- 22	- 1	1	2	- 4
	C	29	59	- 1	- 2	- 2	- 4

Table 5.2: Combined axial and bending stresses in MPa for the jacket-legs when unit loads are applied independently at node 1.

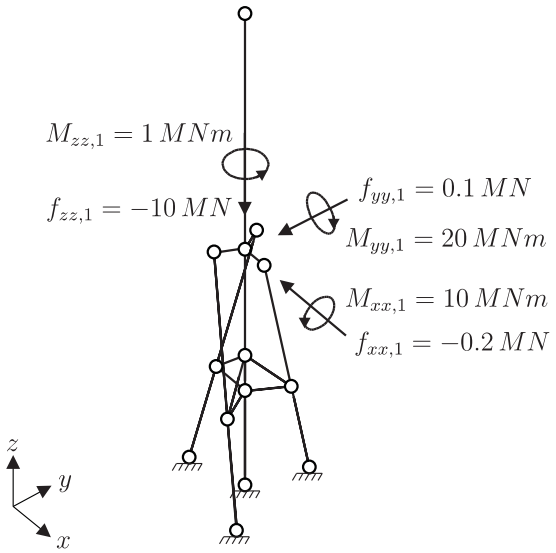

Figure 5.4: Normal operating load case for a typical 5MW wind turbine [*59*], applied to the IBGS at node 1.

higher for the untwisted jacket, though the top-radial members carry up to ten-times more axial force in the twisted jacket. Nevertheless, Figure 5.6 highlights that the maximum M_{yy} bending moments in the jacket-legs and piles of the twisted jacket are generally double those in the untwisted jacket. In the untwisted jacket, the bending moments are predominantly around the z'- axis whereas in the twisted jacket, the bending moments are about both the z' and y' axes. Together, Figures 5.5 and 5.6 demonstrate that introducing an angle of twist into the jacket structure relies on the bending characteristics of a structural member for load transfer to a greater extent than for the untwisted jacket, where load is transferred predominantly by tensile/compresssive axial forces.

Nevertheless, on applying the total load case in Figure 5.4 as a whole, it can be seen in Table 5.3 that the higher combined axial and bending stresses are in the twisted jacket. Typically, the untwisted jacket is around two-to-three times as stiff as the twisted jacket. It is also clear from Table 5.3 that the top radial members contribute the largest proportion of stress to the structure. If a typical yield strength for steel of 250MPa is assumed, then the

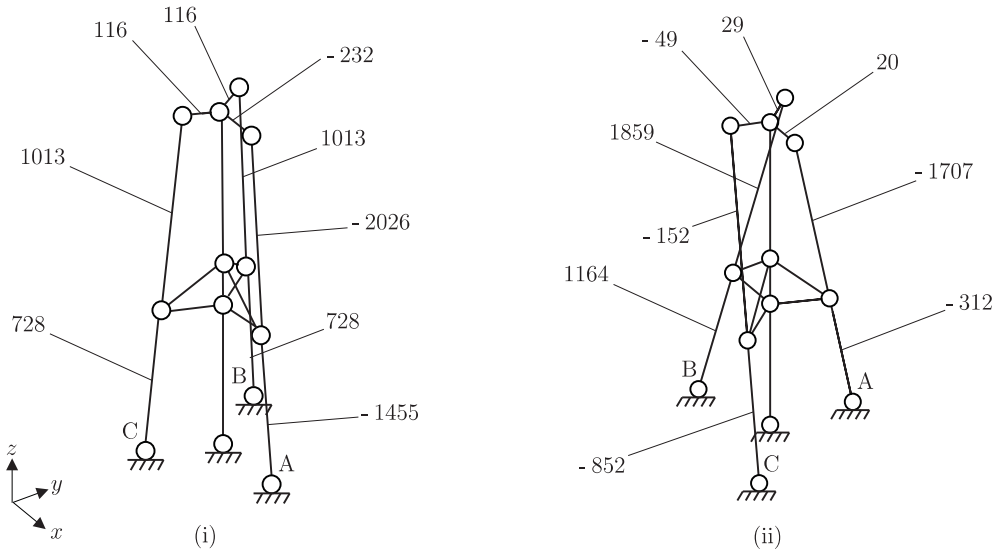

Figure 5.5: Axial forces in kN for the top-radial members, jacket-legs and piles when a pitching moment, $M_{yy} = 20MNm$, is applied to the IBGS at node 1 for (i) the untwisted jacket and (ii) the twisted jacket.

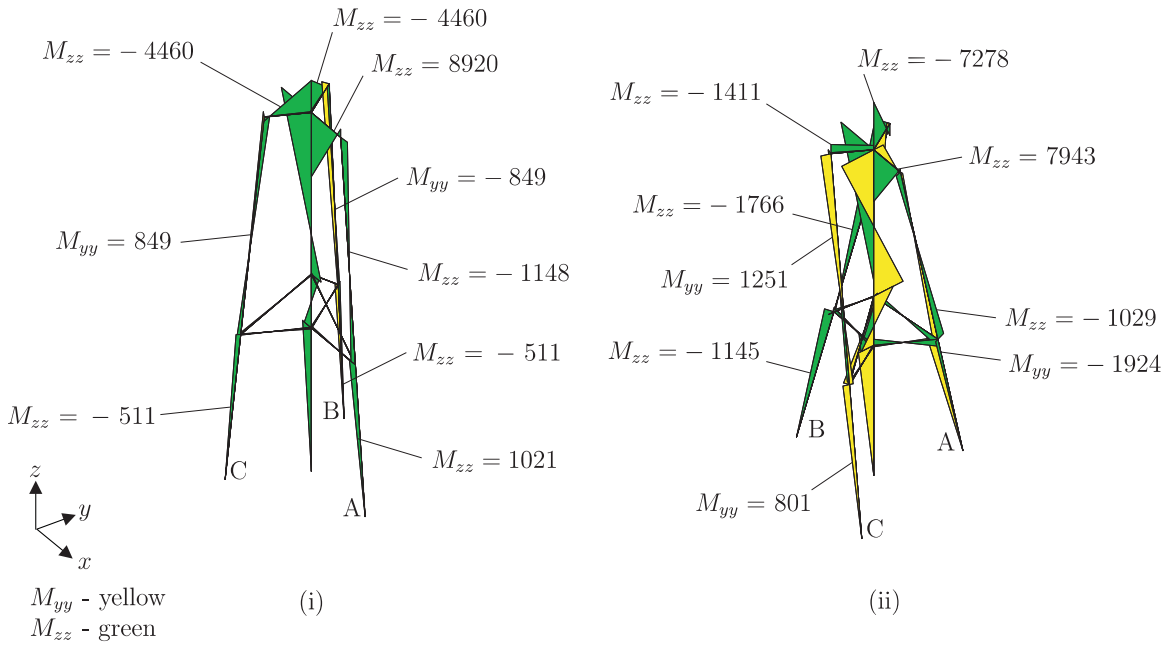

Figure 5.6: Bending moment diagrams in kNm for the top-radial members, jacket-legs and piles when a pitching moment, $M_{yy} = 20MNm$, is applied to the IBGS at node 1 for (i) the untwisted jacket and (ii) the twisted jacket.

top-radial member A would deform plastically under the jacket arrangements used. Although not modelled here, a platform would exist at the top of the jacket, which would help to transfer load away from the base of the tower to the jacket-legs - a concept that is addressed in Section 5.2. Through comparing the untwisted and twisted jacket arrangement, it is evident that the inclined bracing, bottom radial members and piles in the twisted jacket contain around one-

Member	Jacket Twist $= 0°$		Jacket Twist $= 60°$	
	Total Combined Stress	% of Total	Total Combined Stress	% of Total
Top Radial A	- 342		361	
Top Radial B	130	59	153	55
Top Radial C	- 75		- 141	
Inclined Bracing A	3		19	
Inclined Bracing B	- 59	7	- 96	13
Inclined Bracing C	- 9		- 34	
Bottom Radial A	- 12		- 43	
Bottom Radial B	68	8	90	12
Bottom Radial C	1		0	
Jacket-leg A	- 55		- 15	
Jacket-leg B	- 8	8	31	8
Jacket-leg C	- 5		- 52	
Upper Central	- 87		- 12	
Lower Central	8	12	5	1
Central Pile	- 17		5	
Pile A	- 31		- 61	
Pile B	- 2	5	- 21	12
Pile C	23		- 58	

Table 5.3: Total combined axial and bending stresses in MPa for the IBGS for the load case in Figure 5.4.

and-a-half times the amount of stress as those in the untwisted jacket. This suggests that the angle of twist in the jacket alters the load transfer path such that these members transfer load away from the central column members.

In order to try to understand the effect of the stiffness contribution from the inclined bracing in transferring the load away from the central columns, analyses using the load case in Figure 5.4 were undertaken for the following four cases: (i) without the inclined bracing, (ii) with the inclined bracing, (iii) with additional bracing option A and (iv) with additional bracing option B, as shown in Figure 5.7. On comparing the total combined stress in the jacket-legs for cases (i) and (ii), it is evident from Table 5.4 that the inclined bracing provides around three times as much stiffness in the untwisted jacket. Nevertheless, although the stresses are higher overall in the jacket legs of the twisted jacket, the inclined bracing does provide some additional stiffness and so reduces the stresses by up to one-third.

To investigate options (iii) and (iv), two bracing arrangements were considered, as shown in Figure 5.7. Option A connects the base of the jacket to the top-central node and option

Jacket-leg	Jacket Twist $= 0°$		Jacket Twist $= 60°$	
	With Bracing	Without Bracing	With Bracing	Without Bracing
A	- 55	- 12	- 15	- 29
B	- 8	- 27	31	38
C	- 5	2	- 52	- 72

Table 5.4: Total combined axial and bending stresses in MPa in the jacket-legs for the IBGS with and without the inclined bracing for the load case in Figure 5.4.

B connects the top of one jacket-leg to the base of the next jacket-leg in an anti-clockwise direction. A clear benefit is seen with option B in the top-radial members of the twisted jacket, as shown in Table 5.5, where the total combined stresses are reduced and are somewhat more symmetrically distributed around the jacket top, providing greater stability. A more complete table that summarises the total combined axial and bending stresses in each member for each of the three bracing cases can be found in Table C.3 in Appendix B.

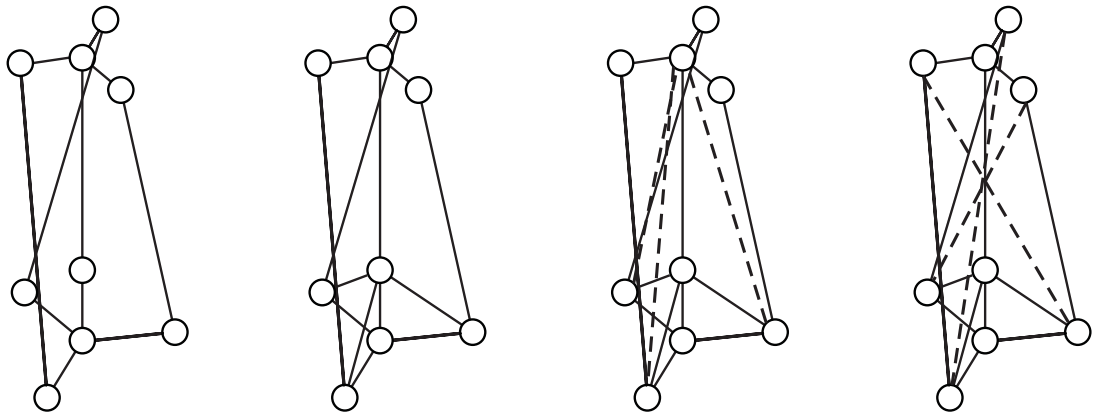

Figure 5.7: Bracing options for the IBGS: (i) no bracing, (ii) inclined bracing, (iii) additional bracing option A and (iv) additional bracing option B.

To gain a further understanding of the rigidity that the IBGS provides as a support structure for a wind turbine, the translation at the nacelle height at the top of a 100m tower was investigated by applying the load case in Figure 5.4 and varying the pile height. Here, the pile height is the distance between the bottom of the jacket and the seabed, as shown in Figure 5.1. The L2-norm of the displacements at the nacelle height are shown in Figure 5.8, which indicates that the untwisted jacket is two-to-three times as rigid as the twisted jacket for varying pile heights.

To summarise, three main observations can be made from the beam analysis. Firstly, the higher stresses are seen in the twisted jacket arrangement. Secondly, additional bracing could

Top-radial Member	Jacket Twist = 0°			Jacket Twist = 60°		
	With Original Bracing	Extra Bracing - Option A	Extra Bracing - Option B	With Original Bracing	Extra Bracing - Option A	Extra Bracing - Option B
A	- 342	- 375	- 372	361	365	- 206
B	130	166	130	153	91	54
C	- 75	- 69	- 78	- 141	- 163	299

Table 5.5: Total combined axial and bending stresses in MPa in the top-radial members for the IBGS with additional bracing for the load case in Figure 5.4.

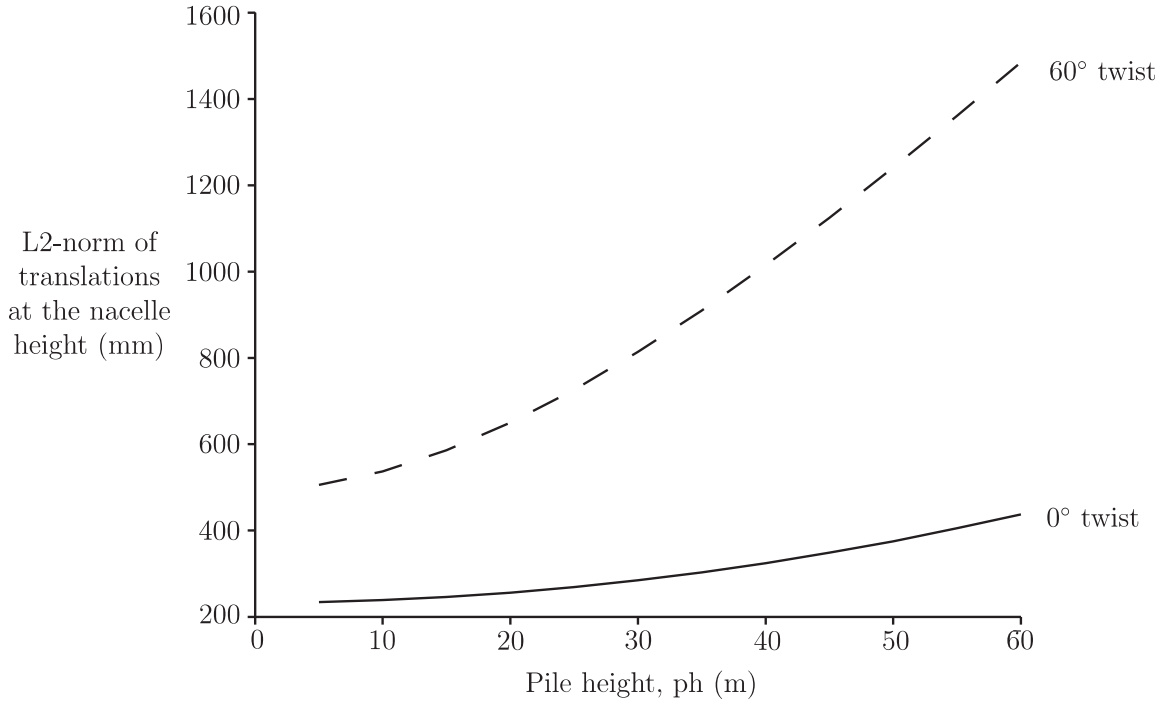

Figure 5.8: L2-norm of the displacements in mm at the nacelle height at various pile depths for the operational load case in Figure 5.4.

be used to reduce the high stresses in the top part of the jacket. Thirdly, the untwisted jacket is two-to-three times as stiff as the twisted jacket and is more favourable in restricting the tower displacement at the nacelle height. In the following section, the structural behaviour of the IBGS is assessed further by considering the stresses through each structural joint.

5.2 Coupled Analysis

5.2.1 Analysis Aims & Set-up

To obtain a greater understanding of the structural behaviour of the IBGS, the structural joints are modelled using the mixed interpolation of tensorial components shell element with nine nodes (MITC9) described in Section 3.5, coupled to the beam elements formulated in

Section 2.5 through employing the constraint equations devised in Chapter 4. This will be achieved by examining the stress distribution through each joint, as well as the displacement at the nacelle height, for the jacket twist angles 0°, 15°, 30°, 45° and 60°. The input parameters in 5.1 and the load case in Figure 5.4 were used.

Algorithm B.2 in Appendix B shows how the coupled analysis was set-up. Note that although the analysis is linear in form, a Newton-Raphson algorithm was used. This aided the debugging process when writing the code since the analysis should converge in one iteration for a linear analysis. In addition, the normalised out-of-balance force vector, defined in Chapter 1, should be zero.

The shell mesh for each structural joint was developed using Trelis^{TM} (based on CUBIT^{TM}) [*65*] and Gmsh [*37*]. These meshes formed the input file for Algorithm B.2, along with the geometry and beam element topology. The origin of each shell mesh for the structural joints was defined by the nodal coordinates used in the beam analysis. Nodes located at the interface between shell and beam elements were identified to ensure the correct transfer of nodal variables between the different element types, as described in Algorithm 3.2. Typically around 5900 nodes were eliminated from the system with a total number of degree of freedom (DOF) in the region of 650,000.

At the intersection of tubular members modelled by the shell meshes, the shell mid-surface normal was calculated as an average of the mid-surface normals on each tube at a particular node. It was found that the thickness along the average mid-surface normal should be scaled appropriately to avoid local thinning in this region, causing high stresses, such that

$$t_{intersection} = \frac{t_{tubeA}}{\{V_{n,average}\}^T.\{V_{n,tubeA}\}} \,. \tag{5.1}$$

5.2.2 Results & Discussion

Initially, it was found that the coupled FE model created very high stresses in the top-middle joint. Consequently, the alternative coupling arrangement in Figure 5.9(ii) was employed where the bottom of the turbine tower is coupled to the top of the central column as well as the three jacket-legs.

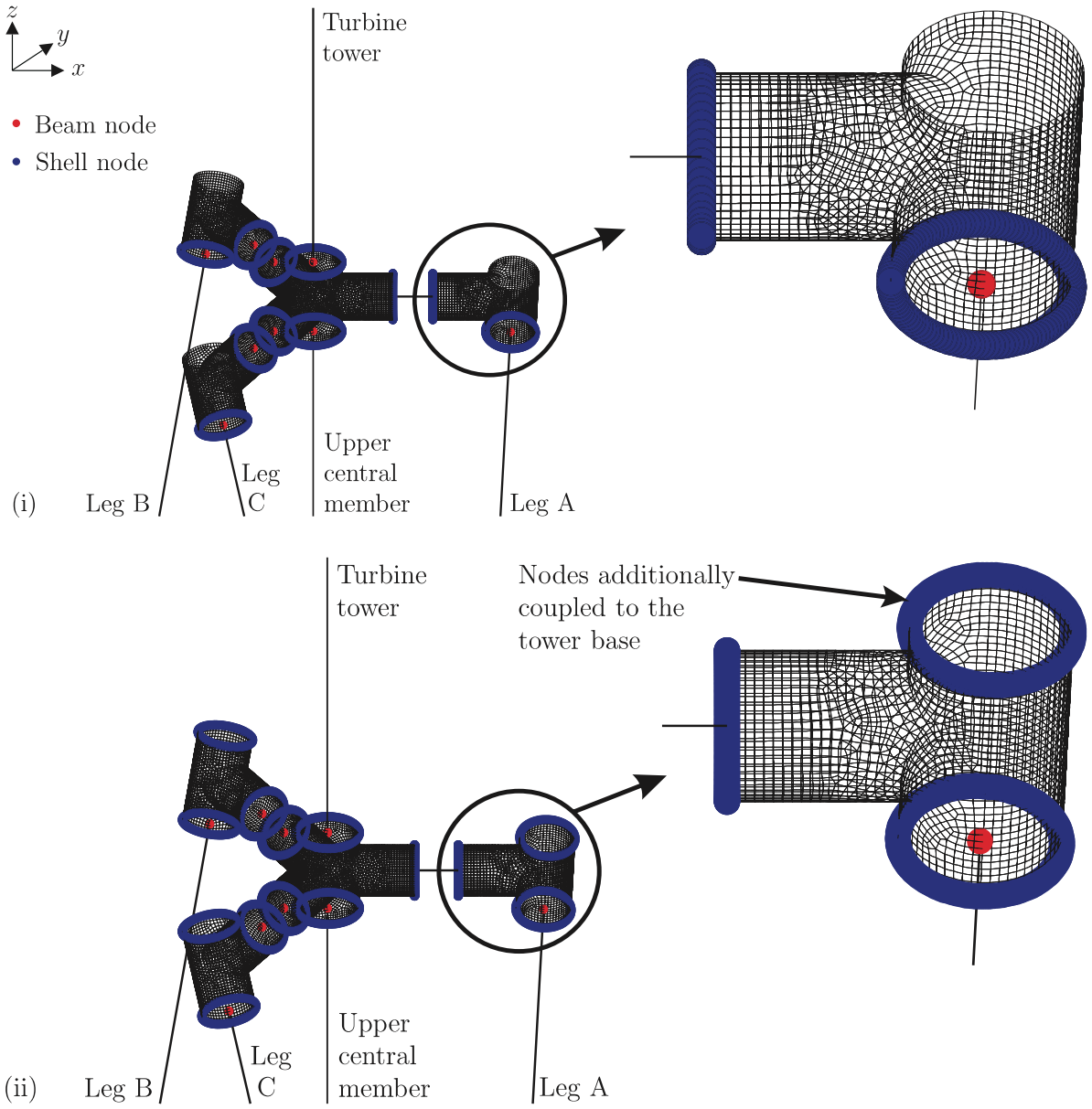

Figure 5.9: Nodes at the beam-shell coupling interface in the IBGS, where coupling between the tower base and the top of the jacket legs is employed.

In effect, this additional coupling provides extra stiffness that would be provided by the access platform at the base of the wind turbine. On running the analysis with the new coupling arrangement, it was found that the stresses were three-to-six times lower. The maximum Gauss-point (GP) stresses in each structural joint for the new coupling arrangement are shown in Table 5.6 for jacket twist angles: 0°, 15°, 30°, 45° and 60°, where the load case in Figure 5.4 is used and the tower-jacket-leg coupling is employed.

Table 5.6 shows that the maximum GP stresses generally increase as the angle of jacket-twist increases, suggesting that the jacket with 0° twist is on average 30% stiffer than the jacket with 60° twist. The highest stresses are in the top-middle joint at the base of the turbine tower

Structural Joint	Corresponding node in Beam Analysis	Angle of Jacket Twist (°)				
		0	15	30	45	60
Top-middle	1	267	273	315	391	459
Top-side A	2	102	63	74	86	93
Top-side B	3	151	126	115	116	125
Top-side C	4	132	186	229	261	295
Middle	5	266	214	229	286	362
Bottom-middle	6	148	151	184	213	235
Bottom-side A	7	236	205	230	176	262
Bottom-side B	8	177	132	195	160	234
Bottom-side C	9	153	123	168	202	216

Table 5.6: Comparison of maximum Gauss-point stresses in MPa in each structural joint for the IBGS with varying jacket-twist angles when the loads in Figure 5.4 are applied.

and the second highest stresses are in the middle joint where the inclined bracing connects to the central column. Figures 5.10, 5.11, 5.12 and 5.13 show the Von Mises stress distribution through the structural joints for jacket twists 0° and 60°, in which the orientation of the jacket-legs is the same as in Figure 5.9. The Von Mises stress (or equivalent tensile stress) was calculated at the nodes by interpolating the Cauchy stress at the Gauss points on the shell mid-surface to the nodes using the shape functions. The nodal Cauchy stress, $[\sigma]$, and deviatoric stress, $[\sigma_{dev}]$, tensors were used to calculate the Von Mises stress, σ_v, at each node as

$$\sigma_v = \sqrt{tr([\sigma_{dev}][\sigma_{dev}])} \quad \text{where} \quad [\sigma_{dev}] = [\sigma] - \frac{\sigma_{xx} + \sigma_{yy} + \sigma_{zz}}{3}[I]\,. \tag{5.2}$$

In Figure 5.12, it can be seen that the largest distribution of stresses are in the top middle-joint in the twisted jacket, around the intersection with the top-radial member A, where some of the Von Mises stresses are close to or exceed a typical yield strength for steel of 250MPa. The stresses on the outer top joints are also higher in Figure 5.12 than in Figure 5.10, which demonstrates that the twisted arrangement allows more stress to be transferred to each jacket-leg. This effect in transferring load in the twisted jacket to the jacket legs/piles is seen by comparing the stresses through the bottom joints, as shown in Figures 5.11 and 5.13 respectively.

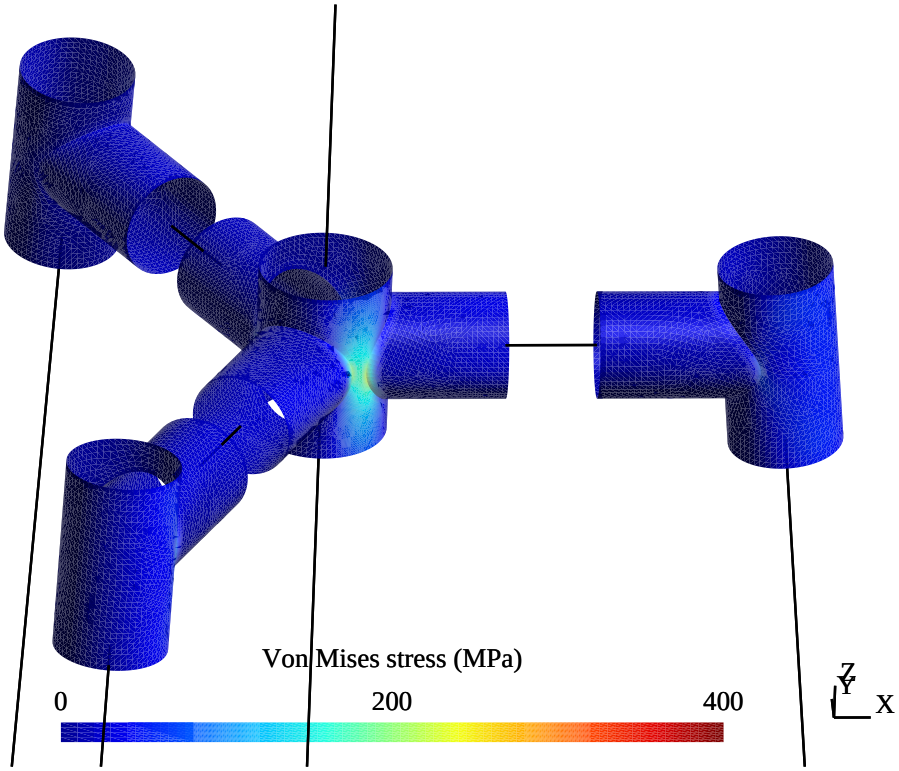

Figure 5.10: Stresses in MPa at the top of the jacket with 0° twist.

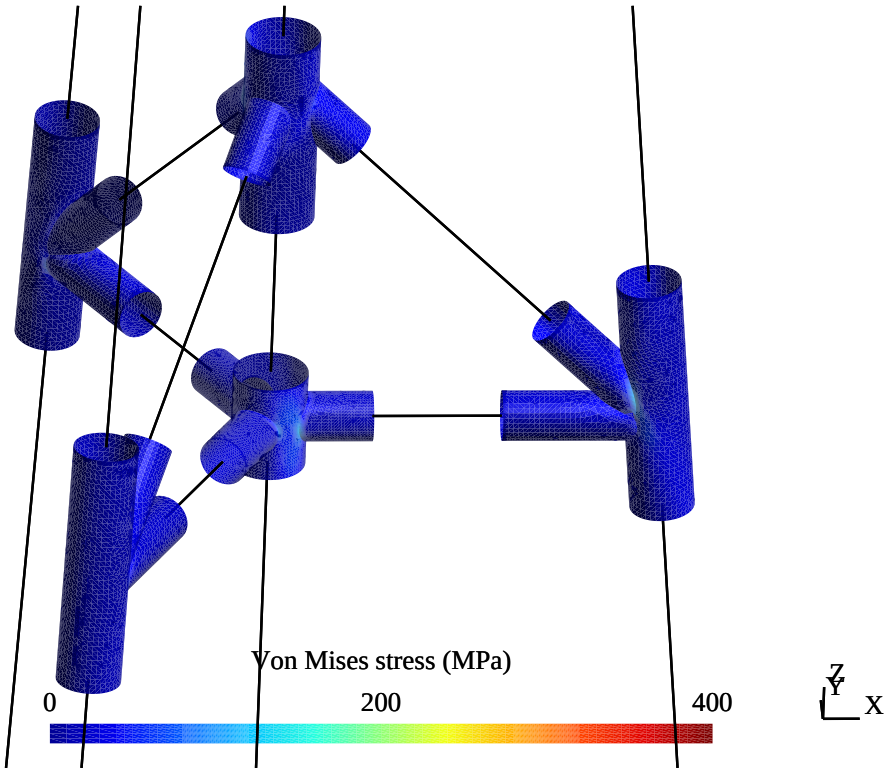

Figure 5.11: Stresses in MPa at the bottom of the jacket with 0° twist.

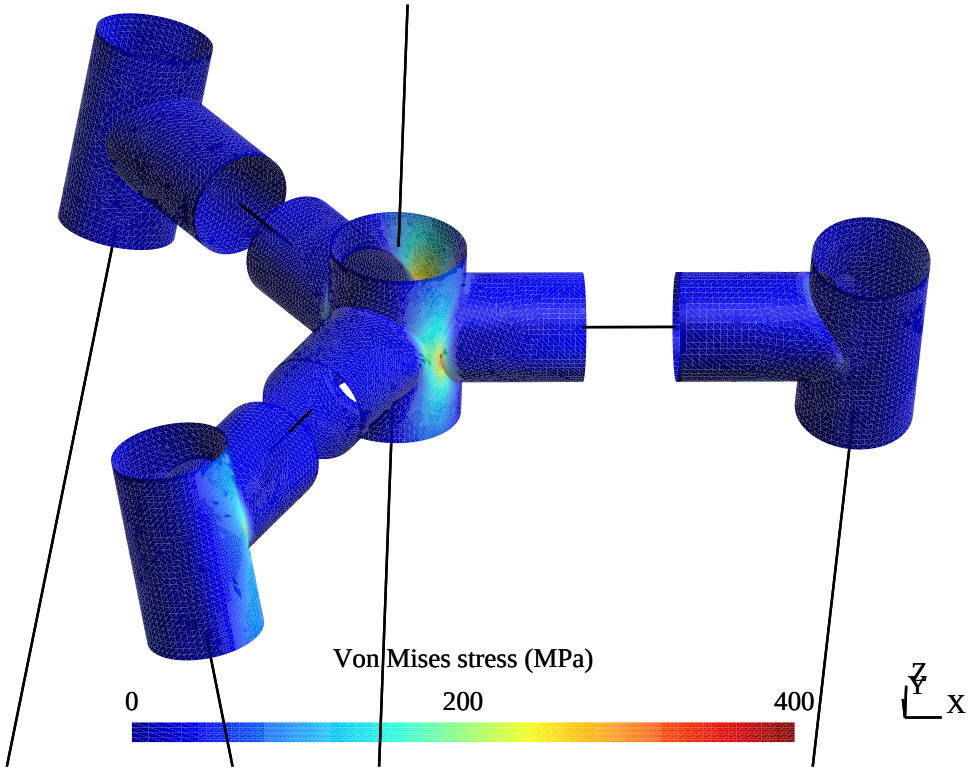

Figure 5.12: Stresses in MPa at the top of the jacket with 60° twist.

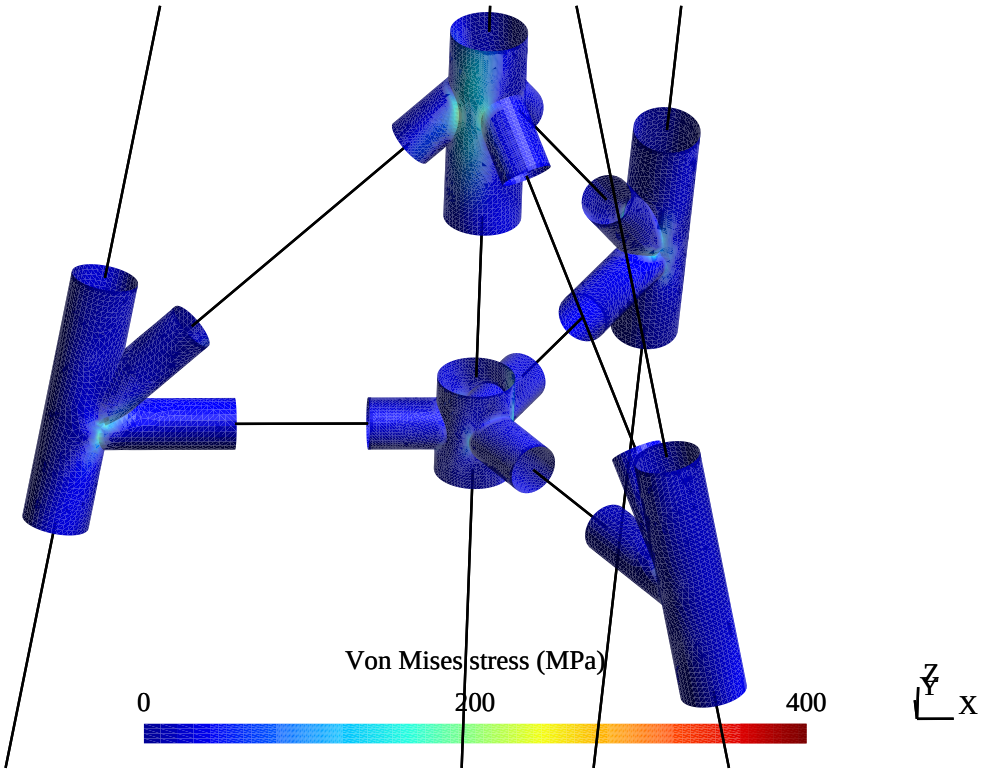

Figure 5.13: Stresses in MPa at the bottom of the jacket with 60° twist.

When employing the beam-shell coupling, it is also possible to obtain stress values along the main part of each structural member using beam elements, as shown in Table 5.7. Compared with the results from the beam analysis in Table 5.3, it can be seen that the jacket-legs and central column members, rather than the top-radial members provide the largest contribution to the stiffness of the IBGS structure. This illustrates that using only beam elements can give a distortion in the stress results which can be rectified through adopting the coupling approach. Nevertheless, the total combined axial and bending stresses in the beam elements shown in Table 5.7 again indicate that the untwisted jacket is generally around twice as stiff as the twisted jacket.

Member	**Jacket Twist** $= 0^\circ$		**Jacket Twist** $= 60^\circ$	
	Total Combined Stress	**% of Total**	**Total Combined Stress**	**% of Total**
Top-radial A	- 5		- 8	
Top-radial B	- 5	7	- 15	7
Top-radial C	- 9		- 9	
Inclined A	15		20	
Inclined B	- 15	15	- 25	16
Inclined C	- 14		- 44	
Bottom-radial A	- 10		- 12	
Bottom-radial B	8	9	17	7
Bottom-radial C	8		11	
Leg A	- 27		- 41	
Leg B	- 23	26	43	28
Leg C	- 26		- 56	
Upper central	- 41		- 71	
Lower central	- 14	29	- 21	26
Central pile	- 29		- 42	
Pile A	- 18		- 11	
Pile B	- 17	15	- 45	17
Pile C	- 9		- 32	

Table 5.7: Total combined axial and bending stresses in MPa for beam elements in the coupled analysis when the load case in Figure 5.4 is applied.

The L2-norm of the translation of the tower at the nacelle height shows that the untwisted jacket is up to five times as stiff as the twisted jacket, as shown in Figure 5.14. Here, the pile height is maintained at 20m and only the jacket-twist angle is varied. The apparent improvement in structural stiffness in the untwisted jacket, compared with the same pile depth in Figure 5.8, could be attributed to the fact that the use of shell elements at the structural

joints provides a better representation of the load transfer over these local regions.

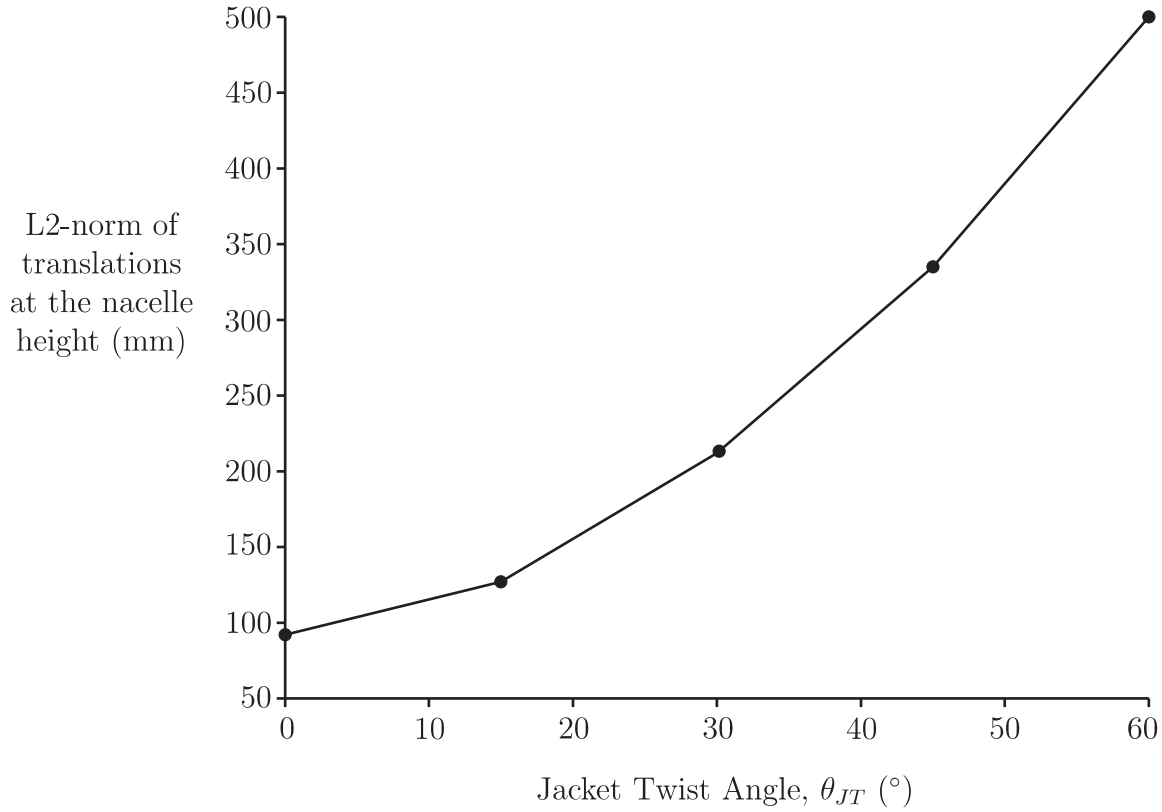

Figure 5.14: L2-norm of the displacements in mm at the nacelle height at various jacket twists for the load case in Figure 5.4.

5.3 Chapter 5 Summary

Overall, the analyses evaluated here indicate that there is no significant structural benefit in designing a jacket foundation with an angle of twist due to the reduced stiffness and higher stresses in a twisted jacket. Indeed, there would be a small cost-saving associated with using an untwisted jacket since the amount of steel required would be 1% less. In general, the analyses of the IBGS have highlighted that (i) the untwisted jacket is around two-to-three times as stiff as the twisted jacket, as demonstrated by the displacements of the wind turbine tower at the nacelle height, and that (ii) the stresses in the members and joints are higher for the twisted jacket. These results also demonstrated that the alternative load transfer path offered by the twisted jacket is not advantageous in achieving a stiff support structure. However, it must be noted that these analyses only consider a static loading case and do not allow for the dynamic loading conditions, such as how the wind pressure varies for example. The limitations of this work and suggestions for extending this research are discussed further in Chapter 6. Nevertheless, this chapter has demonstrated the successful implementation of beam-shell coupling to analyse the global and local behaviour of a tubular structure in a single analysis tool.

Chapter 6

Conclusion

The research in this thesis demonstrates the development of an efficient analysis capability that can be used to evaluate the global and local structural behaviour of the Inward Battered Guide Structure (IBGS) through firstly using beam elements and secondly using beam-shell coupling. The Beam Analysis in Section 5.1 employed linear Euler-Bernoulli (EB) beam elements as discussed in Chapter 2. These were effective in providing an overall assessment of the structural stiffness of the IBGS, using a load case corresponding to the normal operating conditions of a wind turbine. Although it was apparent that the untwisted jacket was stiffer than the twisted jacket, the results were somewhat distorted by high stresses at some nodes as linear beam elements do not account for localised regions of high stress. This limitation was overcome by employing the beam-shell coupling devised in Chapter 4, an approach that allowed the evaluation of local stress distributions at each structural joint within a global finite element analysis (FEA) of the IBGS in Section 5.2. Overall, it was found that the twisted-jacket arrangement in the IBGS showed reduced stiffness and higher stresses compared with the untwisted arrangement, as demonstrated by the larger displacements at the nacelle height and the higher stress values in the structural members and joints. There are, however, several other areas that could be incorporated into this finite element (FE) model to improve the assessment of the structural behaviour of the IBGS, as discussed in Section 6.1.1. Nonetheless, the application of the beam-shell coupling is not limited to the IBGS structure as it can be applied to any tubular structure, by providing a new input file containing the mesh (nodal coordinates, element topology and nodes for coupling), load case and boundary conditions for the structure in question.

The new method developed here to couple EB beam elements and MITC9 shell elements focuses on using vectors to correctly transfer translations and rotations between nodes with six and five DOF respectively. Equation (4.18) shows the constraint equations in the form of $[\tilde{C}]$ that allow this transfer, assuming that the coupling interface behaves as a rigid plate. These constraint equations are imposed using the transformation equations method discussed in Section 4.2.1 by eliminating the degree of freedom (DOF) on one side of the coupling

interface and so producing a reduced but equivalent system to solve. The stiffness contribution from the eliminated DOF is added to the DOF on the other side of the coupling interface using the constraint equations. For the system used in Section 5.2, the number of DOF was in the order of 650,000 with around 4,000 DOF condensed out during the coupling process. Here, the processing time to impose the constraint equations was 3 seconds and the solving time was around 15 seconds on average, (using MATLAB [*50*] on a Windows 64-bit machine). It is worth noting that if a much larger system is to be analysed than is considered here, in which computational storage within the MATLAB [*50*] environment becomes a problem, then an alternative solver, such as Cholesky decomposition with forward/backward substitution or incomplete factorisation as a preconditioner to an iterative solver, could be used instead of the backslash operator. Nevertheless, the simplicity of the constraint equations and the reduced requirement in terms of computational storage capacity that the coupling method provides gives a good basis for undertaking global and local analyses efficiently in a single FE model using different types of FE. This approach could be extended to provide coupling between other element types, as discussed in Section 6.1.2.

6.1 Further Work

6.1.1 Additional Numerical Analysis of the IBGS

The numerical analyses undertaken in Chapter 5.2 provided a good assessment of the structural behaviour of the IBGS under normal operating conditions for a wind turbine. However, there are a several areas that were not considered that could be incorporated into the coupled FE model to give a more extensive assessment of the structural behaviour of the IBGS.

Firstly, the analysis could allow for geometric non-linearity in order to allow for large deformations. In the FEA code used here, there exists the capability to undertake non-linear analysis since the script is based on the Newton-Raphson method whereby the solution is iterative to reach the convergence of $\{f\} = [K]\{d\}$, within a specified tolerance of the out-of-balance force vector, as described in Section 1.1. In a full Newton-Raphson method, the stiffness matrix, $[K]$, would be updated at each iteration. If necessary, the external loads could be applied in separate load steps in order to give a deformation path for the structure. To adapt the work used in this thesis for geometric non-linear analysis, the EB beam elements would have to be substituted for an alternative element, which is likely to be based on the Timoshenko beam theory. Nevertheless, the mixed interpolation of tensorial components shell element with nine nodes (MITC9) shell element is designed to provide the capability for non-linear analysis by updating the shell normal, $\{V_{n,k}^{t+\Delta t}\}$, at each time integration step and formulating a non-linear stiffness matrix. This matrix should be incorporated into to the MITC function in Algorithm 3.2 in order that the sum of the linear and non-linear stiffness matrices gives the overall stiffness matrix, as described in Bathe and Dvorkin [*8*]. In addition, the assumption

for the constraint equations that the coupling interface behaves as a rigid plate should be reviewed for non-linear analysis since the kinematic assumptions, where plane sections remain plane and normal to the longitudinal axis of a beam element and shell mid-surface normals remain straight and perpendicular during deformation, would be not valid.

Secondly, and perhaps more importantly, the analysis could consider transient response at start-up and shut-down as well as from wind and wave loading. Dynamic analysis is crucial for a support structure of a wind turbine and could provide an additional insight as to whether the untwisted or twisted jacket is more structurally efficient. In Chapter 5, it was evident that the twisted jacket gives a different load transfer path compared with the untwisted jacket, which could provide a clearer structural benefit under a dynamic loading regime. Nevertheless, it is essential that the natural frequency of the IBGS is not close to the 1p (rotor speed) or 3p (blade pass and tower shadow) excitation frequencies of a wind turbine [*30*, *67*]. These can be checked in solving an eigenvalue problem to find the natural vibration frequencies and associated mode shapes in the IBGS. For the dynamic analysis, in addition to the global static stiffness matrix, global mass and damping matrices would be assembled from local element mass and damping matrices. This analysis was not undertaken here since the focus of the research was developing and demonstrating the coupling of different types finite elements in a rapid analysis capability.

Thirdly, it would be interesting to compare the coupled analysis capability developed here with an equivalent analysis, using all hexahedral or all shell elements, in commercial software such as ADINA [*6*] or ANSYS [*3*]. Although each part of the work in this thesis has been verified against benchmark problems, it would be worthwhile to further demonstrate that the coupled analysis capability produces results of acceptable accuracy more efficiently than existing commercial FEA software.

Fourthly, the effects of soil-pile interaction and scouring could be incorporated into the FE model.

Finally, the welds around the structural joints in the IBGS could be modelled using solid elements since these are well suited to capturing the three-dimensional (3D) stress field to a good degree of accuracy. This would require the coupling between solid and MITC9 shell elements, as described in the next section. A twenty-noded hexahedron should be used, as opposed to the frequently used eight-noded hexahedron to avoid the problem of shear locking Cook et al. [*23*] and be consistent with the quadratic form of the MITC9 displacement field. The additional elements would provide greater detail about local stress distributions at the structural joints without a significant increase to the number of DOF, thus retaining the rapid, global and local analysis capability in a single model.

In addition to the suggestions above regarding the structural behaviour of the IBGS as discussed, further analyses could be undertaken to assess the structural integrity of the IBGS through fatigue analysis. It is important to comprehend that an assessment of the structural

stiffness does not provide the full story, especially when a structure is not easily accessible (as in offshore wind turbines). Hence, fatigue analysis could be undertaken to provide an indication of the potential failures or damage that might occur, in order that the structural design can be developed to try to mitigate these as far as possible. In this way, it is anticipated that fatigue analysis should be conducted separately from the FEA program in Algorithm B.2 since it is concerned with the longevity of the structure, rather than its response to normal or extreme loading regimes. Nevertheless, the same FE mesh could be used, provided that the structural joints and welds are modelled appropriately.

6.1.2 Extension of FE Coupling

The constraint equations developed in this thesis to provide coupling between beam and shell elements were devised through considering the movement of vectors between the nodes to be coupled. This idea could be extended to form constraint equations for the coupling of shell and solid elements where three translations and two rotations can be related to three translations. Since the three translations on a shell element would directly correspond to the three translations on a solid element, then only the conversion of the two rotations on the shell to the three translations on the solid element needs to be considered carefully. The global unit vectors, $\{\hat{V}_{1,k}\}$ and $\{\hat{V}_{2,k}\}$, defined at each shell node, could be used to relate the two rotations on the shell to the three translations on the solid element, thus the coupling matrix for solid-shell coupling in a linear static analysis might be:

$$\underbrace{\begin{Bmatrix} u \\ v \\ w \end{Bmatrix}^T}_{\text{Solid element DOF}} = \begin{bmatrix} 1 & 0 & 0 & -\hat{V}_{1,x} & \hat{V}_{2,x} \\ 0 & 1 & 0 & -\hat{V}_{1,y} & \hat{V}_{2,y} \\ 0 & 0 & 1 & -\hat{V}_{1,z} & \hat{V}_{2,z} \end{bmatrix} \underbrace{\begin{Bmatrix} u \\ v \\ w \\ \beta_1 \\ \beta_2 \end{Bmatrix}^T}_{\text{Shell element DOF}} . \tag{6.1}$$

Similarly, the coupling approach in this thesis could be developed to join beam and solid elements. As before, only the conversion of the three rotations on the beam to the three translations on the solid element needs to be considered carefully, as the translations on a beam element directly correspond to those on a solid element. To relate the beam rotations to the solid translations, the direction vector, $\{V_d\}$, similar to (4.17), could be defined between the nodes to be coupled. In this way, the matrix for beam-solid coupling in a linear static

analysis might be:

$$\underbrace{\begin{Bmatrix} u \\ v \\ w \end{Bmatrix}^T}_{\text{Solid element DOF}} = \begin{bmatrix} 1 & 0 & 0 & 0 & V_{d,z} & -V_{d,y} \\ 0 & 1 & 0 & -V_{d,z} & 0 & V_{d,x} \\ 0 & 0 & 1 & V_{d,y} & -V_{d,x} & 0 \end{bmatrix} \underbrace{\begin{Bmatrix} u \\ v \\ w \\ \theta_x \\ \theta_y \\ \theta_z \end{Bmatrix}^T}_{\text{Beam element DOF}} . \tag{6.2}$$

By incorporating these coupling matrices* into a function similar to Algorithm 4.3 within a FEA code, a more flexible rapid analysis capability would be provided whereby different parts of a structure could be modelled using the most appropriate element type in a single model. All the constraint equations could be imposed by using the transformation equations method described in Section 4.2.1 as incorporated into Algorithm 4.3, where a distinction between which nodes should undergo which type of coupling should be dictated in the input file. Please note that the matrices above are tentative and are subject to verification through benchmark problems.

As mentioned above, solid-shell coupling could be employed to model local structural details on tubular structures such as welds. Nonetheless, beam-solid coupling might be more suitable in a structure composed of non-tubular members and could be employed in the same manner as for the IBGS, in that beam elements could be used to model the main member length and solid elements could be used to model the structural joints where I or H (or similar) sections intersect. For example, an application might be found in the petrochemical industry for the design of piperacks in chemical plants and oil refineries. Here, the Structural Engineer is often required to design a piperack and pipe supports before the final pipe and anchor loads are calculated and so the Structural Engineer must make a global design allowance for the these forces. Local design checks would be performed later retrospectively to ensure that the design satisfies the finalised loadings. A parameter driven rapid FEA tool, similar to the one shown in Algorithm B.2 for the analysis of the IBGS, could be developed to aid the Structural Engineer in this task.

*Equations (6.1) and (6.2) are tentative and are subject to verification.

References

[1] Abel, J. F. and Shephard, M. S. [1979], 'An algorithm for multipoint constraints in finite element analysis', *International Journal for Numerical Methods in Engineering* **14**, 464–467.

[2] Ahmad, S., Irons, B. M. and Zienkiewicz, O. C. [1970], 'Analysis of thick and thin shell structures by curved finite elements', *International Journal for Numerical Methods in Engineering* **2**(3), 419–451.

[3] *ANSYS Structural*^{TM} [2014].
URL: *www.ansys.com*

[4] Astley, R. J. [1992], *Finite Elements in Solids and Structures - An Introduction*, Chapman & Hall.

[5] Bathe, K. [1996], *Finite Element Procedures*, Prentice Hall.

[6] Bathe, K. J. [2014], 'Automatic dynamic incremental non-linear (ADINA) finite element analysis for solids and structures'.
URL: *www.adina.com*

[7] Bathe, K. J. and Bolourchi, S. [1980], 'A geometric and material nonlinear plate and shell element', *Computers & structures* **11**(1), 23–48.

[8] Bathe, K. J. and Dvorkin, E. N. [1986], 'A formulation of general shell elements - the use of mixed interpolation of tensorial components', *International Journal for Numerical Methods in Engineering* **22**(3), 697–722.

[9] Bathe, K. J., Iosilevich, A. and Chapelle, D. [2000], 'An evaluation of the MITC shell elements', *Computers & Structures* **75**(1), 1–30.

[10] Bathe, K. J., Lee, P. S. and Hiller, J. F. [2003], 'Towards improving the MITC9 shell element', *Computers & structures* **81**(8), 477–489.

[11] Benham, P. P., Crawford, R. J. and Armstrong, C. G. [1996], *Mechanics of Engineering Materials*, second edn, Pearson.

[12] Bischoff, M., Bletzinger, K. U., Wall, W. A. and Ramm, E. [2004], *Models and Finite Elements for Thin-Walled Structures, Volume 2: Solids and Structures*, John Wiley & Sons.

[13] Bletzinger, K. U. [2000], 'Theory of Plates, Part III: Finite elements for plate in bending', *Lecture Notes, Technische Universitt Munchen* .

[14] Bucalem, M. L. and Bathe, K. J. [1993], 'Higher order MITC general shell elements', *International Journal for Numerical Methods in Engineering* **36**, 3729–3754.

[15] *Carbon Trust: Offshore Wind Accelerator Foundations Innovators* [2014].
URL: *www.carbontrust.com/our-clients/o/offshore-wind-accelerator*

[16] *Carbon Trust: Offshore Wind Accelorator* [2014].

URL: *www.carbontrust.com*

[17] *Carbon Trust press release: SMartWind successfully installs round 3's first met mast* [2011].
URL: *www.carbontrust.com*

[18] Chang, S.-C. and Lin, T.-W. [1988], 'Constraint relation implementation for finite element analysis from an element basis', *Advances in Engineering Software (1978)* **10**(4), 191–194.

[19] Chapelle, D. and Bathe, K. J. [2011], *The Finite Element Analysis of Shells - Fundamentals*, second edn, Springer.

[20] Clough, R. W. [1960], The finite element method in plane stress analysis, *in* 'Prceedings of the second conference on electronic computation.', American Society of Civil Engineers, pp. 345–377.

[21] Clough, R. W. [2004], 'Early history of the finite element method from the view point of a pioneer', *International Journal for Numerical Methods in Engineering* **60**, 283–287.

[22] Clough, R. W. and Johnson, C. P. [1968], 'A finite element approximation for the analysis of thin shells', *International Journal of Solids and Structures* **4**(1), 43 – 60.

[23] Cook, R. D., Malkus, D. S., Plesha, M. E. and Watt, R. J. [2002], *Concepts and Applications of Finite Element Analysis*, fourth edn, John Wiley & Sons.

[24] Courant, R. [1943], 'Variational methods for the solution of problems of equiblibrium and vibration.', *Bulletin of the American Mathematical Society* **49**, 1–23.

[25] Crisfield, M. A. [1991], *Non-linear Finite Element Analysis of Solids and Structures, Volume 1: Essentials*, John Wiley & Sons.

[26] Curiskis, J. I. and Valliappan, S. [1978], 'A solution algorithm for linear constraint equations in finite element analysis', *Computers & Structures* **8**(1), 117–124.

[27] de Borst, R., Crisfield, M. A., Remmers, J. J. C. and Verhoosel, C. V. [2012], *Non-linear Finite Element Analysis of Solids and Structures*, second edn, John Wiley & Sons.

[28] de Souza Neto, E A.and Peric, D. and Owen, D. R. J. [2009], *Computational Methods for Plasticity: Theory and Applications*, John Wiley & Sons.
URL: *http://books.google.co.uk/books?id=cBrQmlQW8YAC*

[29] *Department of Energy & Climate Change: UK Renewable Energy Roadmap* [2011].

[30] Dolan, D. S. L. and Lehn, P. W. [2006], 'Simulation model of wind turbine 3p torque oscillations due to wind shear and tower shadow', *Power Systems Conference and Expositions* pp. 2050–2057.

[31] Dong, S. B., Alpdogan, C. and Taciroglu, E. [2010], 'Much ado about shear correction factors in Timoshenko beam theory', *International Journal of Solids and Structures* **47**(13), 1651–1665.

[32] Dvorkin, E. N. and Bathe, K. J. [1984], 'A continuum mechanics based four-node shell element for general non-linear analysis', *Engineering Computations* **1**(1), 77–88.

[33] Dvorkin, E. N., Pantuso, D. and Repetto, E. A. [1995], 'A formulation of the MITC4 shell element for finite strain elasto-plastic analysis', *Computer Methods in Applied Mechanics and Engineering* **125**(1), 17–40.

[34] Edem, I. B. and Gosling, P. D. [2012], 'One-point quadrature ANS solid-shell element based on a displacement variational formulation Part I - Geometrically linear assessment', *Computer Methods in Applied Mechanics and Engineering* **237**, 177–191.

[35] Gallagher, R. H. [1975], *Finite Element Analysis - Fundamentals*, Prentice Hall.

[36] Gere, J. M. and Goodno, B. J. [2009], *Mechanics of Materials*, seventh edn, Cengage Learning.

[37] Geuzaine, C. and Remacle, J. F. [2009], 'Gmsh: A 3-D finite element mesh generator with built-in pre-and post-processing facilities, Software Version 2.8.2', *International Journal for Numerical Methods in Engineering* **79**(11), 1309–1331. Software Version 2.8.2.

[38] Han, S. M., Benaroya, H. and Wei, T. [1999], 'Dynamics of transversely vibrating beams using four engineering theories', *Journal of Sound and Vibration* **225**(5), 935–988.

[39] Ho, R. J., Meguid, S. A., Zhu, Z. H. and Suave, R. G. [2010], 'Consistent element coupling in nonlinear static and dynamic analyses using explicit solvers', *International Journal of Mechanics and Materials in Design* **6**, 319–330.

[40] Ho, R. J., Meguid, S. and Sauve, R. G. [2004], 'Novel coupling constraint technique for explicit finite element analysis', *International Journal of Computational Methods* **1**(02), 309–328.

[41] Hrabok, M. M. and Hrudey, T. M. [1984], 'A review and catalogue of plate bending finite elements', *Computers & Structures* **19**(3), 479–495.

[42] Huang, H. C. and Hinton, E. [1986], 'A new nine node degenerated shell element with enhanced membrane and shear interpolation', *International Journal for Numerical Methods in Engineering* **22**, 73–92.

[43] Jialin, W., Zhiwen, L., Xing, M. and Jianzheng, Z. [1996], 'A DOF expanding method for connecting solid and shell element', *Communications in numerical methods in engineering* **12**(6), 321–330.

[44] Jones, R. M. [2006], *Buckling of Bars, Plates, and Shells*, Bull Ridge Publishing.
URL: *http://books.google.co.uk/books?id=UzVBr8b_jS8C*

[45] Jr., F. W. [1980], 'Richard Courant and the finite element method: A further look', *Historia Mathematica* **7**(4), 369 – 378.

[46] Kansara, K. [2004], Development of Membrane, Plate and Flat Shell Elements in Java, PhD thesis, Virginia Polytechnic Institute & State University.

[47] Kennedy, G. J., Hansen, J. S. and Martins, J. R. R. A. [2011], 'A Timoshenko beam theory with pressure corrections for layered orthotropic beams', *International Journal of Solids and Structures* **48**(16), 2373–2382.

[48] *Keystone Engineering INC. online brochure: The 'twisted jacket' foundation* [2014].
URL: *www.keystoneengr.com*

[49] Li, Z. X., Izzuddin, B. A. and Vu-Quoc, L. [2008], 'A 9-node co-rotational quadrilateral shell element', *Computational Mechanics* **42**(6), 873–884.

[50] *MATLAB* [2011]. Version 7.12.0.635 R2011a.
URL: *www.mathworks.co.uk*

[51] McCune, R. W., Armstrong, C. G. and Robinson, D. J. [2000], 'Mixed-dimensional coupling in finite element models', *International Journal for Numerical Methods in Engineering* **49**(6), 725–750.

[52] Monaghan, D. J. [2000], Automatically coupling element of disimilar dimesion in finite element analysis, PhD Thesis, The Queen's University of Belfast.

[53] Owen, S. J. [1998], 'A survey of unstructured mesh generation technology', *International*

Meshing Roundtable pp. 239–267.

[54] Park, K. C., Felippa, C. A. and Gumaste, U. A. [2000], 'A localized version of the method of Lagrange multipliers and its applications', *Computational Mechanics* **24**(6), 476–490.

[55] Pickhaver, J. A. [2006], Numerical modelling of building response to tunnelling, DPhil, University of Oxford.

[56] Ramm, E. [1977], 'A plate/shell element for large deflections and rotations', *Formulations and computational algorithms in finite element analysis* pp. 264–293.

[57] *Renewable UK: Wind Energy in the UK - State of the Industry Report 2013* [2013].

[58] *Round 3s first met mast installation at Hornsea zone* [2012].
URL: *blog.mainstreamrp.com*

[59] Savini, B. and Lupton, R. [2011], Supervisory controller and load calculation with Individual Pitch Controller for 5MW reference turbine, Technical report, Project UpWind.

[60] Shephard, M. S. [1984], 'Linear multipoint constraints applied via transformation as part of a direct stiffness assembly process', *International Journal for Numerical Methods in Engineering* **20**, 2107–2112.

[61] Shim, K. W., Monaghan, D. J. and Armstrong, C. G. [2002], 'Mixed dimensional coupling in finite element stress analysis', *Engineering with Computers* **18**, 241–252.

[62] Stander, N., Matzenmiller, A. and Ramm, E. [1989], 'An assessment of assumed strain methods in finite rotation shell analysis', *Engineering Computations* **6**(1), 58–66.

[63] *Strong foundations* [2014].
URL: *www.energyengineering.co.uk*

[64] *The Crown Estates: Offshore Wind Cost Reduction Pathways Study* [2012].

[65] *Trelis FEA - Finite element analysis pre-processor* [2014]. Developed by csimsoft for Sandia National Laboratories, Software Version 14.0.
URL: *www.csimsoft.com/trelis-fea.jsp*

[66] Turner, M. J., Clough, R. W., Martin, H. C. and J, T. L. [1956], 'Stiffness and deflection of complex structures', *Journal of Aeronautical Sciences* **23**, 805–823.

[67] van der Tempel, J. and Molenaar, D.-P. [2002], 'Wind turbine structural dynamics-a review of the principles for modern power generation, onshore and offshore', *Wind Engineering* **26**(4), 211–222.

[68] Yang, H. T. Y., Saigal, S., Masud, A. and Kapania, R. K. [2000], 'A survey of recent shell finite elements', *International Journal for Numerical Methods in Engineering* **47**(1-3), 101–127.

[69] Zienkiewicz, O. C. and Taylor, R. L. [2000], *The Finite Element Method - Volume 2: Solid Mechanics*, fifth edn, Butterworth-Heinemann.

Appendix A

3D Euler-Bernoulli Beam Element Stiffness Matrix

The local 3D Euler-Bernoulli beam element stiffness matrix, $[K_b^e]$, as derived in Chapter 2 is shown on the next page.

$$
\begin{Bmatrix}
f_{xx,1} \\ f_{yy,1} \\ f_{zz,1} \\ M_{xx,1} \\ M_{yy,1} \\ M_{zz,1} \\ f_{xx,2} \\ f_{yy,2} \\ f_{zz,2} \\ M_{xx,2} \\ M_{yy,2} \\ M_{zz,2}
\end{Bmatrix}
=
\begin{bmatrix}
\frac{EA}{L} & 0 & 0 & 0 & 0 & 0 & -\frac{EA}{L} & 0 & 0 & 0 & 0 & 0 \\
0 & \frac{12EI_{zz}}{L^3} & 0 & 0 & 0 & \frac{6EI_{zz}}{L^2} & 0 & -\frac{12EI_{zz}}{L^3} & 0 & 0 & 0 & \frac{6EI_{zz}}{L^2} \\
0 & 0 & \frac{12EI_{yy}}{L^3} & 0 & -\frac{6EI_{yy}}{L^2} & 0 & 0 & 0 & -\frac{12EI_{yy}}{L^3} & 0 & -\frac{6EI_{yy}}{L^2} & 0 \\
0 & 0 & 0 & \frac{GJ}{L} & 0 & 0 & 0 & 0 & 0 & -\frac{GJ}{L} & 0 & 0 \\
0 & 0 & -\frac{6EI_{yy}}{L^2} & 0 & \frac{4EI_{yy}}{L} & 0 & 0 & 0 & \frac{6EI_{yy}}{L^2} & 0 & \frac{2EI_{yy}}{L} & 0 \\
0 & \frac{6EI_{zz}}{L^2} & 0 & 0 & 0 & \frac{4EI_{zz}}{L} & 0 & -\frac{6EI_{zz}}{L^2} & 0 & 0 & 0 & \frac{2EI_{zz}}{L} \\
-\frac{EA}{L} & 0 & 0 & 0 & 0 & 0 & \frac{EA}{L} & 0 & 0 & 0 & 0 & 0 \\
0 & -\frac{12EI_{zz}}{L^3} & 0 & 0 & 0 & -\frac{6EI_{zz}}{L^2} & 0 & \frac{12EI_{zz}}{L^3} & 0 & 0 & 0 & -\frac{6EI_{zz}}{L^2} \\
0 & 0 & -\frac{12EI_{yy}}{L^3} & 0 & \frac{6EI_{yy}}{L^2} & 0 & 0 & 0 & \frac{12EI_{yy}}{L^3} & 0 & \frac{6EI_{yy}}{L^2} & 0 \\
0 & 0 & 0 & -\frac{GJ}{L} & 0 & 0 & 0 & 0 & 0 & \frac{GJ}{L} & 0 & 0 \\
0 & 0 & -\frac{6EI_{yy}}{L^2} & 0 & \frac{2EI_{yy}}{L} & 0 & 0 & 0 & \frac{6EI_{yy}}{L^2} & 0 & \frac{4EI_{yy}}{L} & 0 \\
0 & \frac{6EI_{zz}}{L^2} & 0 & 0 & 0 & \frac{2EI_{zz}}{L} & 0 & -\frac{6EI_{zz}}{L^2} & 0 & 0 & 0 & \frac{4EI_{zz}}{L}
\end{bmatrix}
\begin{Bmatrix}
u_1 \\ v_1 \\ w_1 \\ \theta_{xx,1} \\ \theta_{yy,1} \\ \theta_{zz,1} \\ u_2 \\ v_2 \\ w_2 \\ \theta_{xx,2} \\ \theta_{yy,2} \\ \theta_{zz,2}
\end{Bmatrix}
$$

Appendix B

Numerical Analysis Algorithms

The algorithms on the following pages show the set-up and procedure for the numerical analyses undertaken in Chapter 5.

Algorithm B.1 Beam linear analysis

INPUTS:

θ_{JT}	Jacket twist angle
H_j	Jacket height
H_p	Pile height
L_t	Top-radial member length
θ_{IB}	Angle of inclined bracing
H_t	Tower height
t_w	Radius-wall thickness ratio
R_{ext}	External radii for all members
E	Young's Modulus
G	Shear Modulus
	Boundary conditios
$\{f_{ext}\}$	External loads

SETUP:

1:	Define bottom-radial member length.	L_b	$L_b = 1.5 \times L_t$
2:	Define height of lower central column.	H_{lc}	$H_{lc} = L_b \tan\theta_{ib}$
3:	Calculate the nodal coordinates.	x, y, z	
4:	Define the element topology and store the external radius for each member in the same matrix.		
5:	Assign boundary conditions and external loads to the appropriate degree of freedom (DOF).		

ANALYSIS:

1:	Calculate member properties (A, I_{yy}, I_{yy}, J) and store in the element topology matrix.		
2:	Formulate the global beam element stiffness matrix.	$[K_b^e]$	Algorithm 2.1
3:	Assemble global structure stiffness matrix.	$[K]$	
3:	Formulate the global force vector.	$\{f_{ext}\}$	
4:	Solve for the displacements.	$\{d\}$	(1.7)
5:	Calculate the maximum combined axial and bending stress.	$\{\sigma_b\}$	

OUTPUTS:

$\{d\}$	Nodal displacements.
$\{\sigma_b\}$	Maximum combined axial and bending stress.

Algorithm B.2 Coupled linear analysis, using the Newton-Raphson method.

INPUTS:

θ_{JT}	Jacket twist angle
H_j	Jacket height
H_p	Pile height
L_t	Top-radial member length
θ_{ib}	Angle of inclined bracing
H_t	Tower height
t_w	Radius-wall thickness ratio
R_{ext}	External radii for all structural members
E	Young's Modulus
G	Shear Modulus
	Boundary conditios
$\{f_{ext}\}$	External loads
x_s, y_s, z_s	Shell nodal coordinates
	Shell element topology

SETUP:

1:	Define bottom-radial member length.	L_b	$L_b = 1.5 \times L_t$
2:	Define height of lower central column.	H_{lc}	$H_{lc} = L_b \tan\theta_{ib}$
3:	Calculate the beam nodal coordinates.	x, y, z	
4:	Combine beam and shell nodal coordinates into one matrix.		
5:	Define the beam element topology, calculate member properties (A, I_{yy}, I_{yy}, J) and store in the beam element topology matrix.		
6:	Rotate each shell mesh to allign with the correct structural joint loacation using the beam nodal coordinates as the origin for each joint.		
7:	Calculate the angles that define the shell mid-surface normal at each node. *Note: Calculating angles ϕ and ψ provides an efficient way to store data for $\{V_{n,k}\}$. To determine ϕ and ψ, $\{V_n\}$ can be calculated by using the normalised vector between the nodal coordinate and the corresponding point on the central axis of the structural member. At the intersection of structural members, the average normal is calculated and the thickness at these nodes should be scaled to avoid local thinning, using* (5.1)*.*	ϕ_k, ψ_k	$\phi = \tan^{-1}\left(\frac{\sqrt{V_{n,y}^2+V_{n,z}^2}}{V_{n,x}}\right)$ $\psi = \tan^{-1}\left(\frac{V_{n,z}}{V_{n,y}}\right)$
8:	Combine beam and shell element topologies into one matrix.		
9:	Identify nodes at the coupling interfaces.	$[C_{CI}]$	
10:	Assign boundary conditions and external loads.		

Algorithm B.2 continued.

ANALYSIS:			
1:	**for** load step = 0, 1		
2:	**while** the normalised out-of-balance force vector is greater than the specified tolerance and the number of iterations for solving this load step is less than the maximum.		$\frac{\lvert\{f_{oobf}\}\rvert}{\lvert\{f_{ext}\}\rvert} \leq$ tol. and $n_i \leq n_{i,max.}$
3:	**if** load step = 1		
4:	Apply beam-shell coupling.		Algorithm 4.3
5:	Adjust the boundary conditions (BC) if the relevant DOF have been condensed out during coupling.		
6:	Solve for the incremental displacements (for the retained DOF).	$\{\delta d_r\}$	(1.7)
7:	Recover the displacements at DOF condensed out during the coupling process by mapping between the beam and shell DOF at each coupling interface, using the inverse of $[\tilde{C}]$.	$\{\delta d_c\}$	(4.18)
8:	Calculate the incremental reactions.	$\{\delta f_{ext}\}$	
9:	**end**		
10:	**for** shell element = 1, 2, 3, ..., n_s		
11:	Formulate the MITC9 stiffness matrix and internal element force vector.	$[K_s^e]$, $\{f_{ext,\,s}^e\}$	Algorithm 3.2
12:	Assemble these into the (sparse) global stiffness matrix and global internal force vector.	$[K]$, $\{f_{int}\}$	
13:	Store the Cauchy stress calcuated at each Gauss point in Algorithm 3.2.	σ_{GP}	
14:	**end**		
15:	**for** beam element = 1, 2, 3, ..., n_b		
16:	Formulate the three-dimensional (3D) Euler-Bernoulli (EB) beam element stiffness matrix and calculate the internal element force vector.	$[K_b^e]$, $\{f_{ext,\,b}^e\}$	Algorithm 2.1 $\{f_{int,\,b}^e\} = [K_b^e]\{d^e\}$
17:	Assemble these into the global (sparse) stiffness matrix and global internal force vector.	$[K]$, $\{f_{ext}\}$	
18:	Calculate the maximum combined axial and bending stress.	σ_b	
19:	**end**		
20:	Calculate the out-of-balance force vector at iteration i.	$\{f_{oobf,\,i}\}$	(1.8)
21:	**end**		
22:	**end**		

Algorithm B.2 continued.

OUTPUTS:

$\{d\}$	Nodal displacements.
$\{\sigma_{GP}\}$	Gauss point Cauchy stresses in shell elements.
$\{\sigma_b\}$	Maximum combined axial and bending stress in beam elements.

Appendix C

Beam Analysis Results - Additional Data

Member	External Radius (m)	f_{xx}	f_{yy}	f_{zz}	M_{xx}	M_{yy}	M_{zz}
Top-radial A	0.6	156	- 6	- 10	0	- 14	7
Top-radial B	0.6	- 78	- 135	- 10	12	7	- 7
Top-radial C	0.6	- 78	135	- 10	- 12	7	7
Inclined A	0.5	87	63	- 1	- 1	0	- 13
Inclined B	0.5	- 54	- 72	- 1	0	- 1	- 13
Inclined C	0.5	- 54	76	- 1	0	- 1	13
Bottom-radial A	0.5	- 127	- 46	1	0	- 1	16
Bottom-radial B	0.5	64	111	1	1	0	16
Bottom-radial C	0.5	64	- 110	1	- 1	0	- 16
Leg A	0.65	66	15	- 2	- 1	- 1	- 8
Leg B	0.65	- 32	- 55	- 2	1	1	- 8
Leg C	0.65	- 32	58	- 2	- 1	1	8
Upper central	0.75	- 105	- 105	1	- 4	- 4	0
Lower central	0.75	66	66	0	1	- 1	0
Central pile	0.75	93	93	0	1	- 1	0
Pile A	0.65	61	30	0	- 1	- 1	- 18
Pile B	0.65	- 27	- 46	0	1	1	- 18
Pile C	0.65	- 27	52	0	- 1	1	18

Table C.1: Combined axial and bending stresses in MPa for the untwisted jacket when unit loads are applied independently at node 1.

Member	**External Radius**	f_{xx}	f_{yy}	f_{zz}	M_{xx}	M_{yy}	M_{zz}
Top-radial A	0.6	116	- 112	5	6	13	- 15
Top-radial B	0.6	- 155	- 44	5	- 8	12	- 15
Top-radial C	0.6	- 39	156	5	- 14	- 2	- 15
Inclined A	0.5	- 58	- 63	- 2	2	2	- 4
Inclined B	0.5	- 55	36	- 2	- 2	- 2	- 4
Inclined C	0.5	58	66	- 2	2	- 2	- 4
Bottom-radial A	0.5	- 36	87	2	- 1	- 3	6
Bottom-radial B	0.5	61	- 67	2	2	2	6
Bottom-radial C	0.5	- 88	- 18	2	- 3	1	6
Leg A	0.65	38	- 49	- 1	2	- 1	- 4
Leg B	0.65	- 61	- 22	- 1	1	2	- 4
Leg C	0.65	29	59	- 1	- 2	- 2	- 4
Upper central	0.75	96	96	1	5	- 5	0
Lower central	0.75	64	64	1	2	- 2	1
Central pile	0.75	63	63	1	2	- 2	1
Pile A	0.65	34	- 43	- 3	1	- 2	- 4
Pile B	0.65	- 27	39	- 3	- 2	1	- 4
Pile C	0.65	51	28	- 3	- 2	- 1	- 4

Table C.2: Combined axial and bending stresses in MPa for the twisted jacket when unit loads are applied independently at node 1.

Member	Jacket Twist $= 0°$			Jacket Twist $= 60°$		
	With Original Bracing	Extra Bracing - Option A	Extra Bracing - Option B	With Original Bracing	Extra Bracing - Option A	Extra Bracing - Option B
Top-radial A	- 342	- 375	- 372	361	365	- 206
Top-radial B	130	166	130	153	91	54
Top-radial C	- 75	- 69	- 78	- 141	- 163	299
Inclined A	3	- 7	- 7	19	- 24	- 30
Inclined B	- 59	- 47	- 43	- 96	- 57	- 62
Inclined C	- 9	- 7	- 25	- 34	- 27	20
Bottom-radial A	- 12	- 18	- 27	- 43	- 3	- 17
Bottom-radial B	68	58	34	90	71	51
Bottom-radial C	1	- 1	6	0	- 5	- 68
Leg A	- 55	- 35	- 39	- 15	- 23	- 23
Leg B	- 8	- 2	- 2	31	19	17
Leg C	- 5	- 3	- 19	- 52	- 33	- 33
Upper central	- 87	- 29	- 122	- 12	- 29	- 127
Lower central	8	28	21	5	5	20
Extra bracing A	n/a	4	- 9	n/a	- 54	9
Extra bracing B	n/a	58	17	n/a	- 23	- 6
Extra bracing C	n/a	24	1	n/a	10	- 44
Central pile	- 17	8	- 55	5	3	26
Pile A	- 31	- 28	21	- 61	- 54	- 49
Pile B	- 2	- 4	31	- 21	- 16	- 18
Pile C	23	22	22	- 58	- 57	- 63

Table C.3: Total combined axial and bending stresses in MPa in the IBGS with additional bracing for the load case in Figure 5.4.